



UNIVERSITY
OF
JOHANNESBURG

COPYRIGHT AND CITATION CONSIDERATIONS FOR THIS THESIS/ DISSERTATION



- Attribution — You must give appropriate credit, provide a link to the license, and indicate if changes were made. You may do so in any reasonable manner, but not in any way that suggests the licensor endorses you or your use.
- NonCommercial — You may not use the material for commercial purposes.
- ShareAlike — If you remix, transform, or build upon the material, you must distribute your contributions under the same license as the original.

How to cite this thesis

Surname, Initial(s). (2012) Title of the thesis or dissertation. PhD. (Chemistry)/ M.Sc. (Physics)/ M.A. (Philosophy)/M.Com. (Finance) etc. [Unpublished]: [University of Johannesburg](https://ujdigispace.uj.ac.za). Retrieved from: <https://ujdigispace.uj.ac.za> (Accessed: Date).

TEIO
BULK

ELECTRON CYCLOTRON RESONANCE PLASMA ENHANCED CHEMICAL VAPOUR
DEPOSITION OF SiO_xN_y : OPTICAL PROPERTIES AND APPLICATIONS

by

PAVEL VICTOROVICH BULKIN

ПАВЕЛ ВИКТОРОВИЧ БУЛКИН

Thesis submitted in partial fulfilment of the requirements for the degree

DOCTOR INGENERIAE

in

ELECTRICAL AND ELECTRONIC ENGINEERING

in the

FACULTY OF ENGINEERING

at the

RAND AFRIKAANS UNIVERSITY

JOHANNESBURG

REPUBLIC OF SOUTH AFRICA

SUPERVISOR: PROF. P.L.SWART

CO-SUPERVISOR: PROF. B.M.LACQUET

DECEMBER 1994

ABSTRACT

A technology was developed for the manufacturing of optical interference coatings with truly inhomogeneous refractive index profiles. The computer-controlled electron cyclotron resonance plasma enhanced chemical vapour deposition of thin films of SiO_xN_y from a mixture of gases (SiH_4 , O_2 , N_2 and Ar) has proven to be an effective technique for the manufacturing of such complex structures as single- and double-band rugate optical interference filters and graded refractive index antireflection coatings.

The deposition of thin films of SiO_xN_y of different composition was studied and the influence of different process conditions on the optical properties of the material was investigated. The properties of the films were studied by means of optical transmission spectroscopy, Raman spectroscopy and Fourier transform infrared spectroscopy. A whole range of optical constants was extracted for use in the computer-aided design of optical coatings.

The design of different types of inhomogeneous optical coatings was performed on the basis of optical constants available in the SiO_xN_y -system, with the dispersion of complex refractive index and absorption in the layers taken into account. It was found that such dispersion and absorption effectively suppress high-frequency filter bands.

The technology thus developed provides for the growth of conventional multilayer structures with sharp interfaces and any custom designed refractive index profile. Experimental verification of the technology was done by the manufacturing and characterization of different types of optical coatings. Several rugate interference filters, two antireflection coatings, a quarterwave multilayer interference filter and a beamsplitter were grown on silicon and Corning 7059 glass substrates. In comparison with existing deposition techniques, electron cyclotron resonance plasma enhanced chemical vapour deposition has proved to be extremely flexible and constrained only by the availability of the appropriate gas precursors for the synthesis of materials.

ACKNOWLEDGEMENTS

I would like to thank my supervisor, Professor P.L. Swart, and my co-supervisor, Professor B.M. Lacquet for their continuous support, advice and help throughout all work.

I would like to express my great respect to the blessed memory of Dr. Alexander Chumakov of the Epitaxy Laboratory of Institute of Microelectronics Technology Russian Academy of Sciences, who was my mentor and best friend during my work in his research group from 1986 to 1992.

I acknowledge Mr. A. Vorster of the Engineering Faculty, Rand Afrikaans University, for valuable discussions.

I wish to thank Mr. A. Chtcherbakov of Sensors Sources and Signal Processing Research Group, Materials Laboratory, Rand Afrikaans University, for his inputs.

Ms. E. Burger of SABAX (Pty) Ltd., is thanked for the use of their Perkin Elmer 1600 spectrophotometer.

Mr. B. Monard and Mr. F. Denner of Production Technology, CSIR, are thanked for the use of their Hitachi model 3400 UV-VIS-NIR spectrophotometer.

I am thankful to the graduate students of the Sensors Sources and Signal Processing Research Group, Materials Laboratory, Rand Afrikaans University, for their support and friendship.

I would also like to express my appreciation to my wife, Assia, for her enormous patience, understanding and encouragement during these two years.

Finally, I wish to thank the Foundation for Research Development and Rand Afrikaans University for their financial support.

CONTENT

	Page
1. INTRODUCTION	
1.1 Inhomogeneous optical coatings	1
1.2 Goal of the research	2
References for chapter 1	6
2. THE ELECTRON CYCLOTRON RESONANCE PLASMA ENHANCED CHEMICAL VAPOUR DEPOSITION OF SiO_xN_y	
2.1 Introduction	11
2.1.1 Plasma and plasma parameters	12
2.1.2 ECR microwave plasmas	23
2.1.3 The generation of active species in a plasma	26
2.1.4 PECVD fundamentals	30
2.2 The ECR apparatus	35
2.3 The ECR-PECVD deposition system	35
2.4 The deposition of SiO_x , SiN_x and SiO_xN_y	40
2.4.1 Sample preparation and characterization	41
2.4.2 The deposition of SiO_x	42
2.4.3 The deposition of SiN_x	45
2.4.4 The deposition of SiO_xN_y	49
2.5. Conclusions	57
References for chapter 2	58

3.	THE OPTICAL PROPERTIES OF ECR-DEPOSITED FILMS OF SiO_xN_y	
3.1	Introduction	65
3.2	The properties of optical materials	66
3.3	The optical transmission spectroscopy	72
3.4	Theory for the determination of band gap	82
3.5	Description of the software	83
3.6	The optical properties of the substrates	84
3.7	The optical properties of SiO_x	86
3.8	The optical properties of SiN_x	91
3.9	The optical properties of SiO_xN_y	96
3.10	Conclusions	101
	References for chapter 3	103
4.	THE BASICS OF THIN FILM OPTICS AND DESIGN TECHNIQUES FOR GRADED REFRACTIVE INDEX OPTICAL COATINGS	
4.1	Introduction	106
4.2	The basics of thin films optics. The matrix method	109
4.3	Inhomogeneous optical coatings. Design techniques	118
4.4	Conclusions	140
	References for chapter 4	141

5.	THE APPLICATION OF GRADED REFRACTIVE INDEX SiO_xN_y LAYERS FOR THE FABRICATION OF OPTICAL COATINGS	
5.1	Introduction	146
5.2	ECR-PECVD for the fabrication of inhomogeneous optical coatings	154
5.3	Rugate filters	156
5.3.1	Single-band SiN_x rugate filter on silicon	157
5.3.2	Double-band SiN_x rugate filter on silicon	160
5.3.3	Single-band SiO_xN_y rugate filter on glass	162
5.3.4	Gaussian antireflection coating on silicon	166
5.4	Multilayer filters	169
5.4.1	Three-layer antireflection coating on silicon	169
5.4.2	Beamsplitter on glass	171
5.4.3	The multilayer high-reflection filter on glass	173
5.5	Conclusions	176
	References for chapter 5	177
6.	CONCLUSIONS	
6.1	Discussion	182
6.2	Recommendation for further research	187
	References for chapter 6	189

CHAPTER 1

INTRODUCTION

1.1 Inhomogeneous optical coatings

Modern vacuum deposition technology is used broadly for the production of optical thin films¹. The current situation is characterized by the introduction into the optical coatings manufacturing technology of a number of processing techniques developed in the microelectronics industry. Techniques such as molecular beam deposition (MBD)², organometallic vapour phase epitaxy (OMVPE)³, neutral cluster beam deposition (NCBD)⁴, low-voltage reactive ion plating (LV-RIP)⁵, ion beam assisted deposition (IBAD)⁶ and the wide range of plasma-stimulated processes⁷⁻¹² are being added to traditional techniques such as magnetron and reactive magnetron sputtering (MS)¹³, electron beam evaporation (EBE)¹⁴ and thermal evaporation (TE)¹⁵. These new techniques have created a totally new situation for optical engineers working on the development of optical coatings technology, in that, for the first time now, they have enabled engineers to tailor the deposition technique to the requirements of a specific application.

Optical coatings with graded refractive index profiles, and rugate filters in particular, have been rousing considerable interest in recent years¹⁶⁻²⁸. The flexible optical properties of these filters, the possibility to form multiple reflecting bands, the ability independently to adjust main parameters, as well as their expected high laser damage threshold, are very attractive features for various applications. However, contrary to the highly developed design procedures available¹⁶⁻²⁰, manufacturing technologies are far from ideal at the moment²¹⁻²⁸.

1.2 Goal of the research

This research project is aimed at developing a new technique for the fabrication of graded refractive index optical coatings.

Electron cyclotron resonance plasma enhanced chemical vapour deposition (ECR-PECVD) is a modern and effective tool for the fabrication of structures with complicated refractive index profiles^{8,29-31}. One of the materials that can be used for visible and near-infrared filters is SiO_xN_y , where x and y are varied according to a chosen design. The precursors, SiH_4 , O_2 and N_2 , are readily available in the form of electronic grade gases in any required degree of dilution. The optical properties of this material can be adjusted by merely controlling the process variables. SiO_xN_y could have a refractive index as low as that of SiO_2 , yielding a wide range of refractive indices, from 1.46 to 3.3 at the wavelength of 1 μm .

The design and manufacturing of thin film optical filters demand thorough knowledge of the optical parameters of the films over a wide wavelength range. In the case of homogeneous refractive index layers, which are used in, for example, multilayer quarterwave stacks, tables containing optical data for a large number of materials are readily available³²⁻³⁴. Vendors provide materials with known and certified parameters for sputtering, and for electron beam and thermal evaporation.

For advanced rugate-type filters, and for optical coatings in general, continuously varying refractive index profiles are often required. Material is being synthesized successively during the deposition process. The optical properties of such layers are process dependent and seldom well characterized. Consequently, an in-depth study of the optical properties of the depositing material is vital, becoming an obligatory part of the development of the technology.



Thus, the object of the research can be defined as though consisting of two inextricably united parts. The first part of the research will consist of an in-depth study of the optical parameters obtainable in the ECR-PECVD deposited SiO_xN_y -system, whereas the second part will consist of the development of the deposition technique for the controlled and reproducible fabrication of any custom-designed refractive index profile.

In chapter 2, short reviews are given of plasmas and the principles of plasma enhanced chemical vapour deposition. The main characteristics of ECR-PECVD are also

described. In addition, the experimental computer-controlled vacuum deposition system is described and characterized. The deposition of SiO_x , SiN_x and SiO_xN_y thin films by ECR-PECVD is studied for different process conditions. The growth rate dependencies on gas flow ratio, self-bias, pressure and magnetic field are also discussed. Fourier transform infrared spectroscopy is applied in order to investigate the compositional changes in the growing film with a change in the gas phase content. Raman spectroscopy is applied for the determination of microstructure of these thin films.

Chapter 3 comprises a discussion of the application of transmission spectroscopy for the determination of the optical properties of thin films. By this means, the optical properties of SiO_xN_y alloys deposited at different experimental conditions are studied. Refractive index, extinction and absorption coefficients, band gap and Urbach tail energies are calculated and compared with previously published results. The influence of the composition of the gas phase on these optical properties is discussed.

Chapter 4 briefly reviews the fundamentals of thin film optics and gives a summary of synthesis procedures for inhomogeneous optical coatings design. We discuss variation of the flexible Fourier transform design technique and present design examples. A 50/50 beamsplitter is designed by several approaches based on the Fourier transform relationship between transmittance and refractive index profile and results are compared. Optimization of the design is achieved by successive approximations and correction of the target transfer function. An alternative design procedure particularly suitable for the design of narrow band rugate filters which takes account of dispersion of complex refractive index and absorption in the material is also discussed.

Chapter 5 discusses deposition techniques for the manufacturing of inhomogeneous optical coatings and outlines the advantages of ECR-PECVD. A feasibility study of the proposed technique is undertaken and experimental confirmation is given. We report on the design and growth by ECR-PECVD of rugate filters for one and two reflecting bands. These filters are grown on silicon and glass substrates using silane, oxygen and nitrogen as gas precursors. In the discussion experimental results are compared with those of simulations. Inhomogeneous Gaussian antireflection coatings on silicon are also designed, grown and evaluated. For confirmation of the compatibility of the proposed optical thin film deposition technique with the classical design ideology which is based on the quarterwave multilayer stack, a high reflection filter on glass, three-layer antireflection coating on silicon and a neutral 50/50 beamsplitter on glass are designed and manufactured. Finally, an evaluation is given of the results.

Results of the study, as well as the advantages and disadvantages of the proposed deposition technique are discussed in chapter 6. Recommendations for future research are made.

REFERENCES FOR CHAPTER 1

1. H.A. Macleod, *Thin Film Optical Filters*, 2nd ed., Adam Higler Ltd., Bristol, 1986.
2. K.L. Lewis, I.T. Muirhead, A.M. Pitt, A.G. Cullis, N.G. Chew, A. Miller, and T.J. Wyatt-Davies, "Molecular beam deposition of optical coatings and their characterization", *Applied Optics*, Vol. 28, No. 14, 1989, pp. 2785-2791.
3. H. Sankur, W. Southwell, R. Hall and W.J. Gunning, "Rugate filter deposition by the OMVPE technique", in Optical Interference Coatings Technical Digest, 1992 (Optical Society of America, Washington, D.C., 1992) Vol. 15, pp. 125-127.
4. R. Overend, D.R. Gibson and R. Marshall, and K. Lewis, "Rugate filter fabrication using neutral cluster beam deposition", *Vacuum*, Vol. 43, No. 1/2, 1992, pp. 51-54.
5. A.J. Waldorf, J.A. Dobrowolski, B.T. Sullivan, and L.M. Plante, "Optical coatings deposited by reactive ion plating", *Applied Optics*, Vol. 32, No. 28, 1993, pp. 5583-5593.
6. E.P. Donovan, D. Van Vechten, A.D.F. Kahn, C.A. Carosella and G.K. Hubler, "Near infrared rugate filter fabrication by ion beam assisted deposition of $\text{Si}_{(1-x)}\text{N}_x$ films", *Applied Optics*, Vol. 28, No. 14, 1989, pp. 2940-2944.
7. A.G. Greenham, B.A. Nichols, R.M. Wood, N. Nourshargh and K.L. Lewis, "Optical interference filters with continuous refractive index modulations by microwave plasma-assisted chemical vapour deposition", *Optical Engineering*, Vol. 32, No. 5, 1993, pp. 1018-1023.

8. P.V. Bulkin, P.L. Swart and B.M. Lacquet, "Electron cyclotron resonance plasma deposition of SiN_x for optical applications", *Thin Solid Films*, Vol. 241 No. 1&2, 1994, pp. 247-250.
9. K. Sheach, R. Heinecke, "Pulsed plasma deposition of optical filter structures", in Optical Interference Coatings Technical Digest, 1992 (Optical Society of America, Washington, D.C., 1992), Vol. 15, pp. 128-130.
10. M. Heming, J. Hochaus, J. Otto and J. Segner, "Plasma impulse chemical vapour deposition - a novel technique for optical coatings", in Optical Interference Coatings Technical Digest, 1992 (Optical Society of America, Washington, D.C., 1992), Vol. 15, pp. 296-298.
11. S. Lim, J.H. Ryu, J.F. Wager, L.M. Casas, "Inhomogeneous dielectrics grown by plasma-enhanced chemical vapor deposition", *Thin Solid Films*, Vol. 236, No. 1&2, 1993, pp. 64-66.
12. J.C. Rostaing, F. Coeuret, B. Drevillon, R. Etemadi, C. Godet, J. Huc, J.Y. Parey and V.A. Jakovlev, "Silicon-based, protective transparent multilayer coatings deposited at high rate on optical polymers by dual-mode MW/r.f. PECVD", *Thin Solid Films*, Vol. 236, No. 1&2, 1993, pp. 58-63.
13. J.A. Dobrowolski, J.R. Pekelsky, R. Pelletier, M. Ranger, B.T. Sullivan and A.J. Waldorf, "Practical magnetron sputtering system for the deposition of optical multilayer coatings", *Applied Optics*, Vol. 31, No. 19, 1992, pp. 3784-3789.
14. J.D. Traylor, W.T. Pawlewicz, "Optical and durability properties of Bi_2O_3 , Cr_2O_3 , HfO_2 , Ta_2O_5 , Y_2O_3 and ZrO_2 ", in Optical Interference Coatings Technical Digest, 1992 (Optical Society of America, Washington, D.C., 1992), Vol. 15, pp. 175-177.

15. T.I. Oh, "Infrared minus-filter coatings: Design and production", *Applied Optics*, Vol. 30, No. 31, 1991, pp. 4565-4573.
16. E. Delano, "Fourier synthesis of multilayer filters", *Journal of the Optical Society of America*, Vol. 57, No. 12, 1967, pp. 1529-1533.
17. W.H. Southwell, "Using apodization functions to reduce sidelobes in rugate filters", *Applied Optics*, Vol. 28, No. 23, 1989, pp. 5091-5094.
18. B.G. Bovard, "Rugate filter theory: an overview", *Applied Optics*, Vol. 32, No. 28, 1993, pp. 5427-5442.
19. H. Fabricius, "Gradient-index filters: designing filters with steep skirts, high reflection, and quintic matching layers", *Applied Optics*, Vol. 31, No. 25, 1992, pp. 5191-5196.
20. P.G. Verly, J.A. Dobrowolski, W.J. Wild, and R.L. Burton, "Synthesis of high rejection filters with the Fourier transform method", *Applied Optics*, Vol. 28, No. 14, 1989, pp. 2864-2875.
21. S. Lim, J.H. Ryu, J.F. Wager, and T.K. Plant, "Rugate filters grown by plasma-enhanced chemical vapor deposition", *Thin Solid Films*, Vol. 245, No. 1&2, 1994, pp. 141-145.
22. C.S. Bartholomew, H.T. Betz, J.L. Grieser, R.A. Spence, and N.R. Murarka, "Rugate filters by laser flash evaporation of Si_xN_y on room temperature polycarbonate", *SPIE Proceedings*, Vol. 821, *Modelling of Optical Thin Films*, 1987, pp. 198-204.

23. P.V. Bulkin, P.L. Swart and B.M. Lacquet, "ECR plasma CVD for rugate filters manufacturing", SPIE Proceedings, Vol. 2253, Optical Interference Coatings, 1994, pp. 462-469.
24. W.J. Gunning, R.L. Hall, F.J. Woodberry, W.H. Southwell, and N.S. Gluck, "Codeposition of continuous composition rugate filters", Applied Optics, Vol. 28, No. 14, 1989, pp. 2945-2948.
25. S.P. Fisher, J.F. Leonard, I.T. Muirhead, G. Buller and P. Meredith, "The fabrication of optical devices by molecular beam deposition technology", in Optical Interference Coatings Technical Digest, 1992 (Optical Society of America, Washington, D.C., 1992), Vol. 15, pp. 131-133.
26. J. Allen, B.D. Herrington, S. Jansen and J.C. Blomfield, "Graded rugate filters for head up displays", in Optical Interference Coatings Technical Digest, 1992 (Optical Society of America, Washington, D.C., 1992), Vol. 15, pp. 134-136.
27. J.P. Heuer, J.P. Eblen, R.L. Hall and W.J. Gunning, "Scale-up considerations for codeposited gradient index optical thin film filters", in Optical Interference Coatings Technical Digest, 1992 (Optical Society of America, Washington, D.C., 1992), Vol. 15, pp. 122-124.
28. J. H. Campbell, J.L. Emmett, R.M. Brusasco, F. Rainer, R.T. Kersten, V. Paquet and H.-W. Etzkorn, "Damage resistant optical coatings prepared using high temperature, plasma chemical-vapor deposition", in Laser Induced Damage in Optical Materials: 1989, Lawrence Livermore National Laboratory report UCRL-101769.

29. P.V. Bulkin, P.L. Swart, B.M. Lacquet and F.J. Burger, "Electron cyclotron resonance plasma deposition for multilayer structures of silicon nitride on silicon", South African Journal of Physics, Vol. 16, No. 1&2, 1993, pp. 33-36.
30. S. Dzioba and R. Rousina, "Dielectric thin film deposition by electron cyclotron resonance plasma chemical vapor deposition for optoelectronics", Journal of Vacuum Science and Technology B, Vol. 12, No. 1, 1994, pp. 433-440.
31. P.V. Bulkin, P.L. Swart and B.M. Lacquet, "Properties and applications of electron cyclotron plasma deposited SiO_xN_y films with graded refractive index profiles", accepted for publication in "Journal of Non-Crystalline Solids".
32. E.D. Palik (Editor), Handbook of Optical Constants of Solids, Academic Press, Orlando, Florida, 1985.
33. E.D. Palik (Editor), Handbook of Optical Constants of Solids II, Academic Press, San Diego, California, 1991.
34. W.L. Wolf, "Properties of Optical Materials", in Handbook of Optics (Eds. W.G. Driscoll and W. Vaughan), McGraw-Hill, New York, 1978, pp. 7.1-7.157.

CHAPTER 2

THE ELECTRON CYCLOTRON RESONANCE PLASMA ENHANCED CHEMICAL VAPOUR DEPOSITION OF SiO_xN_y

2.1 Introduction

High-density plasma sources are finding widespread use in many new processing applications. Microwave electron cyclotron resonance (ECR) sources¹⁻⁵, radio-frequency (RF) helicon^{6,7} and induction⁸ (for instance, transformer-coupled plasma⁹) sources are now commonly used for plasma etching, low-temperature deposition, and surface treatment. Among the various deposition processes, ECR plasma enhanced chemical vapour deposition (ECR-PECVD) can be distinguished by several features: plasma enhancement, utilization of the ECR effect, low pressure, heterogeneous reaction mode and flexible control over the intensity of the ion bombardment. Because very complex processes are involved in ECR-PECVD, a brief review of these processes is needed in order to understand how they interact with one another and how they influence on the properties of growing films.

2.1.1 Plasma and plasma parameters

A plasma can be defined as a gas that contains charged and neutral species¹⁰. It usually consists of electrons, positive ions, negative ions, atoms and molecules. On average, a plasma is electrically neutral, because any charge imbalance would result in the formation of electric fields that would tend to move charges in such a way as to eliminate the imbalance¹¹. As a result, the combined density of electrons and negative ions will be equal to that of positively charged ions. This property of a plasma is called quasi-neutrality. Plasma can be characterized by two important parameters. The first parameter is plasma density, n_e , which is the concentration of charged species. The second parameter is the plasma temperature T_e in energy units (usually in eV, 1 eV = 11600 K). The plasma density for known plasmas may vary between 10^0 cm^{-3} and 10^{28} cm^{-3} , the plasma temperature may vary "only" by seven orders of magnitude (typically from 0.1 eV to 10^6 eV)¹⁰.

An important numerical characteristic of the plasma is the degree of ionization, which is the fraction of the original neutral species (atoms and molecules) which has been ionized¹¹. Plasmas with a degree of ionization much less than unity are referred to as "weakly ionized" plasmas¹⁰. The presence of a large population of neutral species will dominate the behaviour of this type of plasma. In fully ionized plasmas, the degree of ionization approaches unity, and neutral particles play some or no role.

Creating and maintaining the plasma requires some energy source to produce the ionization. In steady state, the rate of ionization will be balanced by the losses of

ions and electrons from the plasma volume via recombination and diffusion or via convection to the walls. The plasmas used in technology are initiated and sustained mainly by electric fields. Direct-current (DC) or alternating-current (AC) power supplies are used for these purposes. Typical AC frequencies of excitation are 100 kHz at the low end of the spectrum, 13.56 MHz in the radio frequency (RF) range of the spectrum and 2.45 GHz in the microwave region. These plasmas are sometimes also referred to as "electric", "gaseous" or "glow" discharges.

The extensive use of plasmas for the deposition and etching of thin films derives from two of their well-known features¹¹. Firstly, plasmas are sources of chemically active species. The generation of chemically active species in a plasma is initiated by the electron bombardment of molecules and atoms. Plasma electrons are accelerated by the electric fields and are gaining sufficient energy to break chemical bonds. The products of these electron bombardment processes include radicals and ions. They can undergo further reactions, often at high rates, to form additional chemically reactive species. The second feature that makes plasma discharges so useful for deposition and etching is their ability to generate ions and to accelerate ions to energies of 50 to 1000 eV in the vicinity of the substrate. Energetic ions play a synergetic role in the deposition and etching processes, and a determining role in sputtering processes.

In addition to the plasma density, plasma temperature and degree of ionization, other important parameters of the plasma are the Debye length d , the mean free path λ and the Larmor radius r_L . In a plasma, there can be many mean free paths, because

there are many different types of particles (various neutral species, electrons and ions)¹². Of primary interest are the mean free paths for collisions between electrons and heavy particles λ_e and ions and heavy particles λ_D .

If a magnetic field exists in a plasma, charged particles will tend to gyrate about the magnetic field between collisions. The radius of the circular path it takes is called the Larmor radius and is expressed as¹²

$$r_L = \frac{v_T m}{qB} \quad (2.1)$$

where v_T = the local velocity of the charged particle normal to the magnetic field line,

m = the mass of the charged particle,

q = electric charge of the particle, and

B = strength of the magnetic field.

Obviously, the mass of an electron is much smaller than the mass of a heavy ion, so the Larmor radius for electrons will be much smaller than that for ions. Therefore, if we operate a glow discharge in the presence of a magnetic field, the electrons will, in general, be confined by the magnetic field, whereas the ions will not be affected. However, it is difficult to create any significant charge separation in a plasma, so confining the electrons has the effect of confining the ions as well. It is important to note, however, that neutral particles (including free radicals) will not be influenced by the magnetic field.

The Debye length d in a plasma is a distance over which the potential perturbation is reduced to 0.37 (one over base of natural logarithms) of its initial value. It is given by

$$d = \left(\frac{kT_e \epsilon_0}{e^2 n_e} \right)^{1/2} \quad (2.2)$$

where ϵ_0 = the permittivity of free space, and

e = the unit charge of an electron.

k = Boltzmann's constant.

For low-pressure discharges, where n_e can be quite small, the Debye length can be large and the sheath region along a surface (where significant charge separation occurs) can extend a considerable way into the plasma. The number of electrons in a Debye sphere, N_D , used to be the criterion for plasma existence. If $N_D \gg 1$, the medium can be called a plasma. For plasmas used in thin film technology, the relevant range of d is from 0.01 to 1 mm, with 0.1 mm being a good average for weakly ionized discharges, and the value of N_D varies from about 10^4 to 10^7 , which value easily satisfies the definition of a plasma.

Electrons in a plasma have a distribution of energies, and typically average electron energy is used. For plasmas of interest to this work¹², the electrons may be assumed to have a Maxwellian distribution, which is described¹¹ in terms of the electron energy E ,

$$f(E) = \frac{2\sqrt{E}}{\sqrt{\pi}(kT_e)^{3/2}} \exp\left(-\frac{E}{kT_e}\right) \quad (2.3)$$

where $f(E)$ = the electron energy distribution function (EEDF) which gives the fraction of the total number of electrons with energy between E and $E+dE$, and

The electron energy is given by

$$E = \frac{1}{2}m_e v_e^2 \quad (2.4)$$

where m_e = the electron mass and
 v_e = the magnitude of the electron velocity.

The EEDF is normalized in such a way that if we integrate over all energies, we get:

$$\int_0^{\infty} f(E)dE = 1 \quad (2.5)$$

A Maxwellian distribution is isotropic¹⁰, thus the average energy can be obtained by the following integral:

$$\int f(E)EdE = \frac{3}{2}kT_e \quad (2.6)$$

Therefore, the electron temperature T_e (in energy units) for a Maxwellian electron energy distribution is a measure of the average energy of electrons.

The Maxwellian distribution is also called the "equilibrium distribution", because it represents the case where the electrons are in thermodynamic equilibrium. It should, however, be pointed out, that ions and electrons are characterized by different Maxwellian distributions with different temperatures T_i and T_e . Although $f(E)$ in weakly ionized plasmas is not Maxwellian¹¹, it is still common to speak of an "electron temperature" when referring to the average electron energy.

Several potentials are important in the glow discharges used in thin film deposition: the plasma potential, the floating potential, and the sheath potential. The plasma potential (V_p) is the potential of the glow region of the plasma. It is essentially uniform throughout the volume of the glow discharge and is the most positive potential in the vessel containing the plasma.

The floating potential (V_f) is the potential of an electrically floating surface in contact with the plasma. Equal fluxes of negatively and positively charged species arrive at such surface. The difference between V_p and V_f is approximately given by¹²:

$$V_p - V_f = \frac{kT_e}{2e} \ln \left(\frac{m_i}{2.3m_e} \right) \quad (2.7)$$

where m_i is the ion mass. Equation (2.7) can be used to estimate the maximum energy with which positive ions may bombard electrically insulated chamber walls. Most threshold energies for sputtering are 20 to 30 eV. Therefore, a $V_p - V_f \leq 20$ to 30 V (depending on material) would avoid sputtering of the walls which may lead to film contamination¹².

The plasma potential is always positive with respect to any surface in contact with the plasma. This is due to the fact that the mobility of the free electrons in the plasma is much greater than that of ions. This results in the initial electron flux to all surfaces being much greater than the ion flux. Consequently, the surfaces in contact with the plasma become negatively charged and, owing to Debye screening, a positive space charge layer, or sheath, develops in front of these surfaces. Concentration of electrons in this layer is lower than in the plasma volume. Fewer gas species are therefore excited by electron collisions, and fewer species relax and give off radiation. That is why the sheath region is dark relative to the glow discharge and it is sometimes referred to as "dark space". Positive ions that enter the sheaths from the glow region by random thermal motion accelerate into the electrodes and other surfaces in contact with the plasma. Thus, all the surfaces surrounding the glow discharge experience a certain amount of positive ion bombardment, including walls and fixtures in a vacuum chamber. Similarly, secondary electrons emitted from the surfaces (for example, owing to positive ion bombardment) accelerate through the sheaths into the glow region. The maximum energy with which positive ions bombard a surface, and the maximum energy with which secondary electrons enter the glow region, are determined by the difference between the potential of the surface and the plasma potential. Because this is the potential across the sheath, it is usually referred to as the "sheath potential".

In all advanced types of plasma processing systems for thin film etching and deposition (ECR, transformer coupled plasma, helical and helicon resonators, magnetically enhanced PECVD, etc.) plasma excitation is separated from substrate

bias to allow independent control of ion energy¹³. Figure 2.1 schematically shows an RF generator being connected to the substrate holder of a PECVD system via a low-impedance blocking capacitor¹⁴.

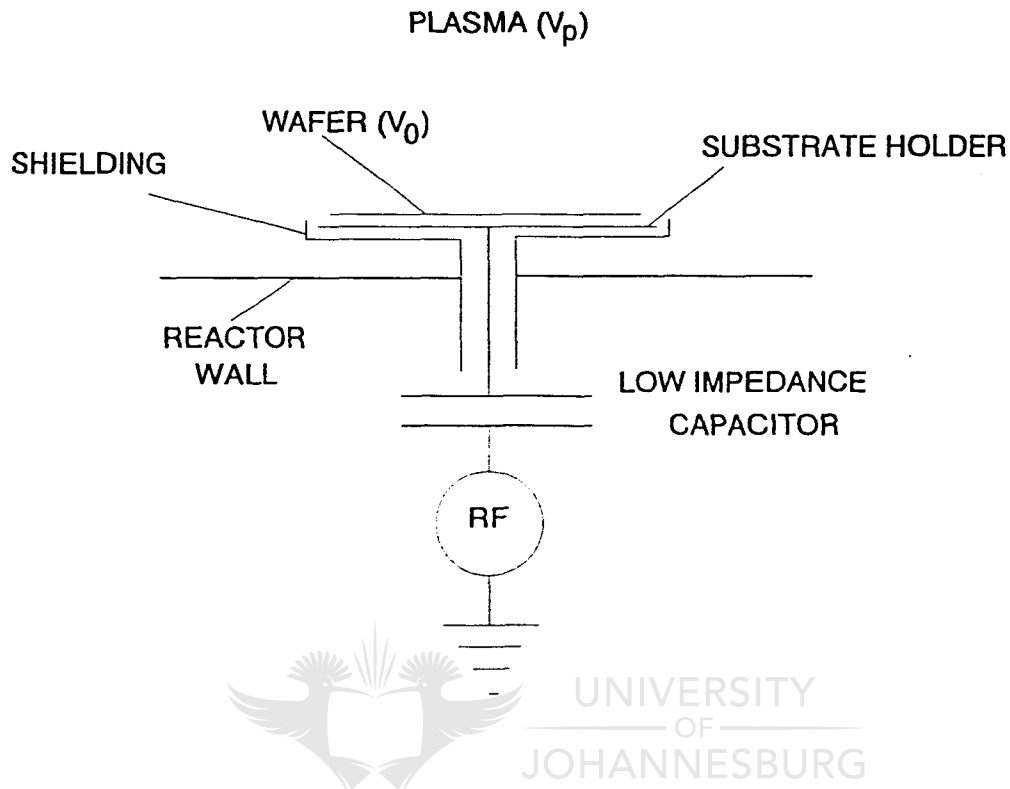


Figure 2.1: A schematic representation of RF biasing¹⁴

We know that a probe at floating potential draws no net current. If a voltage is applied to the probe, the current drawn will be given by the probe current-voltage (I-V) characteristic. Figure 2.2 (a) shows that when a probe is given an RF perturbation symmetrically about its initial value, the asymmetry of the probe I-V characteristic causes the substrate to draw a net electron current. This charges the substrate to a mean negative value with respect to the floating potential, so as to draw a net zero current as shown in Figure 2.2(b)¹².

The derivation of the magnitude of the bias can be performed if one accepts several hypotheses to be valid:

1. The plasma is unbounded.
2. The electron distribution is Maxwellian.
3. There are no collisions in the plasma sheath.
4. All charges impinging the surface are collected.
5. There is no generation of secondary electrons.

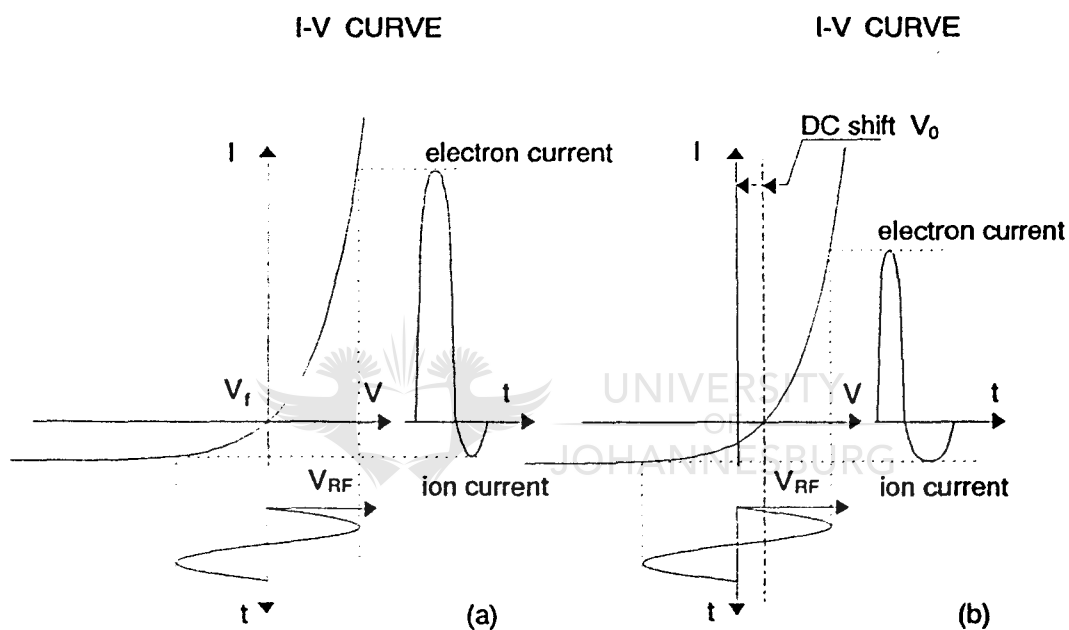


Figure 2.2: Self-biasing mechanism of a dielectric surface¹²: (a) RF biasing has been just applied, (b) after compensation by DC shift.

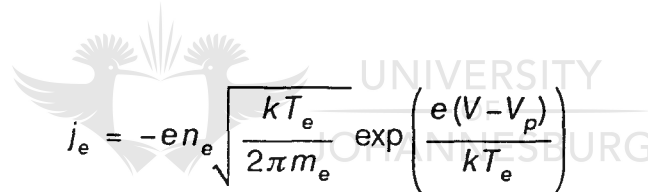
In this case, provided that the radius of curvature of those surfaces in contact with the plasma is much larger than the Debye length, we can consider the substrate to be a large plane probe. When the surface is biased positively with respect to the plasma

potential V_p ($V > V_p$), the ions are repelled and an electron sheath is created. The electron saturation current density will be proportional to the random thermal flux of electrons, thus independent of the bias magnitude and given by¹⁴

$$j_{es} = -en_e \frac{v_{ea}}{4} = -en_e \sqrt{\frac{kT_e}{2\pi m_e}} \quad (2.8)$$

where v_{ea} is the average thermal velocity of electrons.

When the surface is biased negatively ($V < V_p$), part of the electrons are repelled and an ion sheath is created; only electrons that have energies high enough to cross the potential barrier $V-V_p$ are collected by the substrate. As a result, the electron current density is reduced to



$$j_e = -en_e \sqrt{\frac{kT_e}{2\pi m_e}} \exp\left(\frac{e(V-V_p)}{kT_e}\right) \quad (2.9)$$

For positive ions, and if $V < V_p$, the potential is attractive. The corresponding ion saturation current density j_{is} can be obtained by application of the approximation that is called the "Bohm criterion"¹²

$$j_{is} = en_i \sqrt{\frac{kT_e}{m_i}} \quad (2.10)$$

It can be shown¹⁴ that, assuming a zero electric charge collected on the substrate surface over a period T and a sinusoidal periodic signal V_{RF} , the value of the DC

component V_0 is given by

$$V_0 = V_f + \frac{kT_e}{e} \ln \left[I_0 \left(\frac{eV_{RF}}{kT_e} \right) \right] \quad (2.11)$$

where I_0 is the zero-order modified Bessel function. For $eV_{RF} \gg kT_e$, the asymptotic value of V_0 becomes¹⁴

$$V_0 = V_f - V_{RF} + \frac{kT_e}{2e} \ln \left(\frac{2\pi e V_{RF}}{kT_e} \right) \quad (2.12)$$

There are three types of electrical power dissipation mechanisms that can be encountered under DC or RF excitation between planar electrodes. These are illustrated in Figure 2.3¹⁵.

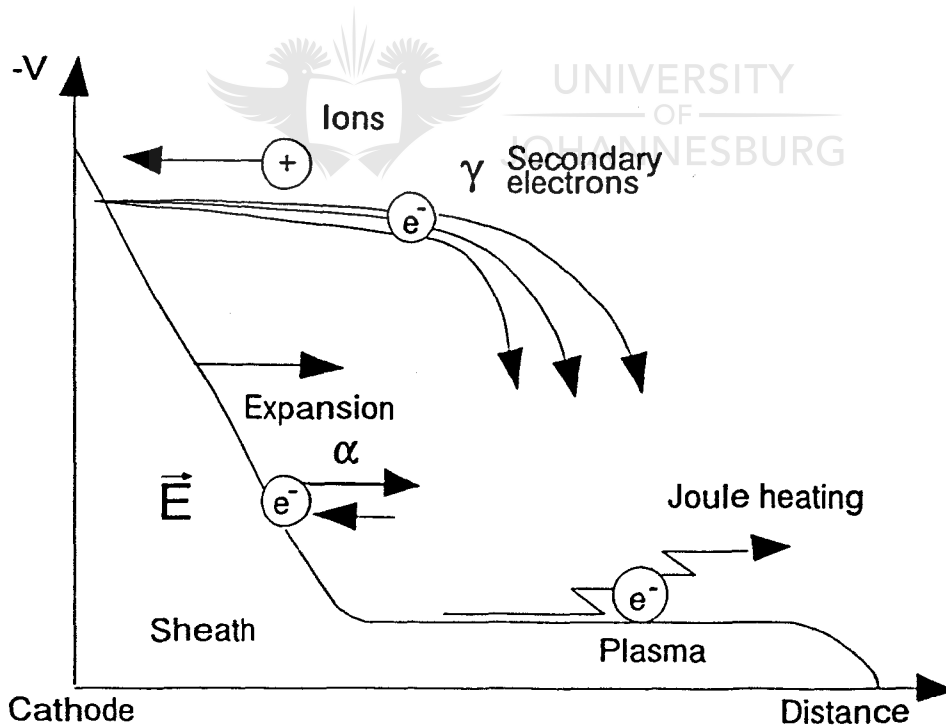
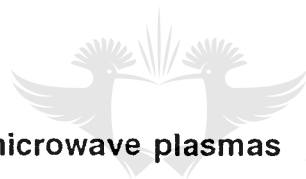


Figure 2.3: Power dissipation mechanisms in an electric discharge¹⁵

In the γ -regime, positive ions are accelerated towards the cathode. Secondary electrons (γ -electrons) are emitted by ion bombardment and accelerated through the sheath into the plasma region. This mechanism is the only way to sustain a DC discharge, but it is also dominant in RF discharge of electropositive gases at high voltage¹⁵. The α -regime occurs only in RF discharges: electrons are accelerated by "waveriding" on the expanding sheath edge during the negative half-cycle at the powered electrode, and the power dissipation is proportional to the square of the RF frequency¹⁵. The "Joule heating" mechanism occurs in the plasma bulk when a DC or RF field is present to maintain the electron conduction and ionization necessary to compensate for the electron losses due to electron attachment in electronegative gases. The power dissipation mechanisms in the ECR discharge will be discussed later in this chapter.

2.1.2

ECR microwave plasmas



UNIVERSITY
OF
JOHANNESBURG

Among the many phenomena that can occur in a plasma, one of the most interesting (from the point of view of discharges used for PECVD) is that of electron cyclotron resonance (ECR).

When a plasma is subjected to an alternating electric field (E) in the presence of a perpendicular static magnetic field (B), the electrons will receive energy from the electric field but will gyrate because of the magnetic field. Consider the arrangement shown in Figure 2.4 (magnetic field is normal to the page). Let us assume that an

electron is accelerated to the left by the time-varying electric field. If the frequency of the alternating electric field ω is equal to the cyclotron frequency of the electron

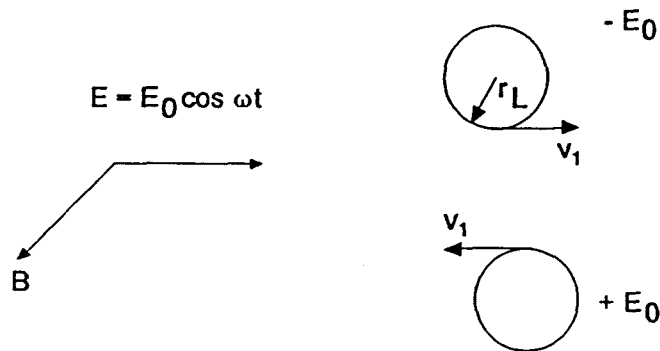


Figure 2.4: The principle underlying the electron cyclotron resonance phenomenon

ω_{ce} , the magnetic field will turn the electron around just in time again to be accelerated in the opposite direction by the time the electric field changes polarity. Thus, the electron gains energy as E oscillates in both directions (provided that there are many oscillations between collisions), and a resonant condition is created. The frequency given by Equation 2.13 provides us with the numerical value of the electron cyclotron frequency in a given magnetic field with strength B.

$$\omega_{ce} = \frac{eB}{m_e} \quad (2.13)$$

Good microwave energy coupling is directly related to a synchronization between the combined electron-neutral and electron-ion collision processes and the excitation frequency ω^5 . For different gases the optimum pressure range for efficient discharge

breakdown and maintenance with 2.45 GHz microwave energy usually occurs between 0.5 and 10 Torr. However, when a static magnetic field with strength equal to 875 Gauss is impressed on the energy coupling process, the electron cyclotron effect leads to very efficient energy transfer from the electric field directly to the electrons. For high pressures, very little resonance is seen, as electron collisions occur so frequently that the electron cannot be turned by the magnetic field in time to catch the reversing electric field. Under these conditions the process of heating of the electrons is purely collisional. At low pressures, there is a strong resonance, and ECR heating is taking place. For helium, for example, transition between the two heating regimes occurs between 3 Torr and 0.5 Torr⁵.

A steady-state microwave discharge is characterized by equality between the electromagnetic power absorbed by the plasma and power losses in the plasma volume⁵. The absorption process includes the microwave energy absorption by both the electron and ion gases. Owing to the fact that work done on a charged particle by an electric field between collisions varies inversely as the particle mass, the energy gained by the electron is much greater than the energy gained by the ion. Therefore, direct energy transfer from the field to the ions can be neglected and electromagnetic energy transfer to the plasma takes place through Joule (elastic and inelastic heating) and electron cyclotron heating of the electron gas.

Because at a certain plasma density, called the critical density n_c , an electromagnetic wave of frequency lower than ω is reflected from the plasma boundary, it is usually assumed that plasma electron and ion densities within the microwave discharges are

limited to less than the critical density, given by¹⁰

$$n_c = \frac{m_e \epsilon_0 \omega^2}{e^2} \quad (2.14)$$

or

$$n_c = 1.24 \times 10^{-2} f^2, \quad (2.15)$$

where f is the excitation frequency. This implies that, with 2.45 GHz excitation, plasma densities are limited to a maximum of $7.4 \times 10^{10} \text{ cm}^{-3}$. In practice, waveguide applicators produce slightly higher densities, and cavity applicators are capable of producing densities of 10 to 50 times the critical densities at low pressures, and densities above 100 times the critical density at high pressures⁵. The ability to produce high densities is due to evanescent wave penetration into the plasma. This type of coupling is greatly enhanced in cavity applicators because of their ability to impress a high, standing-wave electric field against the discharge without reflecting power from the applicator⁵.

2.1.3 The generation of active species in a plasma.

Active species (mainly ions and radicals) can be formed in a plasma by collisions between any sufficiently energetic particles. Collision processes can be broadly divided into elastic and inelastic types, depending on whether or not the internal energies of the colliding species are maintained. An elastic collision is one in which there is an interchange of kinetic energy only. An inelastic collision has no such

restriction, and internal energies change too. The phrase "internal energy" refers to electronic excitations in atoms or electronic, vibrational and rotational excitations in molecules.

There are always many mechanisms that cause the processes of generation and recombination of active species to take place, the most important of which are listed below¹⁶:

Electron impact ionization



Electron impact excitation



Dissociation



Electron attachment



Dissociative electron attachment



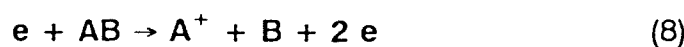
Relaxation (photoemission)



Charge transfer



Dissociative ionization



where A, B, AB = reactants (atoms or molecules),
 e = an electron,
 A^* = reactant A in an excited state,
 $h\nu$ = quantum of energy, and
 A^+, B^+, A^- = ions.

Which of these are most important for a specific PECVD process can be determined by studying corresponding reaction rates¹⁶.

One should point out that, in the case of ECR discharge, electron-electron elastic collisions also become very important owing to effective energy exchange (since masses are equal) and a high degree of ionization, hence EEDF will tend to be Maxwellian.

The rate at which these inelastic collisions create excited species, ions, free radicals, etc., can be estimated by using a reaction rate equation¹⁶. For example, the rate at which A^* is created from reaction (2) can be given by

$$\frac{d[A^*]}{dt} = k_2[A] \cdot [e] \quad (2.16)$$

where $d[A^*]/dt$ = the rate at which A^* is formed,
 k_2 = the reaction (2) rate coefficient,
 $[A]$ = the concentration of species A , and
 $[e]$ = the electron concentration.

Similar equations can be used to describe the reaction rates for any of the above-mentioned reactions.

Since only high-energy electrons can take part in inelastic collisions and in order to take this fact into account, k_2 in Equation 2.16 has to be defined in terms of the electron velocity and the inelastic collision cross-section. The cross-section of an electron-reactant inelastic collision is proportional to the probability that this inelastic collision will occur. It is a function of the electron energy. For example, the collision cross-section will be zero, if the energy of the electron is lower than a certain threshold energy. The rate coefficient k_i can be calculated by using the following equation¹⁶:

$$k_i = \int_0^{\infty} \sqrt{\frac{2E}{m_e}} \sigma_i(E) f(E) dE, \quad (2.17)$$



where σ_i is the collision cross-section of reaction i (it is a function of electron energy E). The integration should be carried out over all possible electron energies.

Unfortunately, most of the collision cross sections are not known^{13,17,18} and only some cross section data can be collected from literature. A similar situation exists with the electron energy distribution function (EEDF) $f(E)$. It is normal practice to assume a Maxwell-Boltzmann distribution for $f(E)$. However, the actual electron energy distribution function is not known. Moreover, it is possible that reactant composition of the gas can influence $f(E)$, because the higher-energy electrons lose a significant fraction of their energy in inelastic collisions with these reactants^{13,16}. It

is thus difficult theoretically to calculate reaction rate coefficients and reaction rates. Because the average electron energy is much higher than that of an ion, the PECVD environment is not in thermal equilibrium^{13,18}. Thermodynamics, therefore, is not able to predict the product of a PECVD reaction.

2.1.4 PECVD fundamentals

In thermally driven chemical vapour deposition (CVD), ground state species of precursors (for example, SiH_4 and NH_3 in thermal chemical vapour deposition of Si_3N_4) are transported to the wafer surface, undergo chemical reactions and surface migration and result in the growth of a silicon nitride film. Byproducts also form, desorb, diffuse away into the main gas stream and are transported out of the chamber. This classical sequence of steps is given below¹⁶:

1. Transportation of the reactants to the growth region.
2. Mass-transport of reactants to the wafer surface.
3. Adsorption of reactants.
4. Physical-chemical reactions yield the solid film and reaction byproducts.
5. Desorption of byproducts.
6. Mass-transport of byproducts to the main gas stream.
7. Transportation of byproducts away from the growth region.

The situation changes when a plasma is generated in a CVD environment. A fraction of the ground state precursor species undergoes electron impact dissociation and

excitation, resulting in the generation of highly reactive species. Thus, in addition to the ground state species, these highly reactive species also participate in the deposition process. They diffuse to the substrate, and undergo parallel processes of adsorption, chemical reactions, surface migration, etc. These highly reactive species create an alternative deposition pathway, which operates simultaneously with the existing thermal deposition pathway¹⁶. Because of lower activation energies (in comparison with ground-state precursors) and higher sticking coefficients, excited and ionized species react faster, and the plasma kinetic pathway often bypasses that of the ground state species. Consequently, the plasma enhancement makes a higher deposition rate possible¹⁶. Moreover, the ions present in the plasma bombard the substrate surface, further modifying the kinetic pathways, effecting the breakdown of weakly bonded reactive species, enhancing the surface migration of adatoms, etc.¹⁸

Let us consider an example of the practical implementation of plasma enhancement. The arrangements for the deposition of silicon oxynitride are shown schematically in Figure 2.5. ECR discharge, occurring when 2.45 GHz microwave radiation interacts with the magnetic field of 875 Gauss provided by permanent magnets (1), is used for remote excitation of nitrogen, oxygen and argon plasma. In this region highly reactive ions and radicals of precursors are formed. They are then transported with the assistance of a divergent magnetic field, created by the external magnetic coil (2), to the vicinity of the substrate. Silane is injected downstream through the gas distribution ring (3) placed near the substrate. In this way deposition on the chamber walls and silane consumption can be reduced. Discharge, occurring when the substrate holder (4) is RF-biased, makes its own contribution to the generation of

active species. The DC self-bias thus created provides control over the energy of ions bombarding the surface. The chemical reaction takes place at the surface of the substrate (5) which is fixed to the holder.

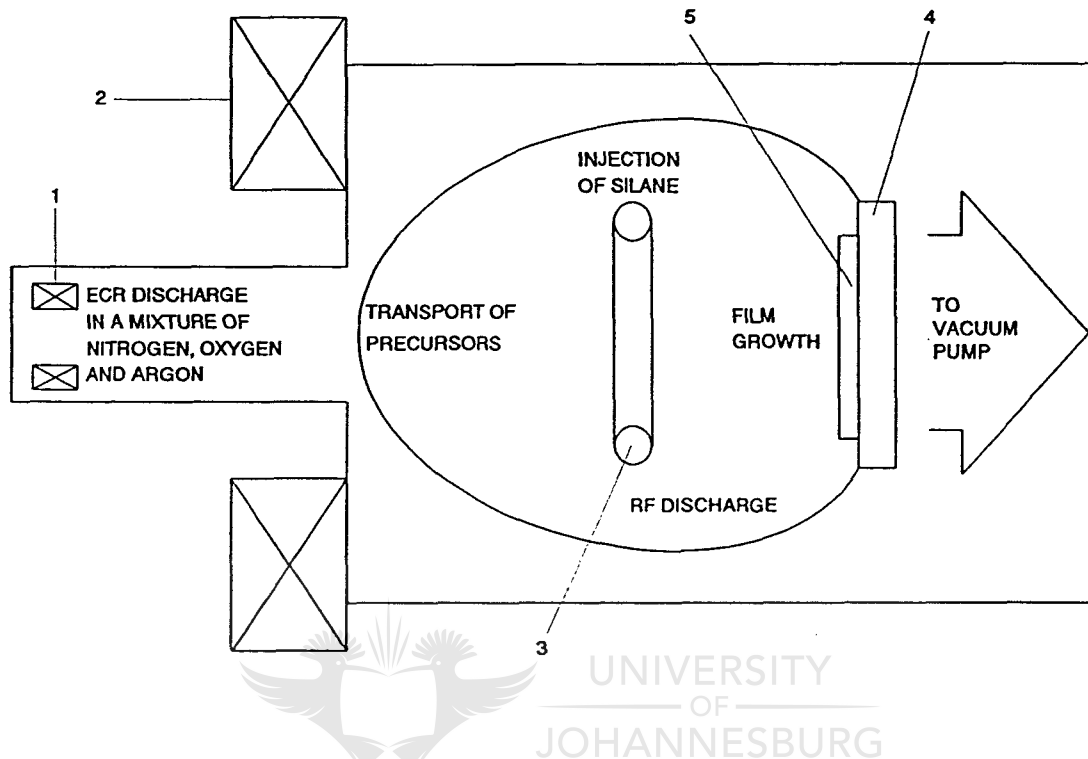


Figure 2.5: Downstream ECR-PECVD arrangements with remote plasma excitation and injection of silane in the vicinity of an RF-biased substrate

The ability of low-energy ions to enhance the precision of surface etching, cleaning and deposition processes, provides the basis for the interest in ion-assisted processes. Different applications of low-energy ion beams are illustrated in Figure 2.6. Low-energy ions assist in the surface processing of materials primarily through the kinetic energy they deposit as they slow down in the sample. The effects of this energy deposition can be divided into two categories, namely physical and chemical effects^{20-22,24,25}. The category of physical effects generally includes those effects

where the energy transferred in ion-atom collisions directly induces atomic motion or displacements, whereas the category of chemical effects includes those effects where the energy transfer enhances chemical reactivity. The physical effects may be understood simply in terms of ion-atom collisions, whereas the chemical effects of low-energy ions are more complex. They include directly stimulating reactions to form volatile species, and the removal of surface species to expose reactive sites on the surface.

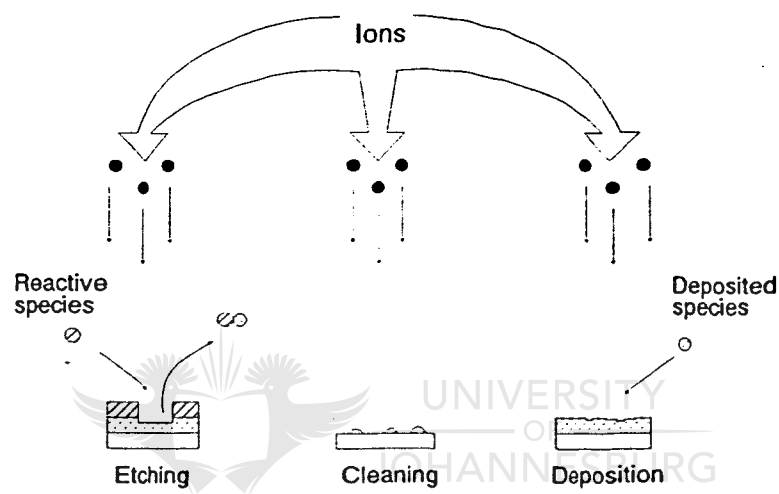


Figure 2.6: The participation of energetic ions in surface reactions²⁰

As was mentioned before, the plasmas are sources of both non-equilibrium gas phase and surface chemistry, and particle bombardment. Ion-surface interactions are present and play a significant role in many plasma-based thin film deposition techniques²⁰⁻²⁶. The net effect of the plasma utilization is that, very often, specific materials can be obtained at lower deposition temperatures and, as a result, a wide and controllable range of film properties can be attained in addition to new metastable structures or compositions²⁰⁻²⁵.

The requirement that the ions play a significant role in surface processing sets the energy scale of interest. For the ions to participate in chemical reactions, the transferred energy must be greater than bond energies, typically several electron volts, whereas atomic displacements are induced only when the energy deposited is greater than the atom displacement thresholds, typically between 10 and 25 eV²⁰⁻²². At the same time, the major fraction of the ion-induced displacements should be confined to the near surface region if the objective is to assist in surface processing; 10³ eV will be a practical high-energy limit for the incident ion energy^{20,21}.

Ion bombardment can be used advantageously during the different stages of thin films manufacturing. Substrate cleaning can be improved, using inert or reactive ion bombardment prior to deposition. Film adhesion (especially for metallic films) can be greatly improved with ion bombardment. At higher energies the substrate, as well as thin films, can be etched or milled. During deposition ion bombardment of thin films influences a number of film properties²⁶ including adhesion, morphology, stoichiometry, stress, impurity content and packing density. It allows flexible control over these properties, something that cannot be attained through any other enhancement technique. However, if ion energies, fluxes and/or doses are too high, they may also affect the film quality and should, therefore, be avoided¹⁶.

2.2 The ECR apparatus

Extensive research was carried out on electron cyclotron resonance discharges and their application to thin film processing²⁷⁻³⁴. ECR discharges have been demonstrated as useful, electrodeless, high-density sources of excited and charged species over 10^{-4} Torr- 10^{-2} Torr pressure regimes. ECR/microwave technology allows a number of different design approaches. Consequently, there are several different processing configurations available. Both waveguide^{1,3,27} and cavity applicators^{5,29} have been employed. Electron cyclotron resonance magnetic fields can be produced with coils^{1,24} or rare-earth magnets^{5,28}. Both low-energy plasmas and neutralized electron-ion beams can be produced for surface processing. Thus, specific applications may have one or more acceptable ECR approach, and/or very specific reactors can be designed for particular applications.



2.3 The ECR-PECVD deposition system

To study the deposition of optical coatings from the gas phase with ECR plasma enhancement, a small-scale computer-controlled ECR-PECVD system was designed and built³⁴.

The vacuum system consists of a pumping station, a main chamber, a compact ECR source and a gas distribution system. It is schematically represented in Figure 2.7. A Leybold-Heraeus 360 CSV turbomolecular pump, together with a TRIVAC D30A

rotary vane pump, was used to provide sufficient pumping speed and base pressure of less than 10^{-7} Torr in the chamber. A pneumatic gate valve was installed on the pumping port. A bypass line (not shown) allows loading/reloading of samples in the chamber while the turbomolecular pump is running.

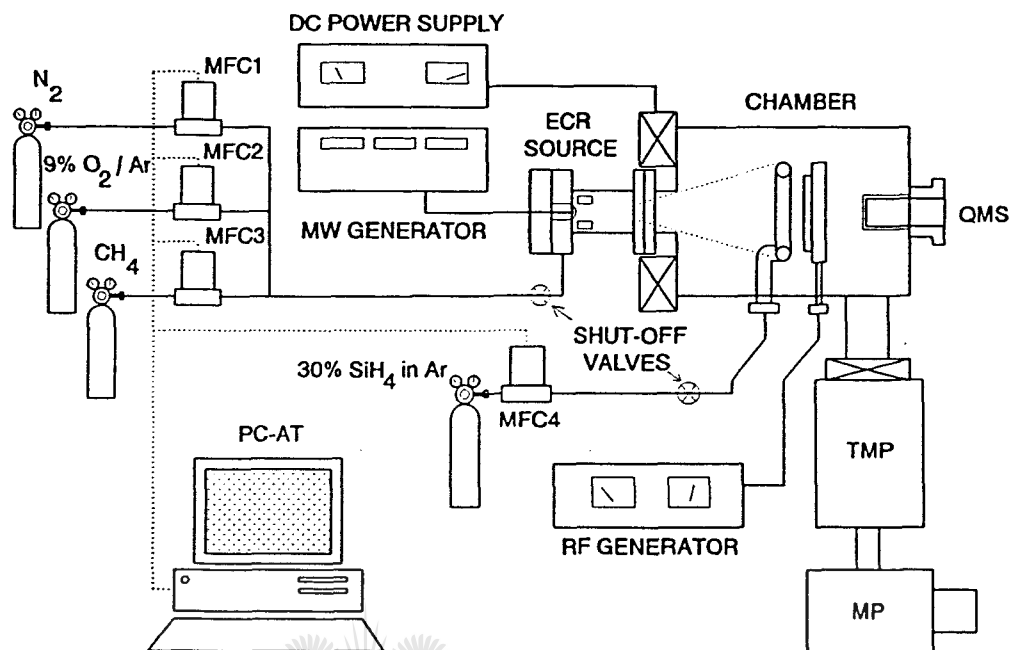


Figure 2.7: A schematic representation of a computer-controlled high-vacuum PECVD system equipped with a compact ECR source

The stainless steel high-vacuum chamber was equipped with two CF63 and several KF40 flanges to allow flexible installation of the ECR source, electrical and gas feedthroughs, a quadrupole mass spectrometer and vacuum gauges. Convectron gauges were used to monitor pressure during deposition and a cold cathode Penning gauge and mass spectrometer were employed for base pressure monitoring. Typical pumpdown time from atmosphere to $2 \cdot 10^{-7}$ Torr was 30 minutes. A substrate holder, made of aluminium and teflon and with RF/DC-biasing capabilities, holds the sample in a vertical position at variable distance from the source and at any chosen angle to

the direction of the plasma stream. A compact ECR plasma source was installed on the chamber in a horizontal position and equipped with an additional Tesla coil for the extraction of ions.

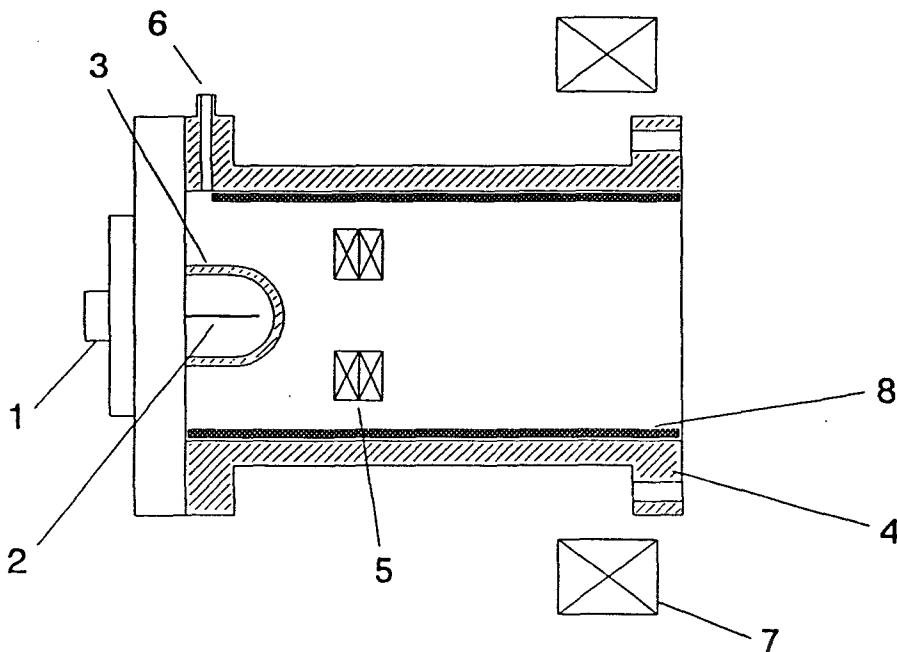


Figure 2.8: A schematic diagram of a compact ECR source²⁸

A schematic diagram of the compact ECR source²⁸ is shown in Figure 2.8. The microwave energy (2.45 GHz) is introduced to the discharge via a 50 Ohm standard microwave connector (1) by antenna (2), which is isolated from the vacuum by a ceramic cup (3). The stainless steel body of the ECR source (4) is water cooled. There are two standard CF63 flanges at the ends of the body, one of which is used for source connection to a high-vacuum chamber. Permanent SmCo₅ ring-shaped magnets (5) are placed inside the body and fixed with special rods to the third CF63 flange, where a microwave input assembly is mounted. The diameter of the antenna and the position of the magnets are adjusted to produce the most stable plasma discharge at the lowest microwave power possible.

Gases can be introduced through the VCR inlet (6) placed on one of the flanges of the source body. An external magnetic coil (7) is also used to increase extraction of the ions from the source with a divergent magnetic field. An optional quartz liner (8) can be inserted into the ECR source body to reduce ion/radical losses at the walls.

The total length of the compact ECR source is 160 mm, and its diameter is 114 mm. The whole construction is mounted on a standard CF63 flange, which makes it flexible and compatible with ordinary ultra-high vacuum equipment.

Several gas channels were used to deliver the gases into the chamber. One line was dedicated to deliver N_2 and 9% O_2 in Ar, and a separate line was used for 30% SiH_4 in Ar. The first line was used to feed the ECR source, while the second one introduced silane through a gas distribution ring placed close to the substrate holder. The correct position of the gas ring relative to the substrate was found to be very important for satisfactory uniformity and growth rate. The third gas channel is dedicated for backfilling of the system with nitrogen. There is also a fourth channel connected to a methane gas cylinder. It can be used for the deposition of carbon-containing materials, SiC for instance, in the same vacuum chamber. Filters were put in every gas line to ensure the absence of particles in the gas stream. Two Aalborg Instruments AFC-2600 mass flow controllers (MFC) with normally-closed control valves and a flow rate of up to 100 sccm, as well as two Tylan 2900 MFCs with a maximum flow rate of 50 sccm, are providing smooth changes of gas flows. Valves, mass flow controllers, filters and gas inlets were equipped with VCR-type fittings for maximum leak tightness. All tubing was chemically polished inside to ensure the

minimum outgassing capacity. Microwave energy was supplied to the source via a flexible coaxial line from the 2.45 GHz magnetron non-continuous wave generator. The manually controlled generator provides 0-800 W of microwave power to the quarterwave antenna isolated from the vacuum by a cap made of alumina ceramic, which is cooled with pressurized nitrogen. A regulated solid-state 13.56 MHz radio frequency (RF) generator with a power amplifier was used to bias the substrate in order to control the energy of ions arriving onto the substrate. Self-bias was monitored during the deposition. The RF-generator features two alternative regimes of functioning, namely the stabilisation of RF forward power and the stabilization of self-bias on the substrate. In the first regime the amplitude of the RF signal is used for feedback control, whereas in the second regime the DC self-bias is used for feedback control.

A personal computer is the key device in the control system of the deposition machine. Two PCL-718 multi-function data acquisition cards³⁵, which were attached to the computer, carried out the control of the gas flows, providing a predetermined set of flow rates as a function of time. Each card is used in a differential unipolar analog input configuration and employs an industrial standard 12-bit successive approximation converter (HI-674A) to convert analog inputs. The maximum A/D sampling rate is 60 kHz, which is more than enough during control of the MFCs. Each card also has two 12-bit monolithic D/A output channels with an output range of 0 to +5 V for driving the MFC's up to full flow rate.

2.4 The deposition of SiO_x , SiN_x and SiO_xN_y

Silicon nitride and silicon oxynitride films have found many applications in integrated circuits and devices as dielectrics, diffusion barriers, isolation and passivation layers³⁶. It is also a very attractive material for optical thin films, since the refractive index can be varied according to needs over a wide range without evoking the problems associated with matching materials with different chemical and mechanical properties^{34,37-40}. Common methods to produce silicon nitride and oxynitride thin layers are 13.56 MHz PECVD, afterglow CVD or thermal CVD⁴¹.

One of the candidates to supplement the standard 13.56 MHz plasma deposition of thin films is a hybrid 2.45 GHz electron cyclotron resonance plasma enhanced chemical vapour deposition (ECR-PECVD) technology^{34,38,39}. In this arrangement, microwave excitation creates a low-energy, low-pressure and high-density plasma, while the 13.56 MHz bias allows for the precise control of the energy of charged particles striking the substrate surface and, therefore, for control over the stress in the films.

The properties of materials deposited by ECR-PECVD are process dependent. It consequently necessitates a broad characterization of the films in terms of growth rate, compositional and optical properties. In rest of this chapter we describe the sample preparation procedures, experimental conditions and growth of SiO_x , SiN_x and SiO_xN_y films of various composition. The growth rate, refractive index at 632.8 nm and infrared transmission characteristics are determined as functions of different process parameters. Complex refractive index of these materials will be discussed in detail in chapter 3.

2.4.1 Sample preparation and characterization

A set of experiments for the determination of the kinetics of the deposition of thin films and their optical properties was performed. In these experiments several types of substrates, namely sapphire, quartz, monocrystalline silicon and Corning 7059 glass, were used. Consequently, the preparation procedures were different for each type of substrate, as detailed below.

- A. Sapphire samples were cut out of 76 mm double-side polished substrates. They were sequentially cleaned prior to deposition in an ultrasonic bath of trichloroethylene, acetone and isopropanol for the removal of all organic contaminants, etched in a hot $\text{H}_3\text{PO}_4:\text{H}_2\text{SO}_4$ (1:3) mixture and rinsed in de-ionized water⁴². After these steps had been taken, samples were blown dry with nitrogen and immediately placed in the deposition chamber.
- B. Corning 7059 glass (25 × 25 mm) and quartz substrates were degreased in isopropanol in an ultrasonic bath and placed in a hot $\text{H}_2\text{O}_2:\text{H}_2\text{SO}_4$ (1:1) mixture for 1 minute, followed by a rinse in de-ionised water. Immediately after that, samples were dried with nitrogen and placed in the deposition chamber.
- C. High-resistivity double-side polished <111> silicon wafers (76 mm diameter) were quartered. One sample from each wafer was used as a reference in Fourier transform infrared (FTIR) spectroscopy measurements. The other three quarter pieces of each wafer were used as carriers for the deposition of layers

of different composition, but with the same thickness of approximately 120 nm.

Before deposition, all silicon substrates were cleaned according to the standard RCA cleaning procedure⁴³.

Samples were fixed to the substrate holder with clamps. Individual layers were grown to a thickness of approximately 1 μm for ultraviolet-visible-near-infrared (UV-VIS-NIR) transmission spectroscopy and to 120 nm for Fourier transform infrared spectroscopy (FTIR) and ellipsometric measurements. Deposited films were studied with a Rudolf Research Auto-EL IV ellipsometer at a single wavelength of 632.8 nm for an estimation of growth rate and the refractive indices of the films. A UV-VIS-NIR spectrophotometer Hitachi model U-3400 was used for the transmission measurements. Values of refractive index, extinction coefficient, absorption coefficient, thickness and optical band gap were calculated from these transmission spectra⁴⁴. Measurement technique and optical properties will be discussed in detail in chapter 3. Infrared transmission measurements were done over the 2.5 to 25 μm wavelength range, using a Perkin-Elmer 1600 FTIR spectrophotometer. Raman measurements were performed, using a DILOR confocal laser Raman spectrometer with a 100 mW, 514.5 nm INNOVA argon ion laser.

2.4.2 The deposition of SiO_x

During the deposition, the conditions were as follows: 100 Watt microwave power; base pressure less than 10^{-6} Torr; working pressure of about 2 mTorr; gas flow rates

set between 4 to 16 sccm; total flow rate kept constant at 20 sccm; 13.5 Watt RF bias power. Glass, silicon and sapphire substrates were cleaned prior to the deposition and fixed to the substrate holder. Individual layers were grown to a thickness of approximately 1 μm for UV-VIS-NIR transmission measurements and 120 nm for ellipsometric measurements. Gas flows for this set of experiments are given in Table 2.1.

No	30% SiH ₄ in Ar (sccm)	9% O ₂ in Ar (sccm)
1	20	0
2	18	2
3	16	4
4	14	6
5	13	7
6	12	8
7	11	9
8	8	12
9	4	16

Table 2.1: Gas flows for set of experiments on SiO_x growth

Figure 2.9 shows dependence of growth rate of SiO_x on gas flow ratio SiH₄/(SiH₄+O₂). The growth rate of SiO_x increases with an increase in the oxygen content in the gas phase from 43 Å/min at a SiH₄/(SiH₄+O₂) gas flow ratio of 1 up to a maximum of about 75 Å/min at a gas flow ratio of approximately 0.7.

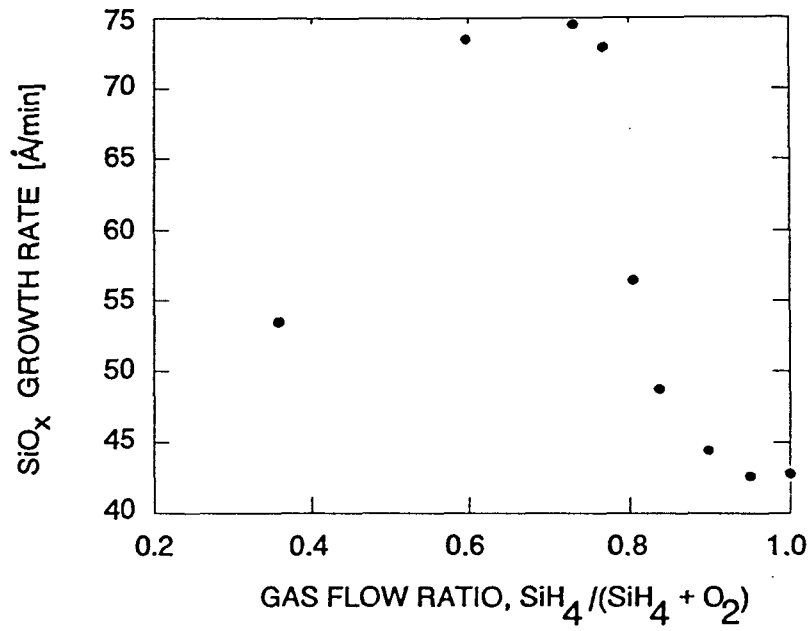


Figure 2.9: The growth rate of SiO_x as a function of gas flow ratio

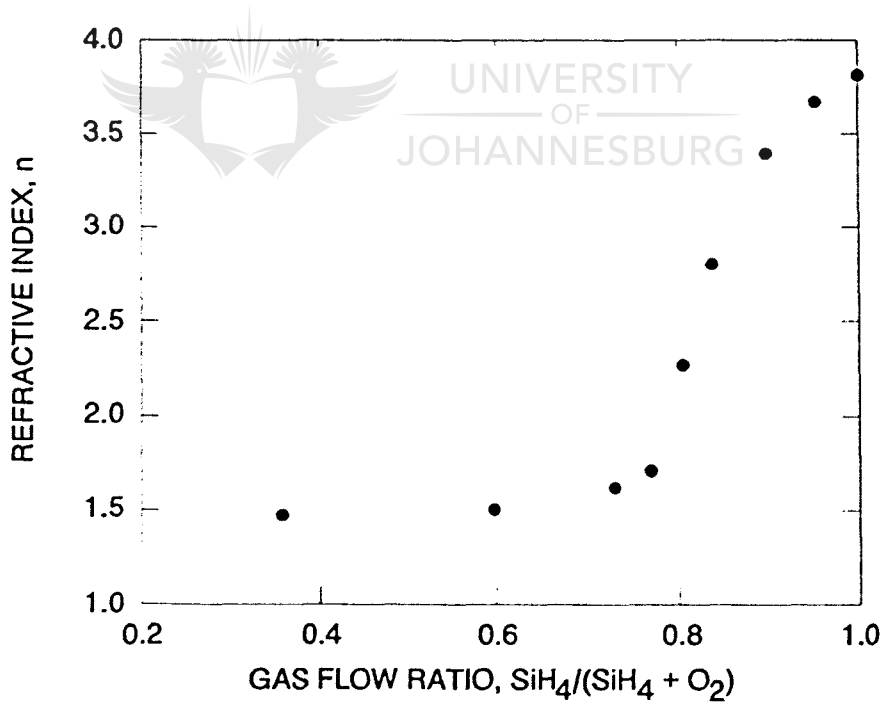


Figure 2.10: Refractive index of SiO_x (at 632.8 nm) as a function of gas flow ratio

With a further increase in oxygen content in the gas phase, the growth rate drops, owing to the depletion of the gas phase of silane.

Dependence of the refractive index (measured at 632.8 nm) on gas flow ratio is illustrated in Figure 2.10. Refractive index decreases from 3.8 for amorphous silicon to 1.48 for SiO₂ with decrease in gas flow ratio from 1 to 0.35. The biggest changes occur when the gas flow ratio changes between 1 and 0.78. The refractive index changes from 3.8 to 1.6 reflecting the change in composition from amorphous silicon to silicon dioxide.

2.4.3 The deposition of SiN_x

During the deposition the conditions were as follows: 100 Watt microwave power; base pressure less than 10⁻⁶ Torr; working pressure of about 2 mTorr; gas flow rates set between 4 to 16 sccm; total flow rate kept constant at 20 sccm; 13.5 Watt RF bias power. Glass, sapphire and silicon substrates were cleaned prior to the deposition and fixed to the substrate holder. Individual layers were grown to a thickness of approximately 1 μm for UV-VIS-NIR transmission measurements and 120 nm for ellipsometric measurements. Gas flows for this set of experiments are given in Table 2.2.

No	30% SiH ₄ in Ar (sccm)	N ₂ (sccm)
1	20.0	0.0
2	16.0	4.0
3	11.5	8.5
4	9.0	11.0
5	7.0	13.0
6	5.4	14.6
7	4.7	15.3
8	4.0	16.0

Table 2.2: Gas flows for set of experiments on SiN_x growth

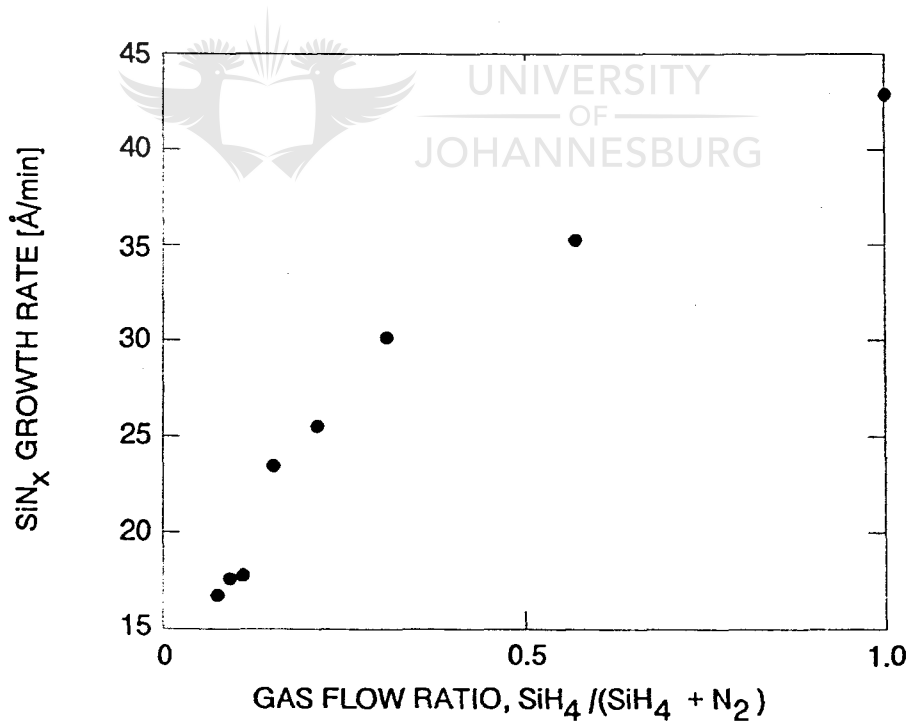


Figure 2.11: The growth rate of SiN_x as a function of gas flow ratio SiH₄/(SiH₄+N₂)

The growth rate of the SiN_x decreases with an increase in the nitrogen content in the gas phase from 43 Å/min at $\text{SiH}_4/(\text{SiH}_4+\text{N}_2)$ gas flow ratio equal to 1 down to about 17 Å/min at a gas flow ratio of approximately 0.07. Figure 2.11 shows a marked change in the deposition rate in the range of gas flow ratio between 0.1 and 0.3, where the composition of the film rapidly changes from silicon nitride to silicon. This change can be seen more clearly if the growth rate of SiN_x is shown versus N_2/SiH_4 gas flow ratio, as is illustrated in Figure 2.12.

Refractive index of SiN_x versus gas flow ratio $\text{SiH}_4/(\text{SiH}_4+\text{N}_2)$ is presented in Figure 2.13. Refractive index decreased strongly, from 3.8 for the film grown in an atmosphere of silane diluted with argon to 1.98 for the film grown at a gas flow ratio approximately equal to 0.07, with decreasing silane content in gas mixture. Note the change in the slope of the dependence of the refractive index on gas composition.

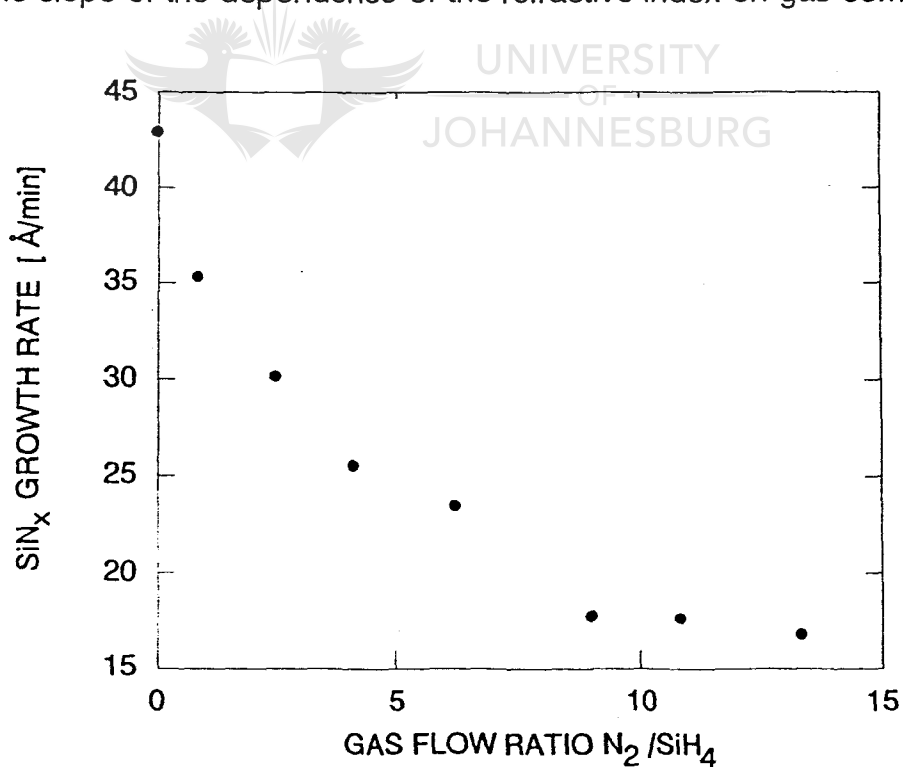


Figure 2.12: The growth rate of SiN_x as a function of a gas flow ratio N_2/SiH_4

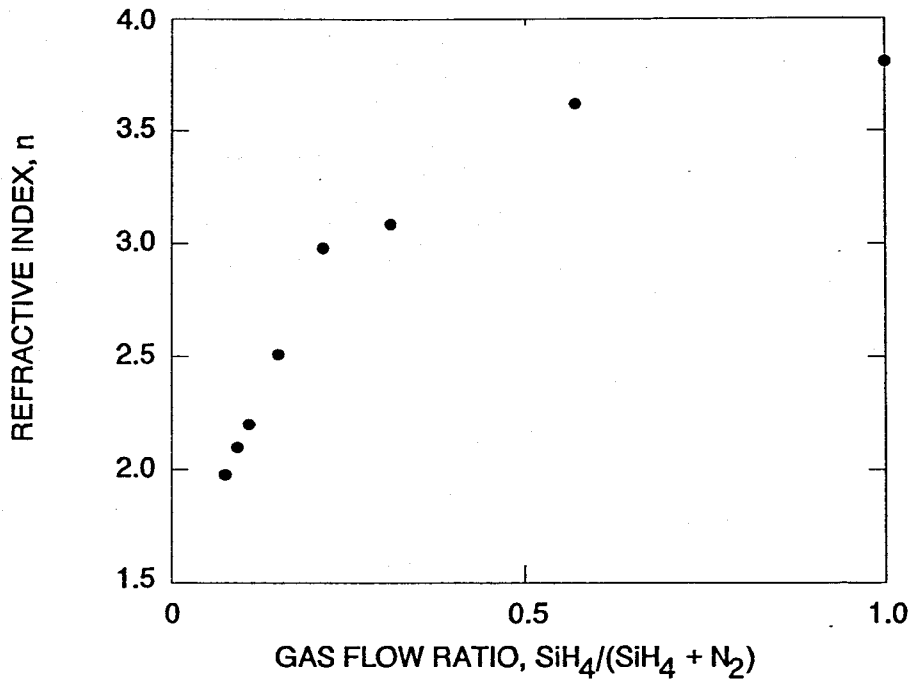


Figure 2.13: Refractive index of SiN_x (at 632.8) as a function of gas flow ratio

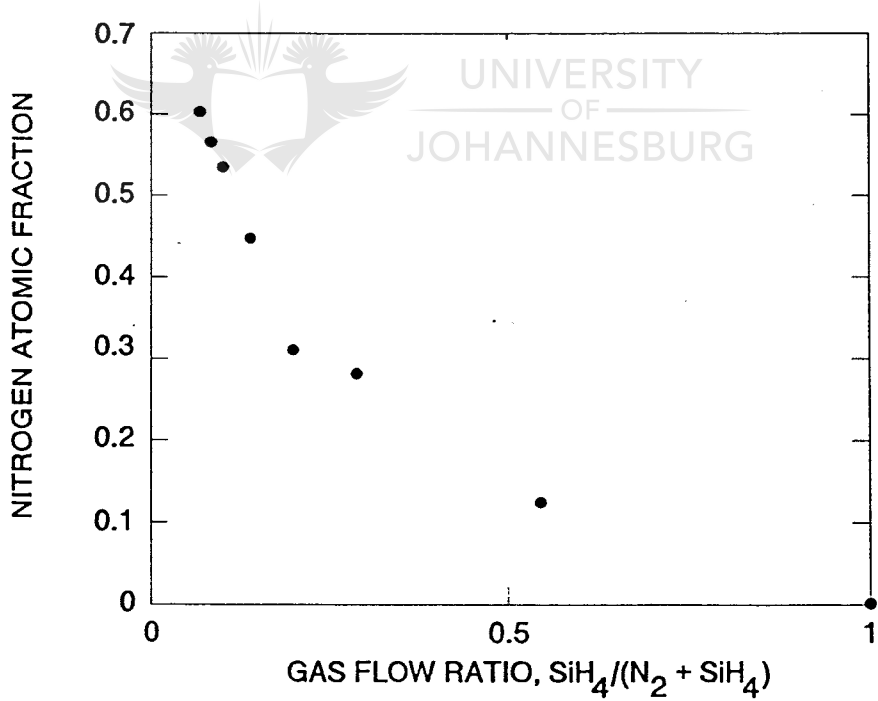


Figure 2.14: Nitrogen atomic fraction in SiN_x as calculated on the basis of data reported in the literature³⁷

Using the results of Donovan et al.³⁷, who calculated the refractive index dependence on the x composition in SiN_x according to the Lorentz-Lorenz equation, a relation between the approximate x composition of the grown films and gas flow ratio was established. The results are shown in Figure 2.14. One can note the marked change in the slope of the dependence at the gas flow ratio of approximately 0.21.

2.4.4 The deposition of SiO_xN_y

An in-depth study of the deposition of SiO_xN_y was undertaken specifically for use in optical coatings manufacturing. Deposition conditions were as follows: 100 Watt microwave power; base pressure less than 10^{-6} Torr; working pressure of about 2 mTorr; gas flow rates set between 1 to 16 sccm (lower limit set by control range of the mass flow controller); total flow rate kept constant at 21 sccm; RF bias power kept at 13.5 Watt. In addition to growth rate and refractive index dependence on gas composition, experiments were also performed to study the influence of RF-bias, extraction magnetic field and working pressure. For these sets of experiments, either total gas flow, or current through the magnetic coil were varied. When the effect of total flow was studied, the flow rates of N_2 , O_2 in Ar and SiH_4 in Ar were kept equal. The gas flow ratio of $\text{O}_2/(\text{O}_2+\text{N}_2)$ under these conditions was equal to 0.114. Corning 7059 glass, silicon and sapphire substrates were cleaned prior to the deposition and fixed to the substrate holder. Individual layers were grown to a thickness of approximately 1 μm for UV-VIS-NIR transmission measurements and 120 nm for ellipsometric measurements.

The "process trajectory" for this set of experiments is shown in Figure 2.15. Points on this graph correspond to the values of O_2/SiH_4 and N_2/SiH_4 flow ratios for which layers were grown. It has two regions, in one the flow of oxygen was kept constant at 1 sccm and the flows of silane and nitrogen were varied (points 1 to 4); in a second region, the flow of silane was kept constant at 7 sccm and the flows of nitrogen and oxygen were varied (points 4 to 10). Respective gas flows are given in Table 2.3. The values of the growth rates for points represented on the process trajectory are depicted in Figure 2.16.

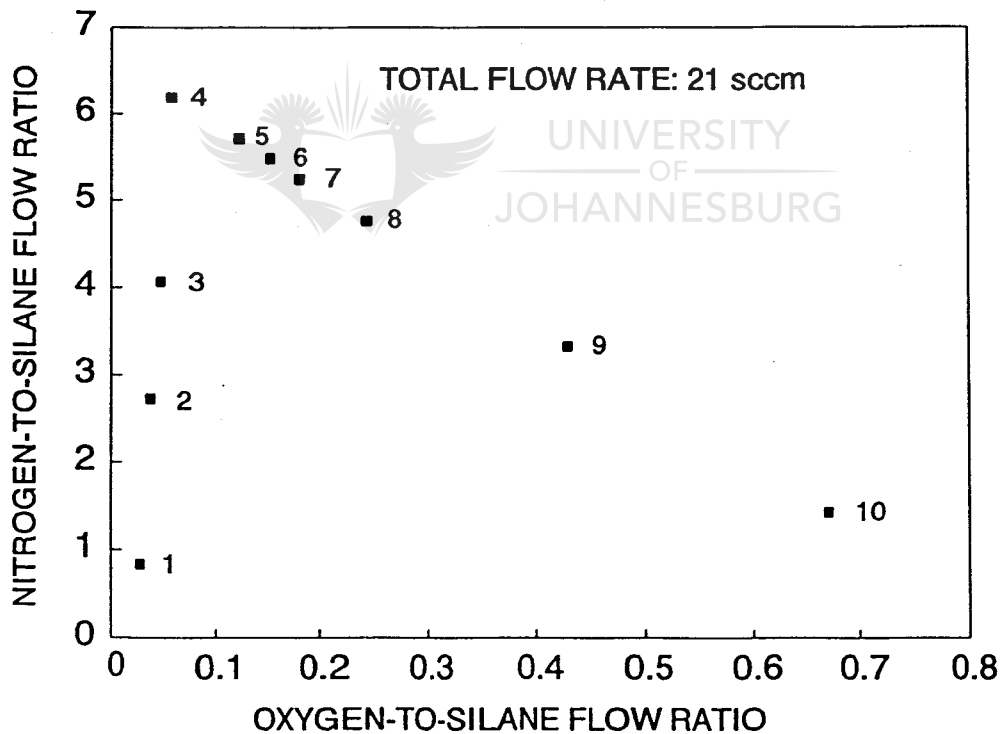


Figure 2.15: Process trajectory for the set of experiments on SiO_xN_y growth

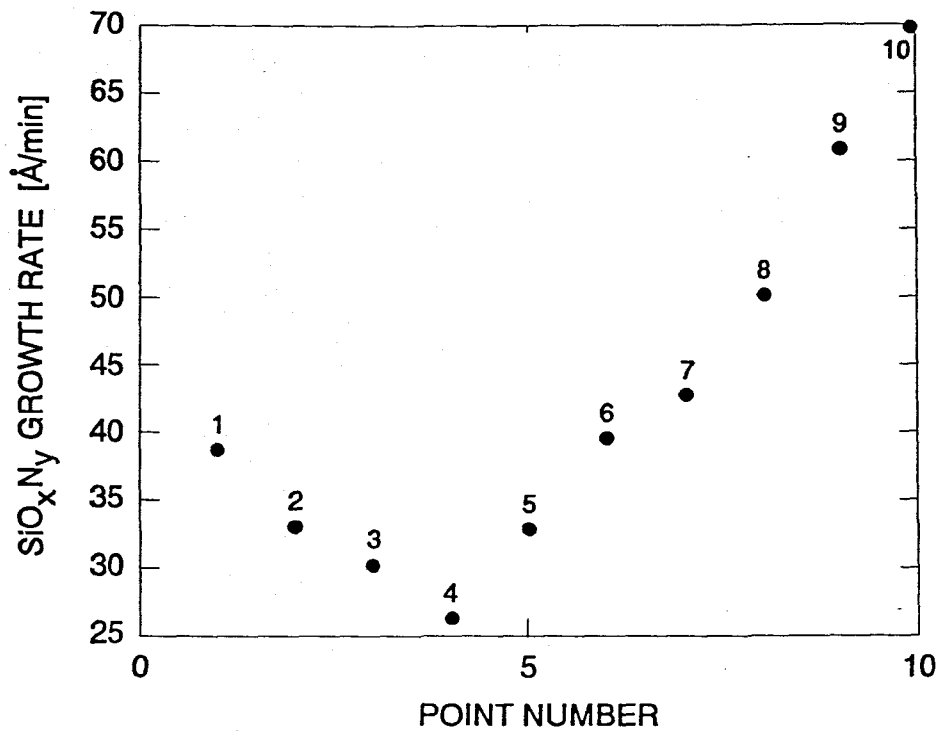


Figure 2.16: The growth rate of SiO_xN_y at corresponding points of process trajectory

Point number	30% SiH ₄ in Ar (sccm)	9% O ₂ in Ar (sccm)	N ₂ (sccm)
1	16	1	4
2	11	1	9
3	9	1	11
4	7	1	13
5	7	2	12
6	7	2.5	11.5
7	7	3	11
8	7	4	10
9	7	7	7
10	7	11	3

Table 2.3: Gas flows at the respective points of the "process trajectory"

In Figure 2.17 the dependence of the growth rate and the refractive index at 632.8 nm on self-bias is shown for a flow ratio of $O_2/(O_2+N_2)=0.114$. The growth rate increased linearly from 15 to 88 Å/min, while the refractive index increased only slightly from 1.522 to 1.552, most probably because of some densification resulting from an increase of ion bombardment due to the increase in self-bias from 50 to 250 Volt.

Data of the growth rate versus the gas flow ratio is shown in Figure 2.18. The growth rate increases with an increased $O_2/(N_2+O_2)$ ratio. Simultaneously, the refractive index, measured at a wavelength of 632.8 nm, is decreasing, because of the substitution of Si-N bonds with Si-O bonds and with oxidation of the excessive silicon in the layers.

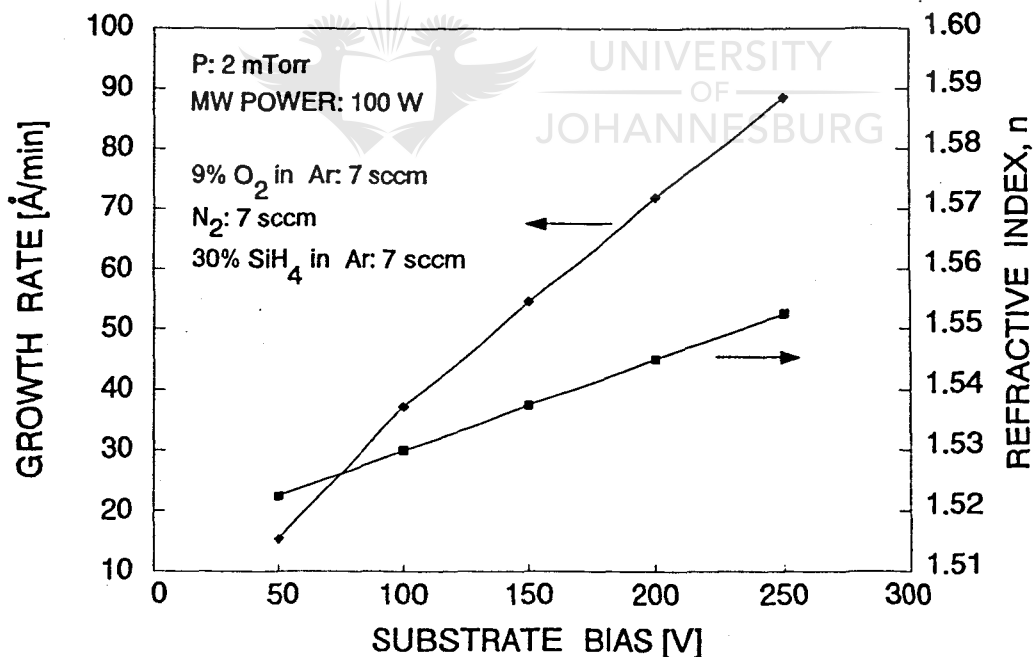


Figure 2.17: The influence of the bias on the growth rate and the refractive index of SiO_xN_y

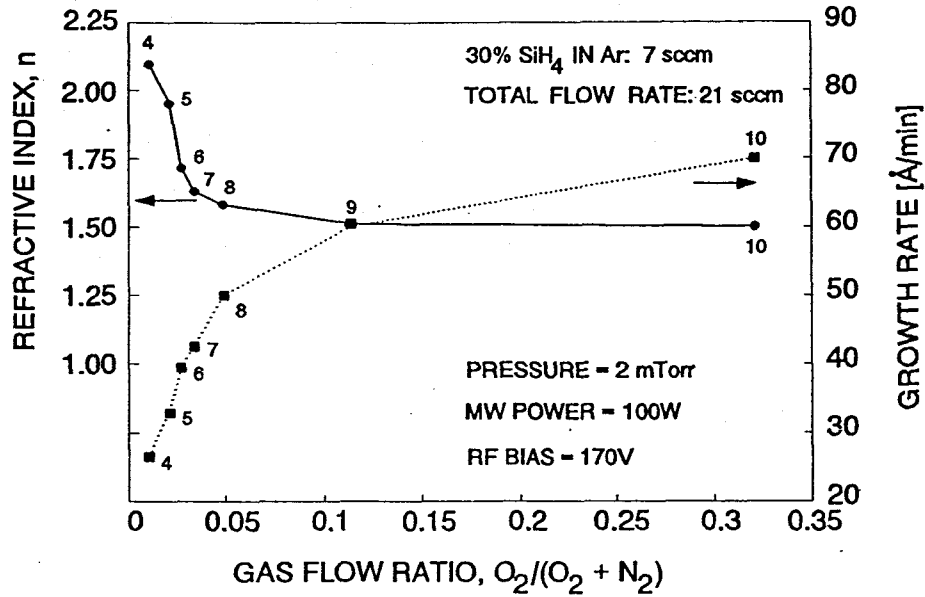


Figure 2.18: The dependence of growth rate and refractive index of SiO_xN_y on gas flow ratio

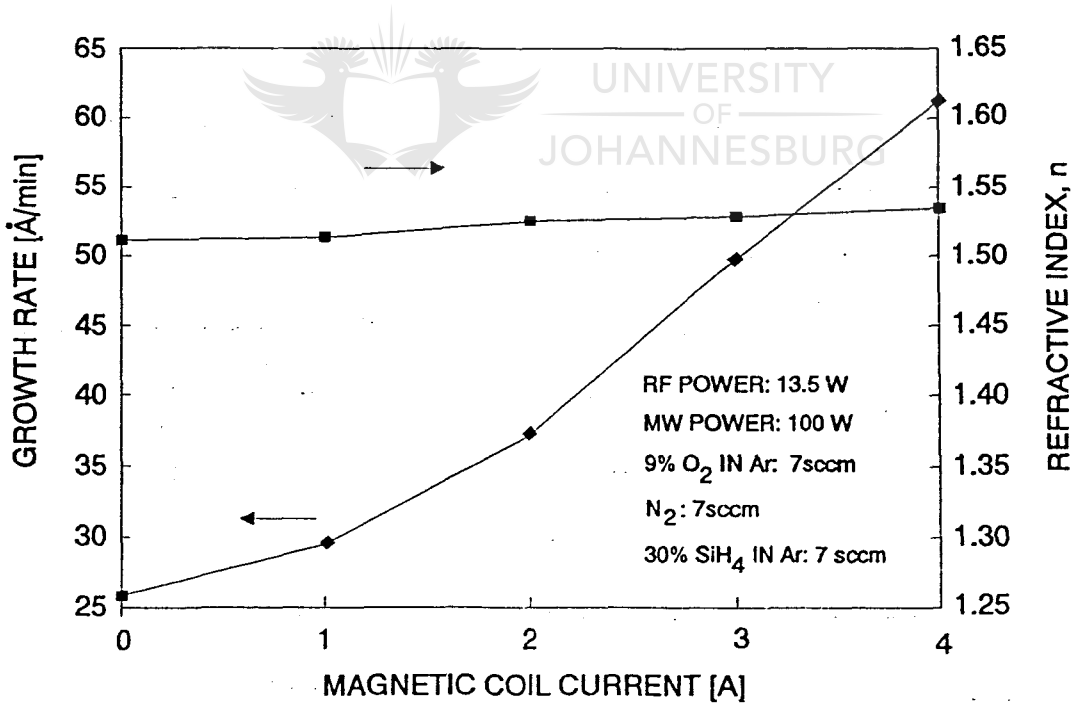


Figure 2.19: The dependence of the growth rate and the refractive index of SiO_xN_y on the current through magnetic coil

It was found that the extraction magnetic field only has a marginal influence on the refractive index measured at five points across the 50 mm diameter silicon wafer. As shown in Figure 2.19, the growth rate increased from 26 to 61 Å/min following an increase in current through the coil from 0 to 4 amperes (corresponding to an increase in the extraction magnetic field, measured in the plane of the coil, from 0 to 130 Gauss).

The value of total flow has a similar kind of influence on growth rate and refractive index. With an increase in total flow from 12 to 24 sccm (the pressure in the chamber increased from 1.5 to 3.0 mTorr), the average refractive index measured at five points across the 50 mm silicon wafer, decreased from 1.554 to 1.535, whereas the growth rate increased from 40 to 68 Å/min. Dependence of the growth rate and the refractive index on the total flow is given in Figure 2.20.

Results of FTIR measurements are presented in Figure 2.21. A clear tendency can be observed in the changing of optical absorption peak positions. With an increase in the $O_2/(O_2+N_2)$ gas flow ratio, the main peak of the Si-N stretching mode⁴⁵ in Si_3N_4 at 830 cm^{-1} is smoothly decreasing in amplitude, while the peak at 1070 cm^{-1} , which is the main Si-O stretching mode³¹ in SiO_2 , is gradually increasing. One should notice that the transition from mostly silicon nitride to mostly silicon dioxide takes place between the 0.027 and 0.049 gas flow ratios. The corresponding change in the refractive index can be seen in Figure 2.18. In addition, there is hardly any Si-H or N-H bonds⁴⁵ at wave numbers 2160 cm^{-1} and 3330 cm^{-1} , respectively. The exception is the samples grown at 0.01 and 0.021 gas flow ratios, for which the small number of Si-H bonds is attributed to the excessive silicon in the layers⁴⁵.

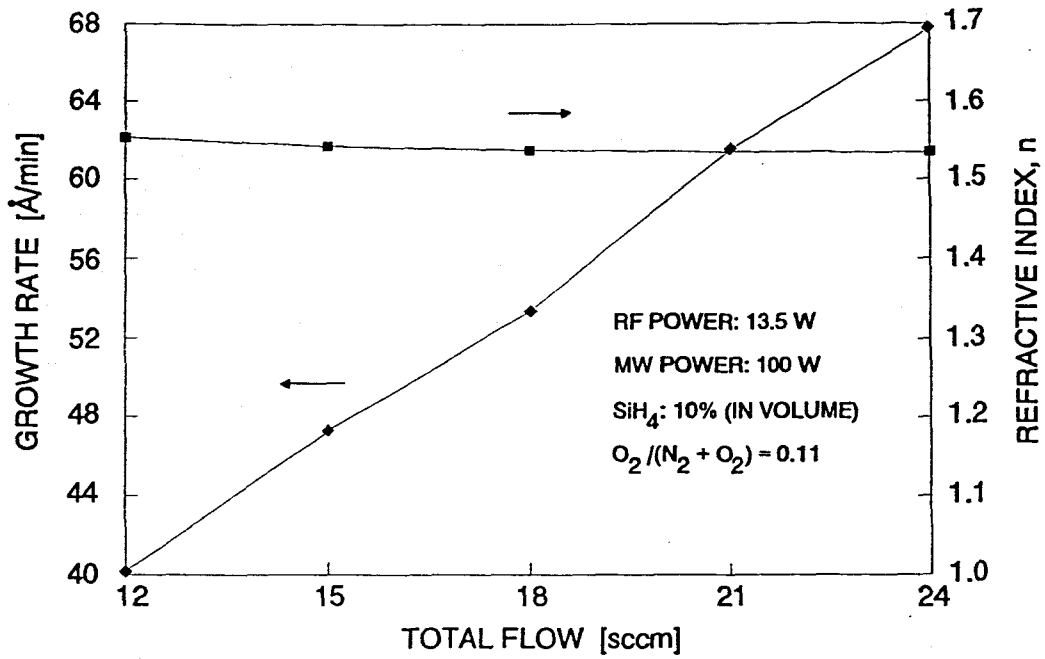


Figure 2.20: The dependence of the growth rate and the refractive index on total gas flow at constant gas flow ratios

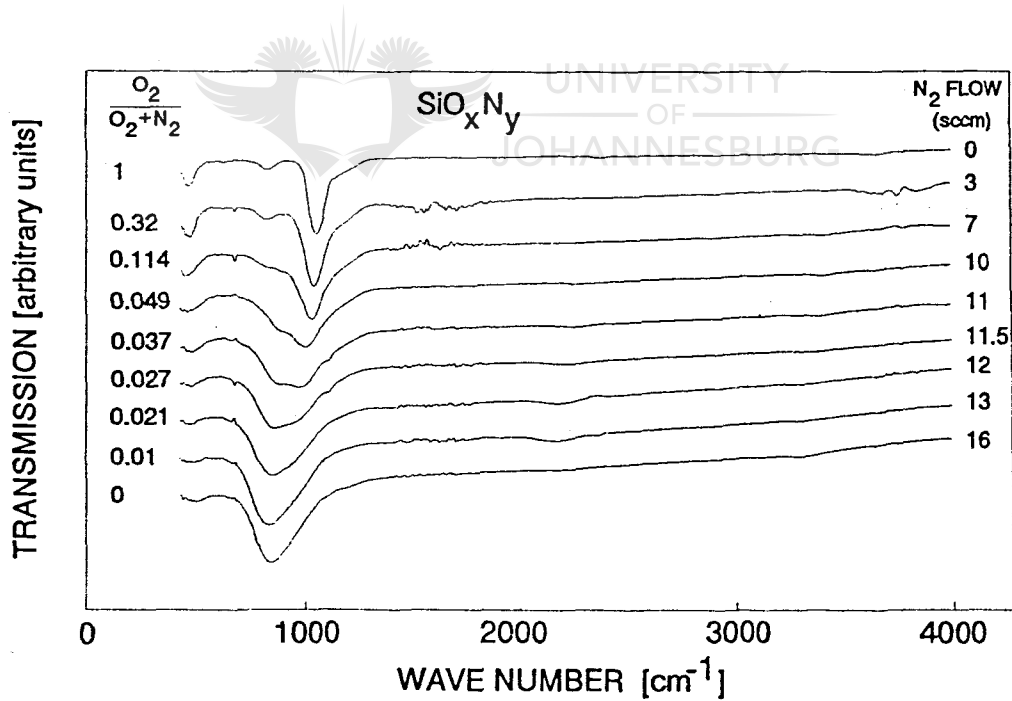


Figure 2.21: FTIR transmission spectra of SiO_xN_y grown at different gas flow ratios

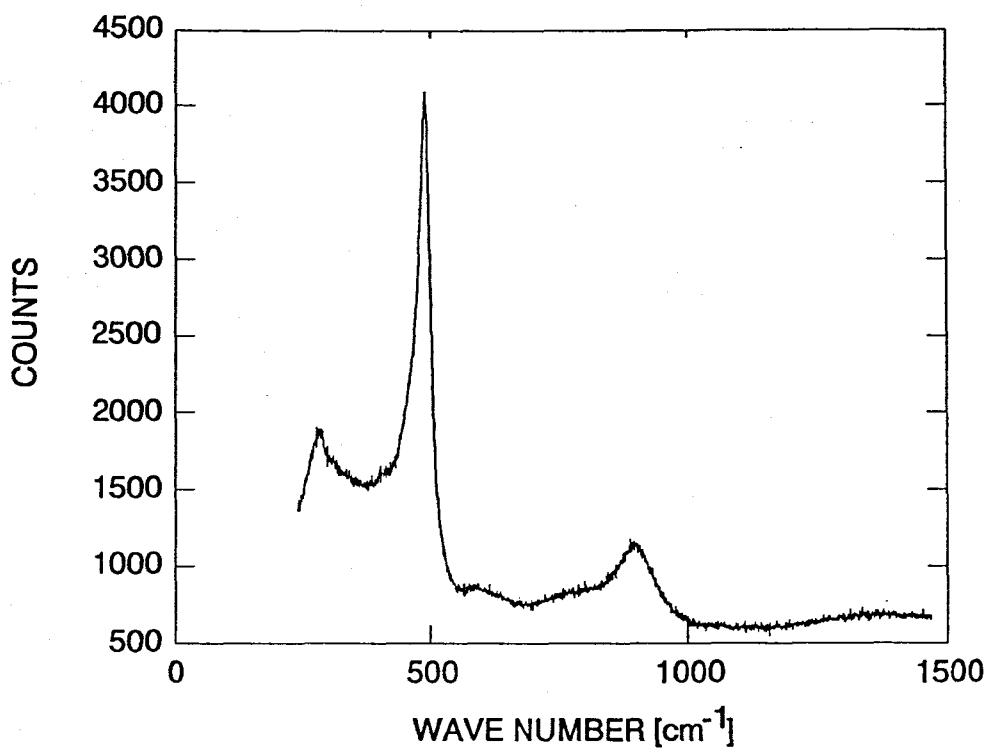


Figure 2.22: Raman spectrum of a-Si:H grown in SiH₄/Ar atmosphere

Film structure was evaluated by Raman spectroscopy. The investigation revealed that no microcrystalline (μc) or polycrystalline silicon phases were present, based on the absence of a Raman peak near 520 cm^{-1} . Only the main amorphous silicon peak positioned at approximately 486 cm^{-1} was detected^{46,47}. The Raman spectrum of a sample grown in silane diluted with argon (30% SiH₄ in Ar) at a pressure of approximately 2 mTorr is shown in Figure 2.22.

2.5 Conclusions

Electron cyclotron resonance plasma enhanced chemical vapour deposition (ECR-PECVD) was used for the growth of SiO_x , SiN_x and SiO_xN_y films from O_2/Ar , N_2 and SiH_4/Ar mixtures.

Studies of deposition in Si-SiO_2 and $\text{Si-Si}_3\text{N}_4$ systems showed a marked difference in growth rate behaviour. In SiN_x deposition, the growth rate decreased monotonically with an increase of nitrogen flow (at constant total flow) from 43 to 17 Å/min, whereas SiO_x growth rate has a maximum of 75 Å/min at the $\text{SiH}_4/(\text{O}_2 + \text{SiH}_4)$ gas flow ratio of approximately 0.7.

The refractive index measured at 632.8 nm for both materials decreased strongly with a decrease of the silane content in the gas phase. Values ranged from 3.8 for amorphous silicon down to 1.98 and 1.48 for silicon nitride and silicon dioxide, respectively. The thin film microstructure was evaluated by Raman spectroscopy and found to be amorphous.

The ECR-PECVD of silicon oxynitride layers was investigated for different gas flow ratios and substrate bias. It was found that an increased self-bias, total flow and extraction magnetic field resulted in a large increase of the growth rate, whilst the refractive index changed only slightly. The gas flow ratio determined refractive index over a wide range as a result of changes in the chemical composition. FTIR measurements showed a smooth transition between silicon dioxide and silicon nitride.

REFERENCES FOR CHAPTER 2

1. O.A. Popov and H. Waldron, "Electron cyclotron resonance plasma stream source for plasma enhanced chemical vapor deposition", *Journal of Vacuum Science and Technology A*, Vol. 7, No. 3, 1989, pp. 914-917.
2. R.P. Vaudo, J.W. Cook, Jr. and J.F. Schetzina, "Atomic nitrogen production in a molecular-beam epitaxy compatible electron cyclotron resonance plasma source", *Journal of Vacuum Science and Technology B*, Vol. 12, No. 2, 1994, pp. 1232-1235.
3. Y. Z. Hu, M. Li, Y. Wang and A.E. Irene, "Electron cyclotron resonance plasma process for InP passivation", *Applied Physics Letters*, Vol. 63, No. 8, 1993, pp. 1113-1115.
4. H. Yamada, "Low-temperature surface cleaning method using low energy reactive ionized species", *Journal of Applied Physics*, Vol. 65, No. 2, 1989, pp. 775-781.
5. J. Asmussen, "Electron cyclotron resonance plasma microwave discharges for etching and thin-film deposition", *Journal of Vacuum Science and Technology A*, Vol. 7, No. 3, 1989, pp. 883-893.
6. N. Blayo, I. Tepermeister, J.L. Benton, G.S. Higashi, T. Boone, A. Onuoha, F.P. Klemens, D.I. Ibbotson, J.T.C. Lee and H.H. Sawin, "Comparison of advanced plasma sources for etching applications. IV. Plasma induced damage in helicon and multipole electron cyclotron resonance source", *Journal of Vacuum Science and Technology B*, Vol. 12, No. 3, 1994, pp. 1340-1350.

7. F.F. Chen, "Experiments on helicon plasma sources", *Journal of Vacuum Science and Technology A*, Vol. 10, No. 4, 1992, pp. 1389-1401.
8. M.C. Vella, "Candidates for advanced processing technology at the Lawrence Berkeley Laboratory", *Solid State Technology*, No. 9, 1990, pp. 95-99.
9. J.B. Carter, J.P. Holland, E. Peltzer, B. Richardson, E. Bogle, H.T. Nguyen, Y. Melaku, D. Gates and M. Ben-Dor, "Transformer coupled plasma etch technology for the fabrication of subhalf micron structures", *Journal of Vacuum Science and Technology A*, Vol. 11, No. 4, 1993, pp. 1301-1306.
10. F.F. Chen, *Introduction to Plasma Physics and Controlled Fusion*, Plenum Press, New York, 1984.
11. J.L. Cecchi, *Introduction to plasma concepts and discharge configurations*, Chapter 2, in Handbook of Plasma Processing Technology: Fundamentals, etching, deposition, and surface interactions, (Eds: S.M. Rossnagel, J.J. Cuomo and W.D. Westwood), Noyes Publications, Park Ridge, 1989, pp. 14-69.
12. B. Chapman, *Glow discharge processes. Sputtering and plasma etching*, John Wiley & Sons, New York, 1980.
13. D.B. Graves, "Plasma processing", *IEEE Transactions on Plasma Science*, Vol. 22, No. 1, 1994, pp. 31-42.
14. C. Pomot and J. Pelletier, *High frequency sustained multipolar plasmas*, Chapter 13, in Plasma Technology 4, Microwave excited plasmas (Eds.: M. Moisan and J. Pelletier), Elsevier, Amsterdam, 1992, pp. 385-418.
15. J. Perrin, "Plasma and surface reactions during a-Si:H film growth", *Journal of Non-Crystalline Solids*, Vol. 137&138, 1991, pp. 639-644.

16. R. Reif, Plasma enhanced chemical vapor deposition of thin films for microelectronics, Chapter 10, in Handbook of Plasma Processing Technology: Fundamentals, etching, deposition, and surface interactions (Eds: S.M. Rossnagel, J.J. Cuomo and W.D. Westwood), Noyes Publications, Park Ridge, 1989, pp. 260-284.
17. D.B. Graves and R.A. Gottscho, "Computer applications in plasma materials processing", MRS Bulletin, Vol. 16, No. 2, 1991, pp. 16-22.
18. R.F. Bunshah, "Critical issues in plasma-assisted vapor deposition processes", IEEE Transactions on Plasma Science, Vol. 18, No. 6, 1990, pp. 846-854.
19. G.G. Lister, "Low-pressure gas discharge modelling", Journal of Physics D: Applied Physics, Vol. 25, No. 12, 1992, pp. 1649-1680.
20. S.T. Picraux, E. Chason and T.M. Mayer, "Ion-assisted surface processing of electronic materials", MRS Bulletin, Vol. 17, No. 6, 1992, pp. 52-57.
21. R. Messier, J.E. Yehoda and L.J. Piliore, Ion-surface interactions: general understanding, Chapter 19, in Handbook of Plasma Processing Technology: Fundamentals, etching, deposition, and surface interactions (Eds: S.M. Rossnagel, J.J. Cuomo and W.D. Westwood), Noyes Publications, Park Ridge, 1989, pp. 448-465.
22. P. Martin, "Ionization-assisted evaporative processes: techniques and film properties", IEEE Transactions on Plasma Science, Vol. 18, No. 6, 1990, pp. 855-868.
23. H.P.W. Hey B.G. Sluijck and D.G. Hemmes, "Ion bombardment: a determining factor in plasma CVD", Solid State Technology, No. 4, 1990, pp. 139-144.

24. J.M.E. Harper, "Ion beam techniques in thin film deposition", *Solid State Technology*, No. 4, 1987, pp. 129-134.
25. J.E. Greene, "Low energy ion bombardment during film deposition from the vapor phase: effects on microstructure and microchemistry", *Solid State Technology*, No. 4, 1987, pp. 115-122.
26. J.R. McNeil, A.C. Barron, S.R. Wilson and W.C. Herrmann, Jr., "Ion-assisted deposition of optical thin films: low energy vs high energy bombardment", *Applied Optics*, Vol. 23, No. 4, 1984, pp. 552-559.
27. O.A. Popov, S.Y. Shapoval, M.D. Yoder and A.A. Chumakov, "Electron cyclotron resonance plasma source for metalorganic chemical vapor deposition of silicon oxide films", *Journal of Vacuum Science and Technology A*, Vol. 12, No. 2, 1994, pp. 300-307.
28. S.Yu. Shapoval, P.V. Bulkin, A.A. Chumakov, S.A. Khudobin, I.A. Maximov and G.M. Mikhailov. "Compact ECR source of ions and radicals for semiconductor surface treatment", *Vacuum*, Vol. 43, No. 3, 1992, pp. 195-197.
29. P. Mak, G. King, T.A. Grotjohn and J. Asmussen, "Investigation of the influence of electromagnetic excitation on electron cyclotron resonance discharge properties", *Journal of Vacuum Science and Technology A*, Vol. 10, No. 4, 1992, pp. 1281-1287.
30. M. Azuma, T. Yokoi, I. Shiiya and I. Shimizu, "Stable a-Si:H fabrication from halogenous silane by ECR hydrogen plasma", *Journal of Non-Crystalline Solids*, Vol. 164&166, 1993, pp. 47-50.

31. K.A. Buckle, K. Pastor, C. Constantine and D. Johnson, "Parametric evaluation of electron cyclotron resonance deposited SiO₂ using a multicusp plasma applicator", *Journal of Vacuum Science and Technology B*, Vol. 10, No. 3, 1992, pp. 1133-1138.
32. R.R. Burke, J. Pelletier, C. Pomot and L. Vallier, "Distributed electron cyclotron resonance in silicon processing: epitaxy end etching", *Journal of Vacuum Science and Technology A*, Vol. 8, No. 3, 1990, pp. 2931-2938.
33. P. O'Keeffe, S. Komuro, S. Den, T. Morikawa and Y. Aoyagi, "Development and applications of a compact electron cyclotron resonance source", *Japanese Journal of Applied Physics*, Vol. 30, No. 11B, 1991, pp. 3164 - 3168.
34. P.V. Bulkin, P.L. Swart and B.M. Lacquet, "Effect of process parameters on the properties of electron cyclotron resonance plasma deposited silicon-oxynitride", accepted for publication in *Journal of Non-Crystalline Solids*.
35. Model PCL-718, User's Manual, Advantech Co., Ltd, Taiwan, 1988.
36. B. Gorowitz, R.H. Wilson and T.B. Gorczyca, "Recent trends in LPCVD and PECVD", *Solid State Technology*, No. 10, 1987, pp. 97-103.
37. E.P. Donovan, D. Van Vechten, A.D.F. Kahn, C.A. Carosella and G.K. Hubler, "Near infrared rugate filter fabrication by ion beam assisted deposition of Si_(1-x)N_x films", *Applied Optics*, Vol. 28, No. 14, 1989, pp. 2940-2944.
38. P.V. Bulkin, P.L. Swart, B.M. Lacquet and F.J. Burger, "Electron cyclotron resonance plasma deposition for multilayer structures of silicon nitride on silicon", *South African Journal of Physics*, Vol. 16, No. 1&2, 1993, pp. 33-36.

39. S. Dzioba and R. Rousina, "Dielectric thin film deposition by electron cyclotron resonance plasma chemical vapor deposition for optoelectronics", *Journal of Vacuum Science and Technology B*, Vol. 12, No. 1, 1994, pp. 433-440.
40. S. Lim, J.H. Ryu, J.F. Wager and L.M. Casas, "Inhomogeneous dielectrics grown by plasma-enhanced chemical vapor deposition", *Thin Solid Films*, Vol. 236, No. 1&2, 1993, pp. 64-66.
41. P.H. Singer, "Depositing high quality dielectrics", *Semiconductor International*, No. 7, 1989, pp. 48-51.
42. T.D. Moustakas, T. Lei and R.J. Molnar, "Growth of GaN by ECR-assisted MBE", *Physica B*, Vol. 185, No.1-4, 1993, pp. 36-49.
43. W. Kern and D.A. Puotinen, "Cleaning solutions based on hydrogen peroxide for use in silicon semiconductor technology", *RCA Review*, Vol. 31, No. 6, 1970, pp. 187-206.
44. R. Swanepoel, "Determination of the thickness and optical constants of amorphous silicon", *Journal of Physics E: Scientific Instrumentation*, Vol. 16, No. 12, 1983, pp. 1214-1222.
45. D. Schalach, A. Scharmann and R. Wolfrat, "The role of hydrogen in silicon nitride and silicon oxynitride films", *Thin Solid Films*, Vol. 124, 1985, pp. 301-308.
46. R.D. Knox, V. Dalal, B. Moradi and G. Chumanov, "Amorphous and polycrystalline silicon films deposited by electron cyclotron resonance reactive plasma deposition", *Journal of Vacuum Science and Technology A*, Vol. 11, No. 4, 1993, pp. 1896-1900.

47. Y. He, C. Yin, G. Cheng, L. Wang, X. Liu and G.Y. Hu, "The structure and properties of nanosize crystalline silicon films", Journal of Applied Physics, Vol. 75, No. 2, 1994, pp. 797-803.



CHAPTER 3


THE OPTICAL PROPERTIES OF ECR-DEPOSITED FILMS OF SiO_xN_y

3.1 Introduction

The design and manufacture of thin film optical filters demand a thorough knowledge of the optical parameters of the films over a wide wavelength range. In the case of homogeneous refractive index layers, which are used in, for example, multilayer quarterwave stacks, tables containing optical data for a large number of materials are readily available¹⁻³. For advanced rugate-type filters and optical coatings in general, continuously varying refractive index profiles are often required. The optical properties of such layers are always process dependent and often not well characterized. Hence, detailed information regarding the optical properties of the materials to be used and the dependencies of optical properties on different process conditions will be required for the design and fabrication of optical coatings possessing inhomogeneous refractive index layers. Consequently, comprehensive optical characterization is an essential step in the development of the technology.

Among the materials that can be used for UV-visible and infrared filters, is SiO_xN_y , where x and y are varied according to a chosen design. Thin film SiO_xN_y has an amorphous structure and constitutes a continuous series of solid solutions, thus ensuring the thermal and chemical stability of the inhomogeneous film. The large excursion of refractive index achievable, ranging between 1.46 of SiO_2 and 3.8 of amorphous silicon (at 632.8 nm), is very important for the optical filter design. Between stoichiometric SiO_2 and Si_3N_4 , this material has very low absorption losses and can be used even for mirrors for high-power lasers. The optical properties of such material can be tailored by controlling the process variables. In this chapter, we will discuss the main optical properties of SiO_xN_y layers deposited by ECR-PECVD, as well as the characterization technique used to extract these properties.

3.2 The properties of optical materials



When light interacts with a dielectric (or semiconductor) film it is first partially reflected at the surface and then scattered and absorbed in various processes. The rest of the light is transmitted, after being again partially reflected at the second interface. The interaction of electromagnetic radiation with media is governed by Maxwell's equations⁴. Let us consider the material as a continuum, which is described by four parameters: magnetic permeability μ , dielectric permittivity ϵ , space charge density ρ and electric conductivity σ . With these parameters Maxwell's equations for isotropic media, which are the only media that will be considered here, can be written as follows⁴:

$$\text{curl} \mathbf{H} = \mathbf{j} + \partial \mathbf{D} / \partial t \quad (3.1)$$

$$\text{curl} \mathbf{E} = -\partial \mathbf{B} / \partial t \quad (3.2)$$

$$\nabla \mathbf{D} = \rho \quad (3.3)$$

$$\nabla \mathbf{B} = 0 \quad (3.4)$$

Here \mathbf{H} = magnetic field vector,
 \mathbf{E} = electric field vector,
 \mathbf{B} = magnetic induction,
 \mathbf{D} = electric displacement and
 \mathbf{j} = the current density.

To Equations (3.1)-(3.4) we should add



UNIVERSITY
OF
JOHANNESBURG

$$\mathbf{j} = \sigma \mathbf{E} \quad (3.5)$$

$$\mathbf{D} = \epsilon \mathbf{E} \quad (3.6)$$

$$\mathbf{B} = \mu \mathbf{H} \quad (3.7)$$

and

$$\varepsilon = \varepsilon_r \varepsilon_0 \quad (3.8)$$

$$\mu = \mu_r \mu_0 \quad (3.9)$$

$$\varepsilon_0 = 1/\mu_0 c^2 \quad (3.10)$$

where ε_0 = permittivity of free space,
 μ_0 = permeability of free space,
 ε_r = relative permittivity of the material,
 μ_r = relative permeability of the material,
 c = velocity of light in free space.

If there is no space charge in the medium ($\rho = 0$), Equation (3.3) becomes

$$\nabla \mathbf{D} = 0 \quad (3.11)$$

From Equations (3.1) and (3.2) follows for \mathbf{E}

$$\nabla^2 \mathbf{E} = \varepsilon \mu \frac{\partial^2 \mathbf{E}}{\partial t^2} + \mu \sigma \frac{\partial \mathbf{E}}{\partial t} \quad (3.12)$$

A similar expression can be obtained for \mathbf{H} .

The solution of Equation (3.12) may be found in the complex form of a plane-polarised wave propagating with velocity v along the x axis:

$$E = \mathcal{E} \exp [i\omega(t-x/v)] \quad (3.13)$$

where $\mathcal{E} =$ the complex electric field vector and
 $\omega =$ the angular frequency of the wave.

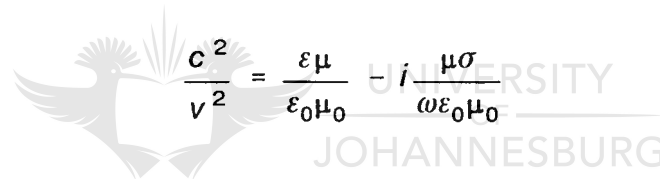
Equation (3.13) will be a solution of Equation (3.12) only if

$$\omega^2/v^2 = \omega^2\varepsilon\mu - i\omega\mu\sigma \quad (3.14)$$

For vacuum $\sigma = 0$ and $v = c$, thus, from Equation (3.14), we have

$$c^2 = 1/\mu_0\varepsilon_0 \quad (3.15)$$

Equation (3.15) is identical to Equation (3.10). If we multiply Equation (3.14) by Equation (3.10) and divide by ω^2 , we obtain the following:



$$\frac{c^2}{v^2} = \frac{\varepsilon\mu}{\varepsilon_0\mu_0} - j \frac{\mu\sigma}{\omega\varepsilon_0\mu_0} \quad (3.16)$$

where c/v is a dimensionless parameter of the medium called complex index of refraction, which we denote by N :

$$N^2 = \varepsilon_r\mu_r - i\mu_r\sigma/\omega\varepsilon_0 \quad (3.17)$$

Equation (3.17) suggests that N is of the form

$$N = c/v = n - ik \quad (3.18)$$

Two possible values of N can be obtained from Equation (3.17). Because of physical reasons, the one should be taken that gives a positive value of n . Parameter n is known as the "real part of the refractive index" or is often simply referred to as the "refractive index", because N is real in an ideal dielectric material. Parameter k is known as the "extinction coefficient". These two parameters are recognised as the main intrinsic optical properties of a material.

For non-magnetic material $\mu_r = 1$, thus from Equations (3.17) and (3.18),

$$n^2 - k^2 = \epsilon_r \mu_r = \epsilon_r \quad (3.19)$$

and

$$2nk = \frac{\sigma \mu_r}{\omega \epsilon_0} = \frac{\sigma}{\omega \epsilon_0} \quad (3.20)$$

Introducing the wavelength in free space, $\lambda = 2\pi c/\omega$, we can now re-write Equation (3.13) as follows

$$E = \mathcal{E} \exp\left(i \left[\omega t - \frac{2\pi N}{\lambda} x \right]\right) \quad (3.21)$$

Substitution of $n - ik$ for N in Equation (3.21) gives:

$$E = \mathcal{E} \exp\left[-\frac{2\pi k}{\lambda} x\right] \exp\left(i \left[\omega t - \frac{2\pi n}{\lambda} x \right]\right) \quad (3.22)$$

k can be considered as a measure of the absorption in the material: the distance $\lambda/2\pi k$ is the distance in which the amplitude of the wave falls to 0.37 (one divided by base of natural logarithms) of its initial value.

The intrinsic optical properties of a material are functions of wavelength. In a particular compound materials system such as Si-O-N, these properties can be changed by varying the stoichiometry through the process parameters. However, the value of refractive index, its wavelength dependence (dispersion), and absorption (e.g. band-to-band and intra-band transitions) are interdependent. Consequently, it is inevitable that a large range of refractive index with low dispersion and low losses is only available in the infrared. In real material systems, the designer should also be aware of additional loss mechanisms caused by structural defects and impurities introduced by the manufacturing technology.



Thus, the choice of the materials and technology for the manufacturing of optical coatings will depend largely on intrinsic optical properties of materials and ability of the fabrication process to provide low defects, low impurity films, yielding as low absorption losses as possible in the spectral range of interest. Consequently, the rest of this chapter will be dedicated to the discussion of the characterization technique and optical properties of thin films of SiO_x , SiN_x and SiO_xN_y grown by electron cyclotron resonance plasma enhanced chemical vapour deposition (ECR-PECVD).

3.3 The optical transmission spectroscopy

Frequently, for non-destructive determination of thickness and refractive index of transparent thin films, ellipsometry is used. However, ellipsometry cannot give the information over a wide range of wavelengths (unless spectroscopic ellipsometry is available⁶). Optical transmission spectroscopy is a powerful tool for non-destructive characterization of thin films⁷. We shall present a detailed discussion of the technique developed by Swanepoel⁷⁻⁹, since it became a standard for the extraction of optical properties from transmission spectra of thin films deposited onto transparent substrates and this technique was used extensively throughout this work.

The system of a thin film on a transparent substrate is shown in Figure 3.1. The thin film has a thickness d and a complex refractive index $N=n-ik$. k can also be expressed in terms of the absorption coefficient α .

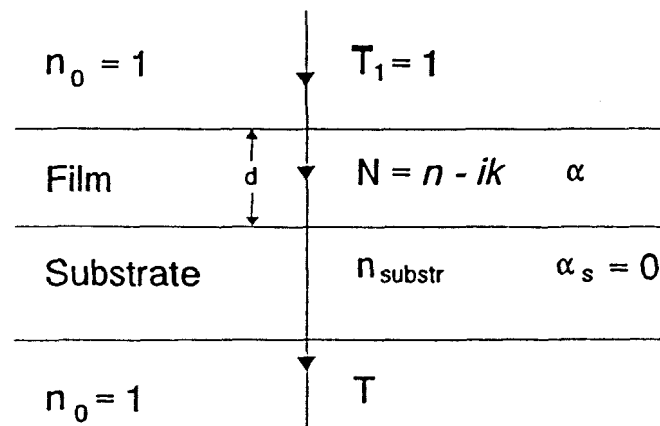


Figure 3.1: The system of an absorbing film on a transparent substrate

The transparent substrate has a thickness several orders of magnitude larger than d and has an index of refraction n_{substr} and an absorption coefficient $\alpha_s = 0$. The refractive index of the surrounding air is $n_o = 1$. Multiple reflections at all interfaces should be taken into account when calculating transmittance, T .

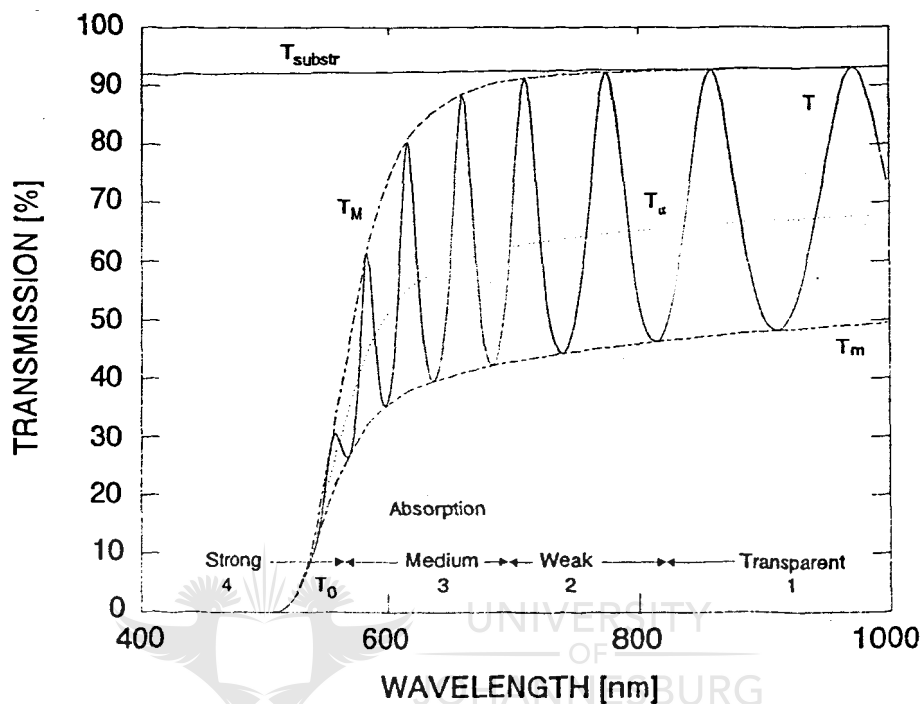


Figure 3.2: A typical transmission curve of an absorbing film (a:Si) on a transparent substrate (quartz)⁷

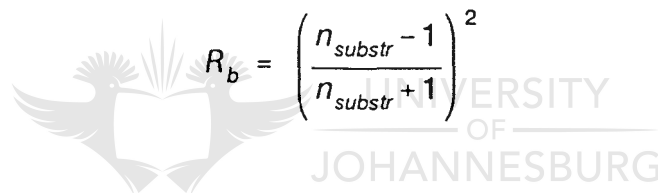
If the thickness d is not uniform, interference effects disappear and the transmission is a smooth curve, as shown by curve T_α in Figure 3.2. The spectrum can roughly be divided into four regions⁷. In the transparent region (1), $\alpha=0$ and the transmission is determined by n and n_{substr} through multiple reflections. In the region of weak

absorption (2), α is small, but already starts to reduce transmission. In the region of medium absorption (3), α is large and the transmission decreases mainly owing to the effect of α . However, if the thickness d is uniform, interference effects give rise to a spectrum, shown by the oscillating full curve T in Figure 3.2. The fringes can be utilised to calculate the optical constants of the film.

Transmission of a thick non-absorbing substrate is given by⁷

$$T_{substr} = \frac{(1-R_b)^2}{1-R_b^2} \quad (3.23)$$

where R_b is the reflectance at the boundary and is given by

$$R_b = \left(\frac{n_{substr} - 1}{n_{substr} + 1} \right)^2 \quad (3.24)$$


or

$$T_{substr} = \frac{2n_{substr}}{n_{substr}^2 + 1} \quad (3.25)$$

and

$$n_{substr} = \frac{1}{T_{substr}} + \sqrt{\frac{1}{T_{substr}^2} - 1} \quad (3.26)$$

The equation for interference fringes is

$$2nd = m\lambda \quad (3.27)$$

where m is an integer for maxima and a half integer for minima. Equation (3.27) includes a product of n and d , and it is not possible to obtain the values of either n or d separately using this equation only. The transmission T depicted in Figure 3.2 is a complicated function, $T = T(\lambda, n_{\text{substr}}, n, d, \alpha)$, and its most general form is⁷

$$T = \frac{Ax}{B - Cx + Dx^2} \quad (3.28)$$

where

$$\begin{aligned} A &= 16n_{\text{substr}}(n^2 + k^2) \\ B &= [(n+1)^2 + k^2][(n+1)(n+n_{\text{substr}}^2) + k^2] \\ C &= [(n^2 - 1 + k^2)(n^2 - n_{\text{substr}}^2 + k^2) - 2k^2n_{\text{substr}}^2 + 1]2\cos(\varphi) - \\ &\quad - k[2(n^2 - n_{\text{substr}}^2 + k^2) + (n_{\text{substr}}^2 + 1)(n^2 - 1 + k^2)]2\sin(\varphi) \\ D &= [(n-1)^2 + k^2][(n-1)(n-n_{\text{substr}}^2) + k^2] \end{aligned} \quad (3.29)$$

$$\varphi = \frac{4\pi nd}{\lambda}$$

$$x = \exp(-\alpha d)$$

$$\alpha = \frac{4\pi k}{\lambda}$$

The expression becomes simpler, however, if $k^2 \ll n^2$. Such approximation is valid over regions 1 and 2 and part of the 3 region of the spectrum in Figure 3.2. In this case Equation (3.28) becomes

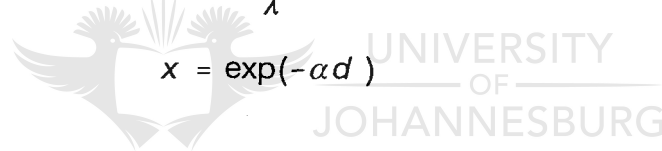
$$T = \frac{A_0 x}{B_0 - C_0 x \cos(\varphi) + D_0 x^2} \quad (3.30)$$

where

$$\begin{aligned} A_0 &= 16n^2 n_{\text{substr}} \\ B_0 &= (n+1)^3 (n + n_{\text{substr}}^2) \\ C_0 &= 2(n^2 - 1)(n^2 - n_{\text{substr}}^2) \\ D_0 &= (n-1)^3 (n - n_{\text{substr}}^2) \end{aligned} \quad (3.31)$$

$$\varphi = \frac{4\pi n d}{\lambda}$$

$$x = \exp(-\alpha d)$$



The extremes of the interference fringes, by taking $\cos(\varphi)$ equal 1 and -1, for maxima and minima, respectively, can be written as

$$\begin{aligned} T_M &= \frac{A_0 x}{B_0 - C_0 x + D_0 x^2} \\ T_m &= \frac{A_0 x}{B_0 + C_0 x + D_0 x^2} \end{aligned} \quad (3.32)$$

For subsequent analyses, T_M and T_m will be considered to be continuous functions of λ and, thus, of $n(\lambda)$ and $x(\lambda)$, as it is shown by the envelopes of the oscillating spectrum in Figure 3.2¹⁰. For any λ , T_M has an accompanying T_m .

In the region of transparency $\alpha=0$ and $x=1$ in Equations (3.32). If we substitute Equations (3.31) into Equations (3.32), it yields for T_M

$$T_M = \frac{2n_{substr}}{n_{substr}^2 + 1} \quad (3.33)$$

Equation (3.33) is analogous to Equation (3.25), and the maxima of the interference fringes are a function of n_{substr} only and coincide with T_{substr} . When maxima depart from T_{substr} , it shows the onset of absorption. Equation (3.33) can be used for calculation of n_{substr} in the transparent region using Equation (3.26).

Transmission at the minima is solved by substituting Equation (3.31) into Equation (3.32), and letting $x=1$:

$$T_m = \frac{4n^2 n_{substr}}{n^4 + n^2(n_{substr}^2 + 1) + n_{substr}^2} \quad (3.34)$$

or

$$n = \sqrt{M + \sqrt{M^2 - n_{substr}^2}} \quad (3.35)$$

where

$$M = \frac{2n_{substr}}{T_m} - \frac{n_{substr}^2 + 1}{2} \quad (3.36)$$

T_m , therefore, is a function of both n and n_{substr} , and, using Equation (3.35), n can be calculated from T_m .

In the region of weak and medium absorption, $\alpha > 0$ and $x < 1$. Subtracting the reciprocal of Equation (3.32) for maxima from the reciprocal of Equation (3.32) for minima yields an expression that is independent of x :

$$\frac{1}{T_m} - \frac{1}{T_M} = \frac{2C_0}{A_0} \quad (3.37)$$

Substituting Equation (3.31) into Equation (3.37) and solving for n gives us

$$n = \sqrt{P + \sqrt{P^2 - n_{substr}^2}} \quad (3.38)$$

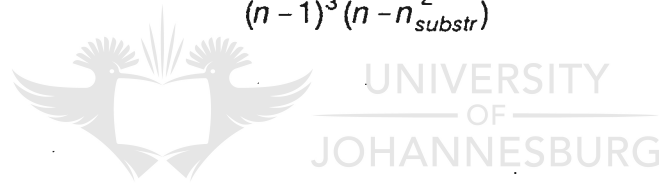
where

$$P = 2n_{\text{substr}} \frac{T_M - T_m}{T_M T_m} + \frac{n_{\text{substr}}^2 + 1}{2} \quad (3.39)$$

Equation (3.38) can be used to calculate $n(\lambda)$ from $T_M(\lambda)$ and $T_m(\lambda)$. This equation is identical to the formula derived by Manifacier¹⁰ using the theory for an infinitely thick substrate.

As soon as $n(\lambda)$ is known, all the constants in Equations (3.31) are known and x can be calculated in several ways. It was demonstrated, however, that best accuracy is obtained when calculating x from Equation (3.32) for maxima⁷:

$$x = \frac{E_M - \sqrt{E_M^2 - (n^2 - 1)^3 (n^2 - n_{\text{substr}}^4)}}{(n - 1)^3 (n - n_{\text{substr}}^2)} \quad (3.40)$$



where

$$E_M = \frac{8n^2 n_{\text{substr}}}{T_M} + (n^2 - 1)(n - n_{\text{substr}}^2) \quad (3.41)$$

Let us consider the region of strong absorption (4). All the interference fringes disappear. There is no way to calculate n and x independently in this region from the transmission spectrum alone. Values of n can be estimated by extrapolating the values

calculated in the other parts of the spectrum. The values of x can then be calculated, using Equation (3.40). For very large α , all curves converge to a single curve T_0 . If interference effects are ignored, Equation (3.30) can be written for $x \ll 1$ as

$$T_0 \approx \frac{A_0 x}{B_0} \quad (3.42)$$

or

$$x \approx \frac{(n+1)^3 (n+n_{substr}^2)}{16n^2 n_{substr}} T_0 \quad (3.43)$$

For the determination of n in the region of weak and medium absorption, the values of T_m and T_M at different λ must be obtained. Then, after having calculated d , the accuracy of these values can be improved by using accurate values of m and d and Equation (3.27). Next, n can be fitted to a function for extrapolation to the region of strong absorption. A function in the form of Cauchy's dispersion rule⁵,

$$n(\lambda) = A_c + \frac{B_c}{\lambda^2} + \frac{C_c}{\lambda^4} \quad (3.44)$$

could be used as a good approximation if least-square fit of the values of n can be performed.

Determination of thickness should be performed in the regions of transparency and weak absorption and be based on the equation derived from Equation (3.27). If n_1 and n_2 are refractive indices at two adjacent maxima (or minima) at λ_1 and λ_2 , it follows from Equation (3.27) that:

$$d = \frac{\lambda_1 \lambda_2}{2(\lambda_1 n_2 - \lambda_2 n_1)} \quad (3.45)$$

Equation (3.45) is very sensitive to errors in n and is not very accurate. The values of d calculated from Equation (3.45) should be used only as a first approximation⁷. These values should be used with n to determine the order numbers for the extremes from Equation (3.27). The accuracy will improve greatly by taking the exact integer (for maxima) or half-integer values of m (for minima) for each λ and again calculating the thickness, now from Equation (3.27).

Since $n(\lambda)$ is known, $x(\lambda)$ can be determined from $T_M(\lambda)$ using Equation (3.40). $\alpha(\lambda)$ can be calculated from $x(\lambda)$ and d , using Equation (3.31). However, it should be mentioned that, in the region of weak absorption, the value of α is very sensitive to any errors in measurements of transmission and should, therefore, be treated very carefully not to misinterpret the results. Once $\alpha(\lambda)$ is known, $k(\lambda)$ can be calculated from the following equation:

$$k = \frac{\alpha \lambda}{4\pi} \quad (3.46)$$

That completes the calculation of the optical constants of thin films.

3.4 Theory for the determination of band gap

The precise determination of the value of the band gap for a non-stoichiometric compound like SiO_xN_y is difficult. There is no single model which describes the nature of absorption near the absorption edge of amorphous thin films, because it is affected by the degree of disorder in the structure; chemical bonding and composition; various defect states in the forbidden band; and the degree of compensation of these defect states¹¹. Usually, for an analysis of the absorption coefficient, the wavelength range is divided into two regions (Urbach edge region and interband region), and two approximations are used. The Urbach rule for the low-energy (long wavelength) region ($\alpha < 10^4 \text{ cm}^{-1}$) states that¹¹:

$$\alpha = \alpha_0 \exp\left(\frac{h\nu - E_g}{E_0}\right) \quad (3.47)$$

where $h\nu$ = the incident photon energy,
 α_0 = a constant,
 E_g = value of optical band gap energy, and
 E_0 = the Urbach tail energy which gives the steepness of the defect level distribution near the band edge.

At higher energies (when $\alpha > 10^4 \text{ cm}^{-1}$), the absorption coefficient takes the following form:

$$\alpha = K \frac{(h\nu - E_g)^{m_p}}{h\nu} \quad (3.48)$$

where K is a constant. The constant m_p characterizes the transition process and can have values of 1/2, 2, 3/2 and 3 for allowed direct, allowed indirect, forbidden direct and forbidden indirect transitions, respectively¹². The usual method for determining the value of the optical band gap of indirect band gap materials is by plotting $(\alpha h\nu)^{1/2}$ (or $(\alpha h\nu)^2$ - for direct band gap materials) versus $h\nu$ (Tauc plot), or $(\alpha/h\nu)^{1/2}$ versus $h\nu$ (Cody plot¹³) and extrapolating the linear part to the x-axis. An alternative approach is to take the value of $h\nu$, at which $\alpha = 10^4 \text{ cm}^{-1}$, as an approximation for the band gap energy¹³. This is also the only approach if thick films (of the order of hundreds of nanometers) are under investigation, where it is not possible to measure the transmission at photon energies higher than the fundamental absorption edge.



3.5 Description of the software

The theory, described above, allows for direct implementation of an algorithm for calculation of complex refractive indices, thickness and absorption coefficient of thin films on transparent substrates. On the basis of these closed-type formulae, a computer program was developed for the extraction of optical properties of thin films from transmission spectra.

The program is written in MATLAB¹⁴. The files of transmission data of both substrate alone and substrate with thin film on it are used for calculations. The program performs calculations of refractive indices of the substrates, and thickness and optical properties of the thin film (refractive index, extinction coefficient, absorption coefficient and band gap energy taken at $\alpha=10^4 \text{ cm}^{-1}$). Manual inputs are needed during rough estimation of the coordinates of maxima and minima and orders of interference fringes. When the calculations are complete, results are saved as an ASCII file to allow further data processing, creation of graphs, etc.

3.6 The optical properties of the substrates

Due to the large variation of refractive index of the SiO_xN_y alloy three types of substrates were used during the investigation. Corning 7059 glass was used for characterization of highly absorbing materials with low nitrogen and oxygen content, whereas fused quartz and sapphire were used for characterization of materials with low absorption. All three types of substrates were characterized by optical transmission spectroscopy in the 200-2600 nm wavelength range. Respective transmission curves are shown in Figure 3.3. Refractive indices calculated according to Equation (3.26) are depicted in Figure 3.4. The refractive indices of fused quartz and sapphire reported by Palik^{1,2} are given for comparison in the same figure.

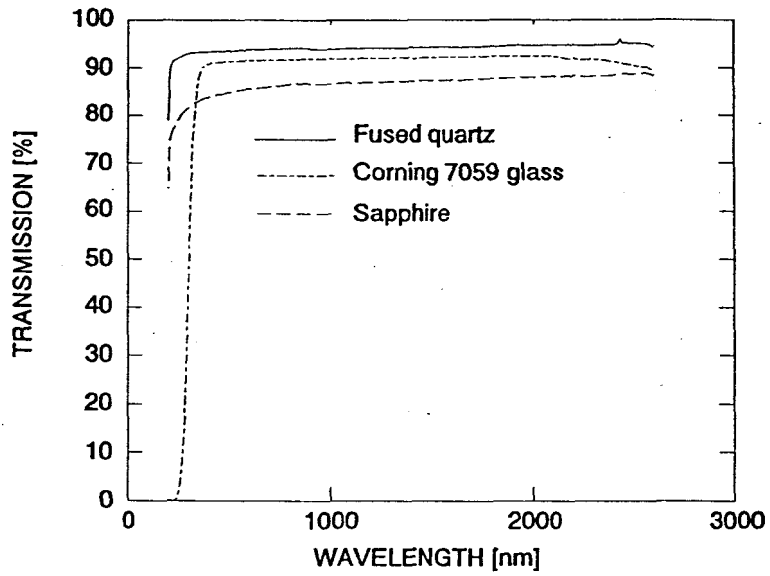


Figure 3.3: Transmission spectra of fused quartz, Corning 7059 glass and sapphire

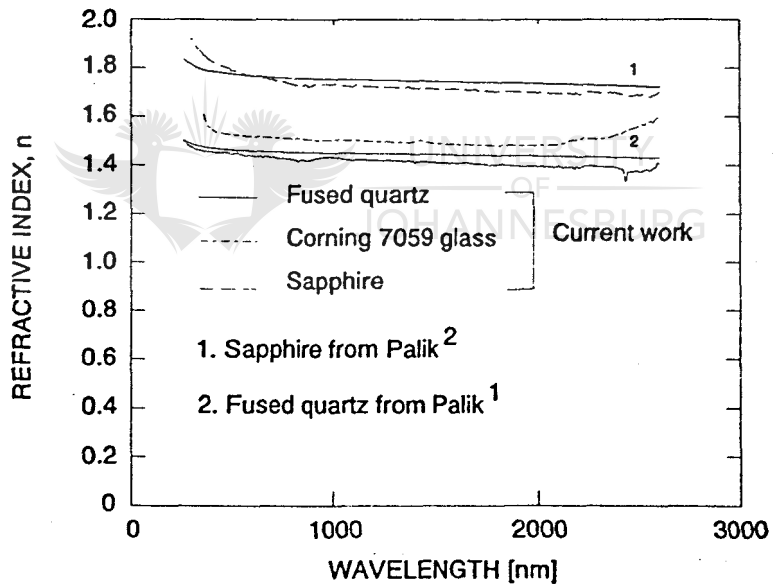


Figure 3.4: Refractive indices of fused quartz, Corning 7059 glass and sapphire in comparison with the data reported for fused quartz and sapphire by Palik^{1,2}

3.7 The optical properties of SiO_x

The real and imaginary parts of refractive indices, n and k , respectively, as obtained from the measurements, are within limits set by data for stoichiometric silicon dioxide and amorphous silicon presented by Palik¹. Figures 3.5 and 3.6 depict n and k , respectively as a function of wavelength for different SiH₄/(SiH₄+O₂) gas flow ratios. The information on actual gas flows during the deposition is given in the Table 3.1.

No	30% SiH ₄ in Ar (sccm)	9% O ₂ in Ar (sccm)
1	N/A	N/A
2	20.0	0.0
3	18.0	2.0
4	16.0	4.0
5	14.0	6.0
6	13.0	7.0
7	12.0	8.0
8	11.0	9.0
9	8.0	12.0
10	4.0	16.0
11	N/A	N/A

Table 3.1: Gas flows for set of experiments on SiO_x growth

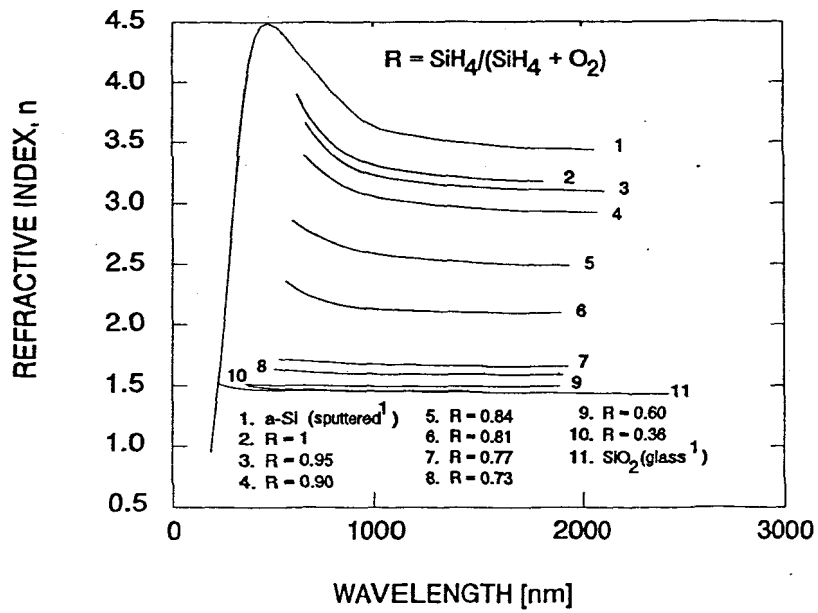


Figure 3.5: The refractive indices of SiO_x grown at different gas flow ratios

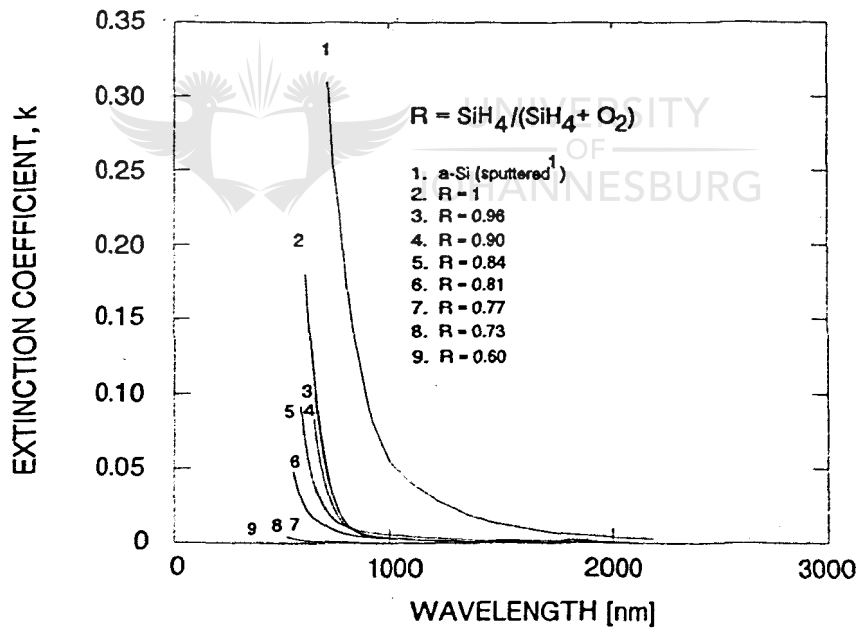


Figure 3.6: The extinction coefficients of SiO_x grown at different gas flow ratios

The difference between n and k for sputtered amorphous silicon¹ and material grown in a 30% silane in Ar mixture can be explained by the presence of substantial numbers of Si-H bonds in the last mentioned material. A decrease in the silane content of the gas mixture leads to a decrease in the refractive index over the wavelength range of interest. At the lowest gas flow ratio ($\text{SiH}_4/(\text{SiH}_4+\text{O}_2)=0.35$), the values of the refractive index are identical to those reported for stoichiometric silicon dioxide¹, whereas it is not possible to determine k because of the limited wavelength range of the spectrophotometer.

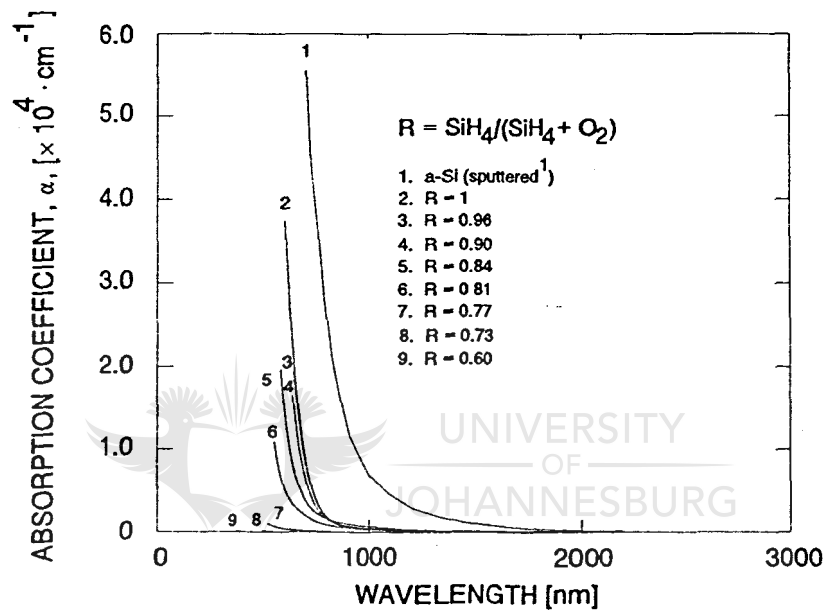


Figure 3.7: The absorption coefficients of SiO_x grown at different gas flow ratios

Calculated absorption coefficient α versus wavelength curves are shown in Figure 3.7. All layers are transparent in the region 900 to 2600 nm. However, there is a notable shift of the absorption edge towards shorter wavelengths with an increase in the oxygen content of the layer.

Using the calculated values of refractive index and the extinction coefficient, the transmission spectra for each of the grown layers were calculated and compared to the measured data. Figure 3.8 is a typical comparative graph showing excellent agreement. The particular graph is the measured and calculated spectra of a 0.92 μm -thick layer grown with an $\text{SiH}_4/(\text{SiH}_4+\text{O}_2)=0.8$ gas flow ratio.

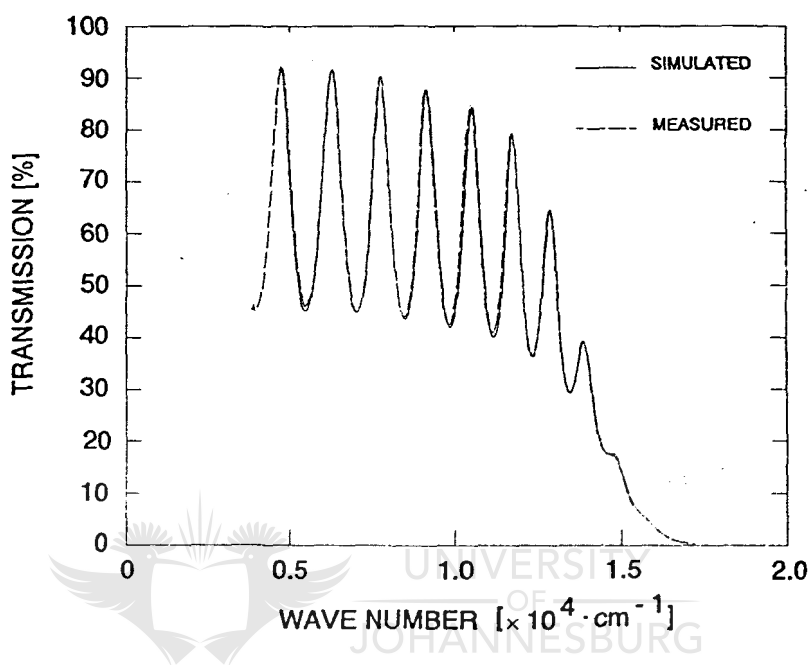


Figure 3.8: A comparison of measured and simulated transmission curves

Figure 3.9 depicts the values of optical band gap energy taken as the photon energy at which α is equal to 10^4 cm^{-1} versus gas flow ratio. It increases from 1.8 to more than 6 eV with a decrease in the gas flow ratio corresponding to an increase in the oxygen content in the film (a decrease in the refractive index). This indicates the transition from silicon to silicon dioxide in the chemical composition of the film. Note that the greatest

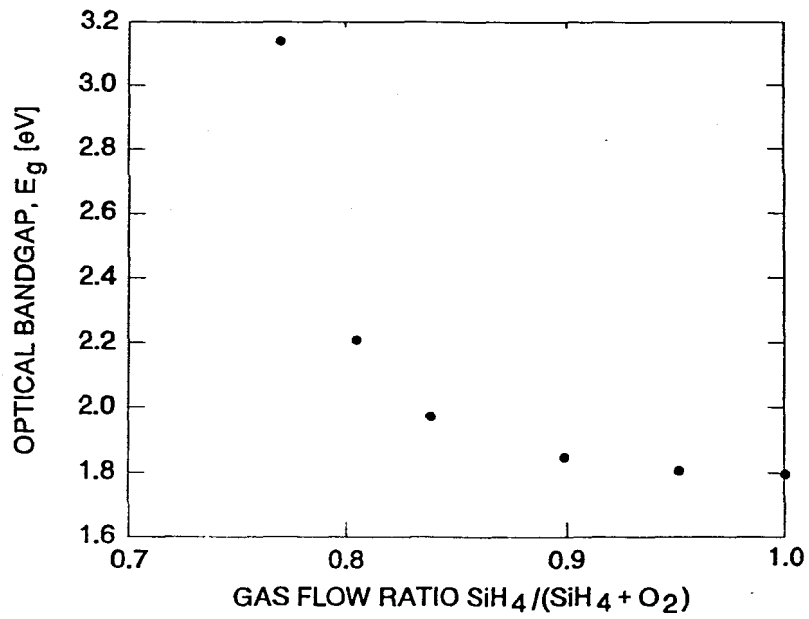


Figure 3.9: The band gap of SiO_x grown at the different gas flow ratios

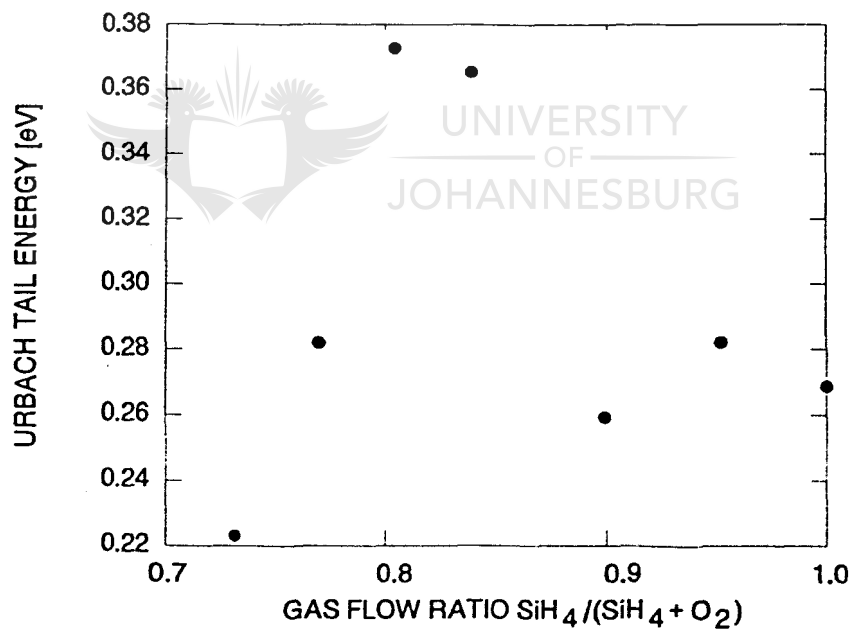


Figure 3.10: Urbach tail energy of SiO_x grown at the different gas flow ratios

value shown is only 3.16. Increasing the oxygen flow resulted in the deposition of SiO_x with values of band gap energy that are larger than can be determined by the spectrophotometer used. Another limitation is caused by absorption in the substrate.

The dependence of the Urbach tail energy (which is usually connected to the degree of disorder in the material¹¹) on the gas flow ratio is shown in Figure 3.10. It is difficult to interpret this data, however, because there is no clear tendency in the Urbach tail energy values. The values of Urbach tail energies are considerably higher than for RF-PECVD material¹³. The reason, most probably, lies in the low hydrogen content, usually found in ECR-grown films. Intense ion bombardment due to self-bias of approximately -170 V also may cause defects in thin film structure¹⁵.

3.8 The optical properties of SiN_x



UNIVERSITY
OF
JOHANNESBURG

The real and imaginary parts of refractive indices, n and k , respectively, as obtained from the measurements, are within limits (or very close to it in the case of Si_3N_4) set by data for stoichiometric silicon nitride and amorphous silicon presented by Palik¹. Figures 3.11 and 3.12 depict n and k , respectively, as a function of wavelength for different $\text{SiH}_4/(\text{SiH}_4+\text{N}_2)$ gas flow ratios. The information on actual gas flows during the deposition is given in Table 3.2. An increase of the silane content in the gas mixture leads to an increase in the refractive index over the wavelength range of interest. At the

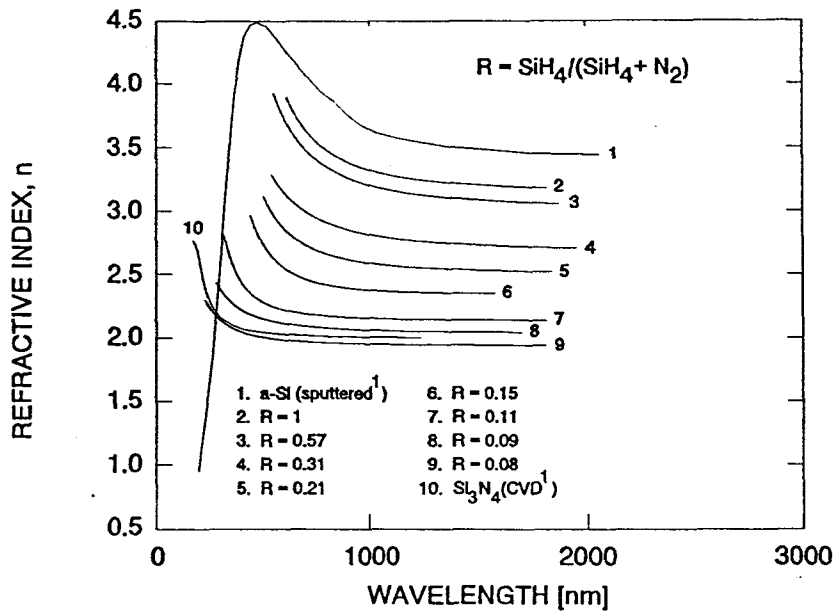


Figure 3.11: The refractive index of SiN_x grown at different gas flow ratios

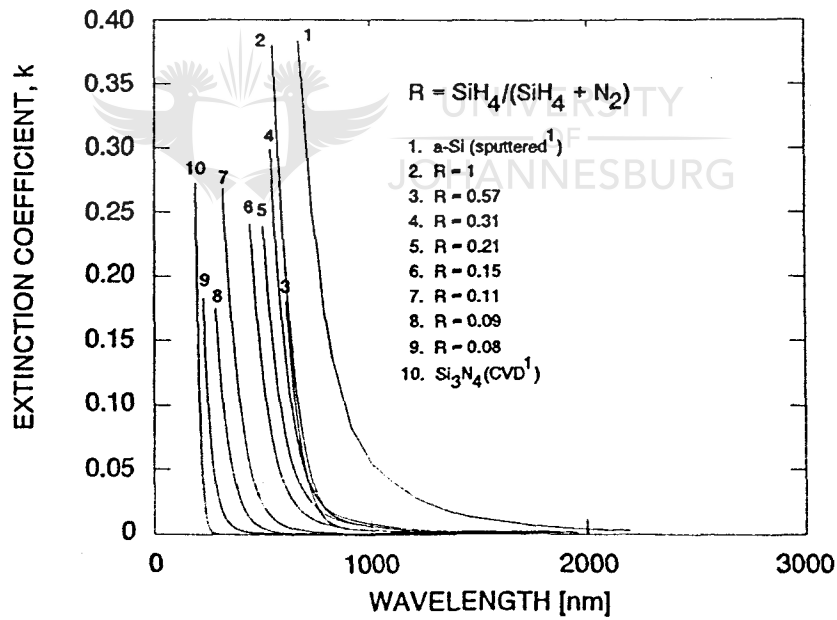


Figure 3.12: The extinction coefficient of SiN_x grown at different gas flow ratios

lowest gas flow ratio ($R = \text{SiH}_4 / (\text{SiH}_4 + \text{N}_2) = 0.08$), the values of refractive index are almost identical to those reported for stoichiometric silicon nitride¹.

No	30% SiH ₄ in Ar (sccm)	N ₂ (sccm)
1	N/A	N/A
2	20.0	0.0
3	16.0	4.0
4	11.5	8.5
5	9.0	11.0
6	7.0	13.0
7	5.4	14.6
8	4.7	15.3
9	4.0	16.0
10	N/A	N/A

Table 3.2: Gas flows for set of experiments on SiN_x growth

Calculated absorption coefficient α versus wavelength curves are shown in Figure 3.13. All layers are transparent in the region 900 to 2600 nm. However, there is a notable shift of the absorption edge towards shorter wavelengths with an increase in the nitrogen content of the layer.

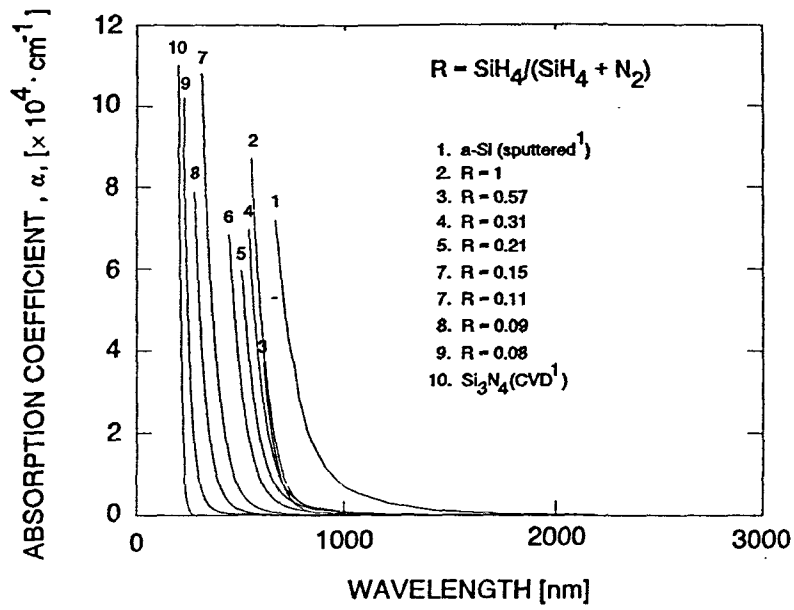


Figure 3.13: The absorption coefficient of SiN_x grown at different gas flow ratios

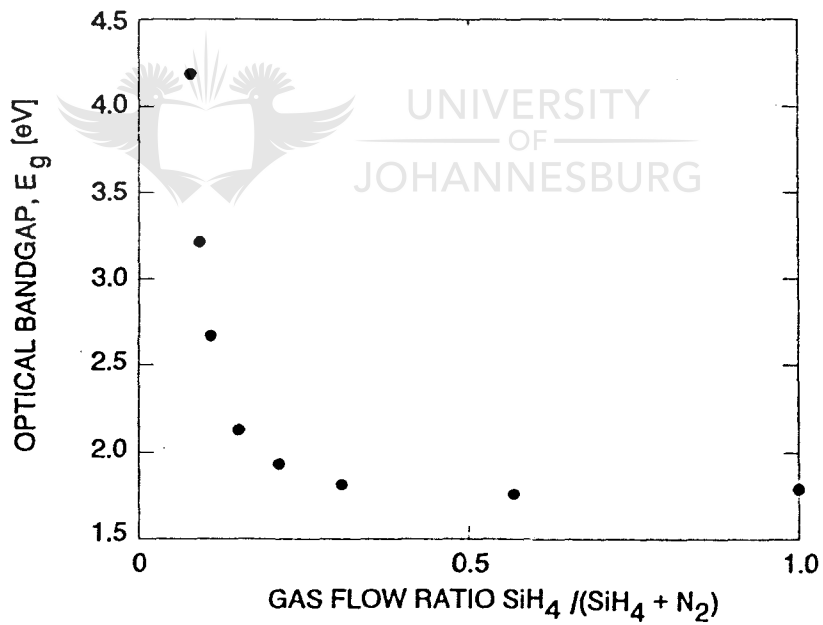


Figure 3.14: The optical band gap of SiN_x grown at different gas flow ratios

Figure 3.14 depicts the values of the optical band gap energy taken as the photon energy at which α is equal to 10^4 cm^{-1} versus the gas flow ratio. One can easily see that the band gap increases from 1.8 to 4.2 eV with a decrease in the gas flow ratio in accordance with an increase in the nitrogen content of the film (a decrease in the refractive index). This indicates the transition from silicon to silicon nitride in the chemical composition of the film. These values of the band gap energy are similar to values usually found in films with a very low hydrogen content¹⁶⁻¹⁸.

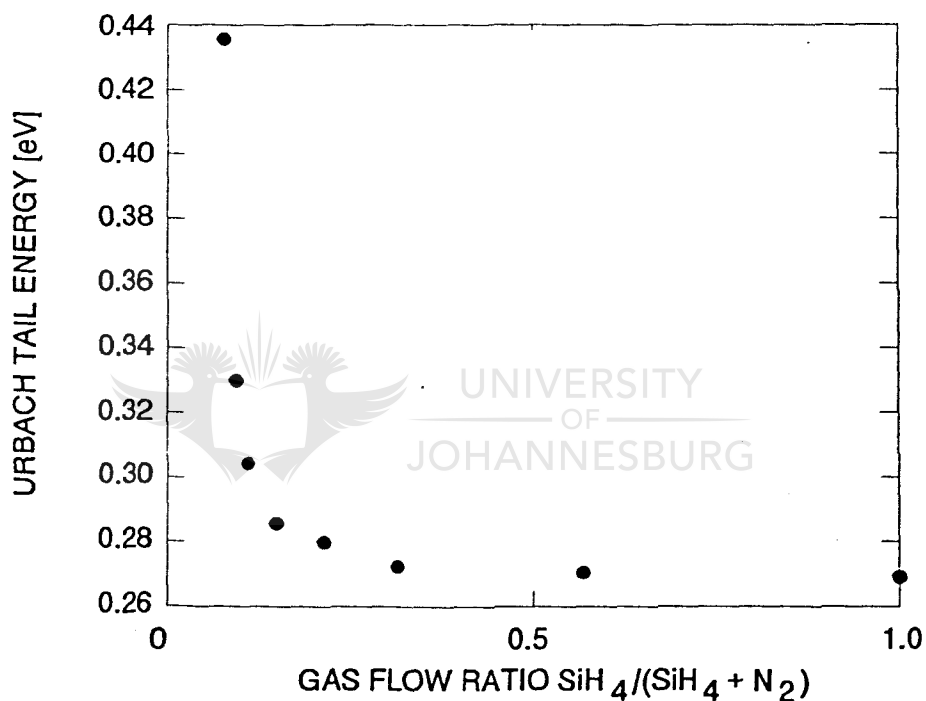


Figure 3.15: Urbach tail energy for SiN_x grown at different gas flow ratios

The dependence of the Urbach tail energy on the gas flow ratio is shown in Figure 3.15. One can infer that the defect density increases with an increase in the nitrogen content.

The values of Urbach tail energies, E_0 , for films with low nitrogen content, are considerably larger than the values found for RF plasma-deposited films^{13,16}, and could be explained by a very low hydrogen content in the films. Hydrogen, which is much more abundant in RF plasma-grown amorphous Si and SiN_x films, is responsible for the passivation of dangling bonds in the material, and causes a marked decrease in the Urbach tail energy¹³ and a blue shift in absorption curves^{17,19}. Ion bombardment during deposition also can substantially increase the Urbach tail energy¹³.

3.9 The optical properties of SiO_xN_y

A "process trajectory" followed during these experiments is shown in Figure 3.16. Points on this graph correspond to the values of O₂/SiH₄ and N₂/SiH₄ flow ratios for which layers were grown. Specific points have been chosen to satisfy the need for a large excursion of the refractive index for optical interference filter manufacturing.

The real and imaginary parts of refractive indices, n and k , as obtained from the measurements, are depicted in Figures 3.17 and 3.18, respectively as a function of the wavelength for different gas compositions. The numbers on curves correspond to the respective point numbers on the process trajectory. An increase in the silane content of the gas mixture leads to an increase in the refractive index over the wavelength range of interest.

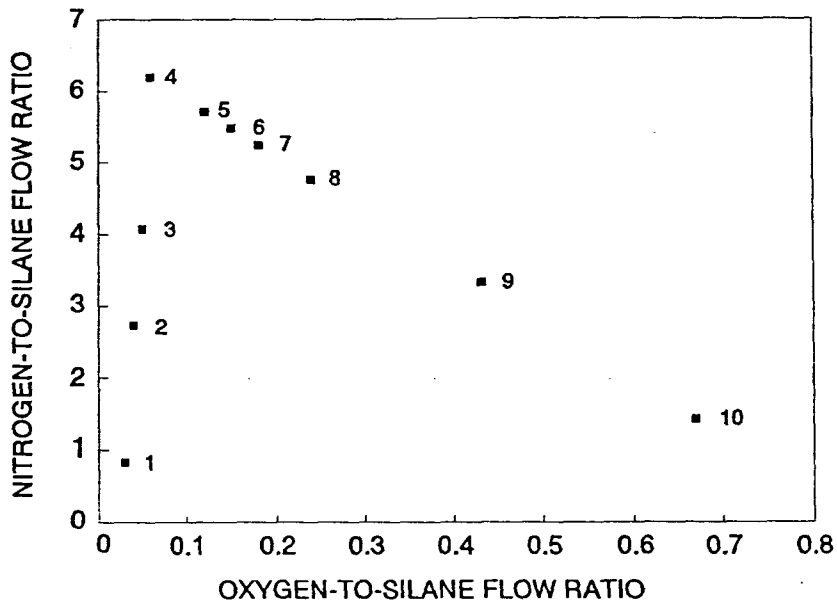


Figure 3.16: The process trajectory for the growth of SiO_xN_y samples

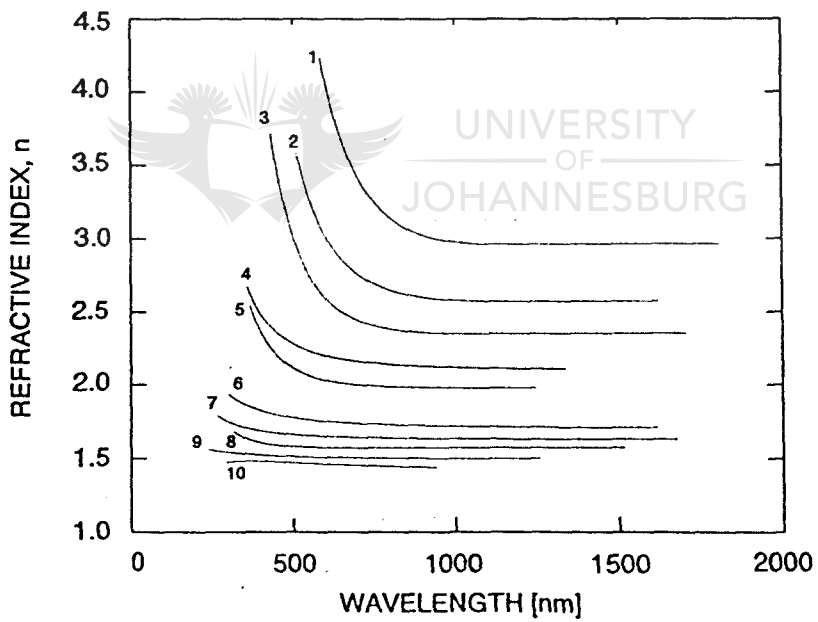


Figure 3.17: The refractive index of SiO_xN_y grown at different gas flow ratios

Point number	30% SiH ₄ in Ar (sccm)	9% O ₂ in Ar (sccm)	N ₂ (sccm)
1	16	1	4
2	11	1	9
3	9	1	11
4	7	1	13
5	7	2	12
6	7	2.5	11.5
7	7	3	11
8	7	4	10
9	7	7	7
10	7	11	3

Table 3.3: Gas flows at the respective points of the "process trajectory"

All layers are transparent in the 900 to 2600 nm region. However, there is a notable shift of the absorption edge towards shorter wavelengths with an increase in nitrogen and oxygen content of the layer, as is evident in Figure 3.19. Points 9 and 10 are absent in Figures 3.18 and 3.19 due to high transparency of the respective films in the working range of the spectrophotometer.

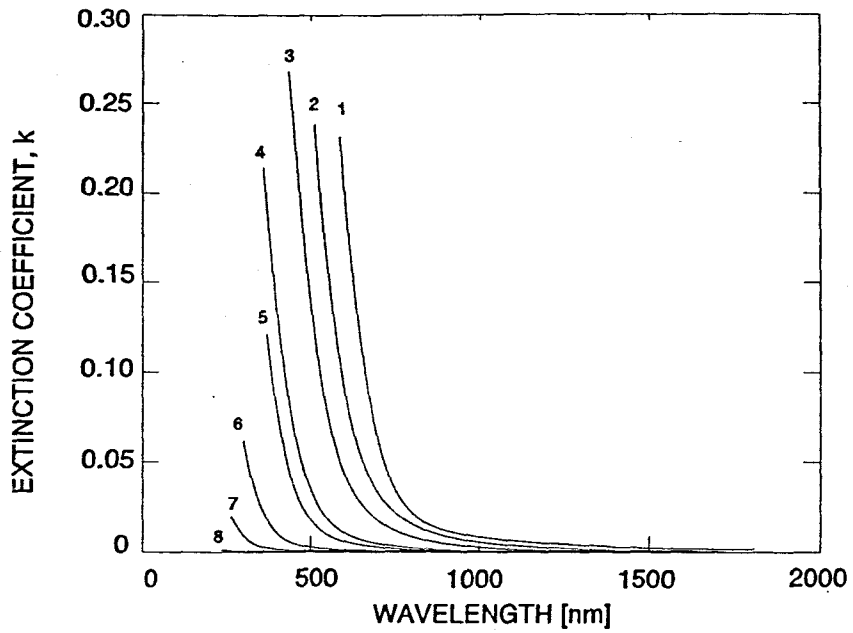


Figure 3.18: The extinction coefficient of SiO_xN_y grown at different gas flow ratios

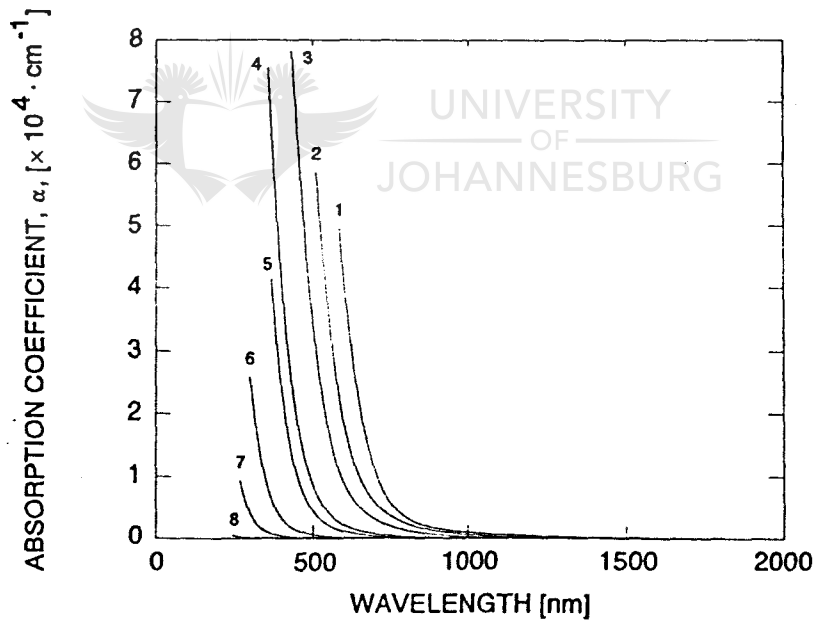


Figure 3.19: The absorption coefficient of SiO_xN_y grown at different gas flow ratios

The values of the optical band gap taken as the photon energy at which α is equal to 10^4 cm^{-1} for SiO_xN_y materials are presented in Figure 3.20. Band gap energy increases from 1.7 to more than 6 eV (not shown on graph) with an increase in the proportion of nitrogen and oxygen in the gas composition, in accordance with an increase in the nitrogen and oxygen content of the film (a decrease in the refractive index). This indicates the transition from amorphous silicon to a silicon-rich silicon oxynitride and further to silicon dioxide.

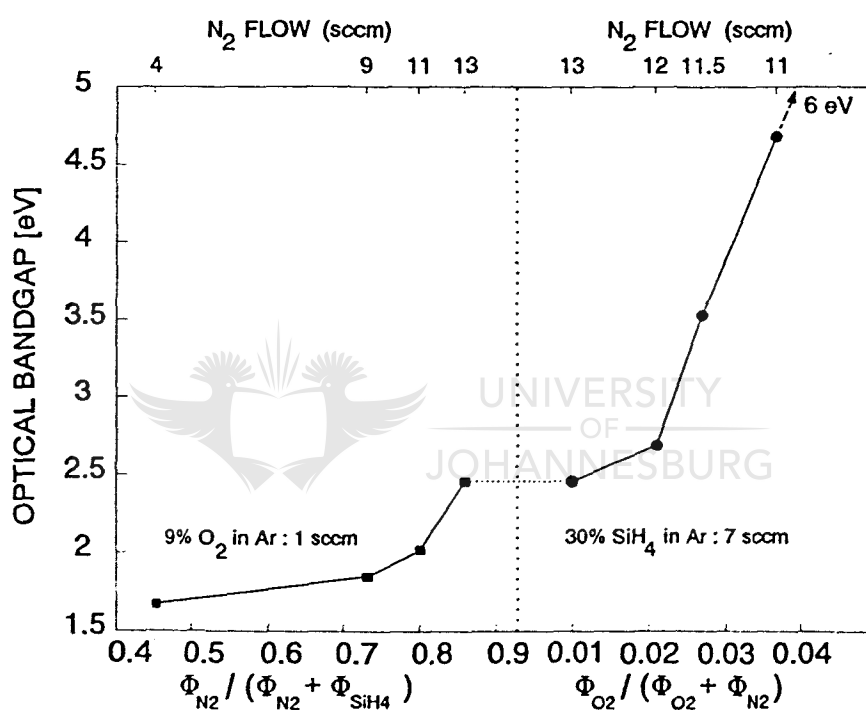


Figure 3.20: The band gap of SiO_xN_y grown at different gas flow ratios

3.10 Conclusions

The investigation produced new information on the optical properties of ECR-PECVD-grown SiO_x , SiN_x and SiO_xN_y thin films in the 200 to 2600 nm wavelength range. The calculated results show a strong dependence of n , k and α on composition of the gas mixture during deposition. The refractive index versus the wavelength curves for the SiO_x and SiN_x materials grown at a gas composition with a low silane content are almost identical to those for stoichiometric SiO_2 and Si_3N_4 films, respectively. These values are close to corresponding values for films grown by thermal oxidation¹, high-temperature CVD¹ and reactive ion plating¹⁹, suggesting a small amount of hydrogen in the films. These results agree with those previously reported for ECR-PECVD grown films^{20,21}.

With a decreasing silicon content in the film, k , α and E_g exhibit a strong blue shift. The explanation for this fact can be found in two models currently being used to describe the bonding structure of non-stoichiometric SiN_x , SiO_x and SiO_xN_y ^{18,22-24}. This blue shift can be linked to the substitution of Si-Si bonds with Si-O and/or Si-N bonds (in the case of the random bonds network model) or to the decrease of the a-Si-phase in comparison with the SiO_2 - and/or Si_3N_4 -phases (in the case of the two separate phase model). The estimated values of the optical band gap lie between 1.7 and 4.2 eV for SiN_x and between 1.7 to more than 6 eV for SiO_x . The transmission curves calculated using the measured optical constants agree well with the experimental spectra.

The range of optical parameters available in SiO_xN_y thin films demonstrates that ECR-PECVD can be used for the fabrication of optical filters with pre-programmed graded refractive index profiles by controlling the gas flows of silane, nitrogen and oxygen, respectively.



REFERENCES FOR CHAPTER 3

1. E.D. Palik (Editor), Handbook of Optical Constants of Solids, Academic Press, Orlando, Florida, 1985.
2. E.D. Palik (Editor), Handbook of Optical Constants of Solids II, Academic Press, San Diego, California, 1991.
3. W.L. Wolf, "Properties of Optical Materials", in Handbook of Optics (Eds. W.G. Driscoll and W. Vaughan), McGraw-Hill, New York, 1978, pp. 7.1-7.157.
4. H.A. Macleod, Thin Film Optical Filters, Adam Hilger Ltd., Bristol, 1986.
5. M.E. Thomas, "Optical Properties of IR materials", Thin Solid Films, Vol. 206, No. 1&2, 1991, pp. 241-247.
6. S.A. Alterovitz, J.A. Woollam, P.G. Snyder, "Variable angle spectroscopic ellipsometry", Solid State Technology, Vol. 31, No. 4, 1988, pp. 99-102.
7. R. Swanepoel, "Determination of the thickness and optical constants of amorphous silicon", Journal of Physics E: Scientific Instruments, Vol. 16, No. 12, 1983, pp. 1214-1222.
8. R. Swanepoel, "Determining refractive index and thickness of thin films from wavelength measurements only", Journal of the Optical Society of America, Vol. 2, No. 8, 1985, pp. 1339-1343.
9. R. Swanepoel, "Transmission and reflection of an absorbing thin film on an absorbing substrate", South African Journal of Physics, Vol. 12, No. 4, 1989, pp. 148-156.

10. J.C. Manifacier, J. Casiot, and J.P. Fillard, "A simple method for the determination of the optical constants n , k and the thickness of a weakly absorbing thin film", *Journal of Physics E: Scientific Instruments*, Vol.9, No. 11, 1976, pp. 1002-1004.
11. K.W. Böer, *Survey of Semiconductor Physics*, Van Nostrand Reinhold, New York, 1990.
12. D. Bhattacharyya, S. Chaudhuri and A.K. Pal, "Bandgap and optical transitions in thin films from reflectance measurements", *Vacuum*, Vol. 43, No. 4, 1992, pp. 313-316.
13. Y. Cros, J.C. Rostaing, J. Peisner, G. Leveque and C. Ance, "Optical properties of plasma-enhanced chemical vapour deposited silicon-oxynitride films", *Journal of Applied Physics*, Vol. 62, No. 11, 1987, pp. 4538-4544.
14. 386-MATLAB User's Guide, The MathWorks, Inc., South Natick, 1989.
15. J.R. McNeil, A.C. Barron, S.R. Wilson and W.C. Herrmann, Jr., "Ion-assisted deposition of optical thin films: low energy vs high energy bombardment", *Applied Optics*, Vol. 23, No. 4, 1984, pp. 552-559.
16. Z. Yin and F.W. Smith, "Studies of the deposition of high quality N-rich amorphous silicon nitride films", *Journal of Non-Crystalline Solids*, Vol. 137&138, 1991, pp. 879-882.
17. D. Schalch, A. Scharmann and R. Wolfrat, "The role of hydrogen in silicon nitride and silicon oxynitride films", *Thin Solid Films*, Vol. 124, 1985, pp. 301-308.
18. S. Logothetis, J. Petalas, A. Markwitz and R.L. Johnson, "Optical and compositional studies of SiN thin films with conventional and synchrotron ellipsometry", *Journal of Applied Physics*, Vol. 73, No. 12, 1993, pp. 8514-8518.

19. B.G. Bovard, J. Ramm, R. Hora and F. Hanselman, "Silicon nitride thin films by low voltage reactive ion plating: optical properties and composition", *Applied Optics*, Vol.28, No.20, 1989, pp. 4436-4441.
20. S.Yu. Shapoval, Ch.V. Kopezky and O.E. Bal'vinsky, "Deposition of silicon nitride layers using the magnetic-field-held SHF-plasma in conditions close to cyclotron resonance", *USSR Poverhnost'. Fizika, khimia, mekhanika* (Surface. Physics, chemistry, mechanics), No. 3, 1989, pp. 92-95.
21. K.A. Buckle, K. Pastor, C. Constantine and D. Johnson, "Parametric evaluation of electron cyclotron resonance deposited SiO₂ using a multicusp plasma applicator", *Journal of Vacuum Science and Technology B*, Vol. 10, No. 3, 1992, pp. 1133-1138.
22. A.V. Rzhhanov (Editor), *Silicon nitride in electronics*, Elsevier Science, Amsterdam, 1988, pp. 138-187.
23. S. Hasegava, T. Inokuma, and Y. Kurata, "Structural and bonding properties of amorphous silicon nitride films", paper presented at Symposium on Amorphous and Insulating Thin Films II, E-MRS Spring Meeting, Strasbourg, May 23-27, 1994, (will be published in *Journal of Non-Crystalline Solids*).
24. J. Robertson, "Defects and hydrogen in amorphous silicon nitride", *Philosophical Magazine B*, 1994, Vol. 69, No. 2, pp. 307-326.

CHAPTER 4

THE BASICS OF THIN FILM OPTICS AND DESIGN TECHNIQUES FOR GRADED REFRACTIVE INDEX OPTICAL COATINGS

4.1 Introduction

Thin film interference optical coatings have found numerous applications in the engineering practice. Besides its widespread use in military-related technologies, many

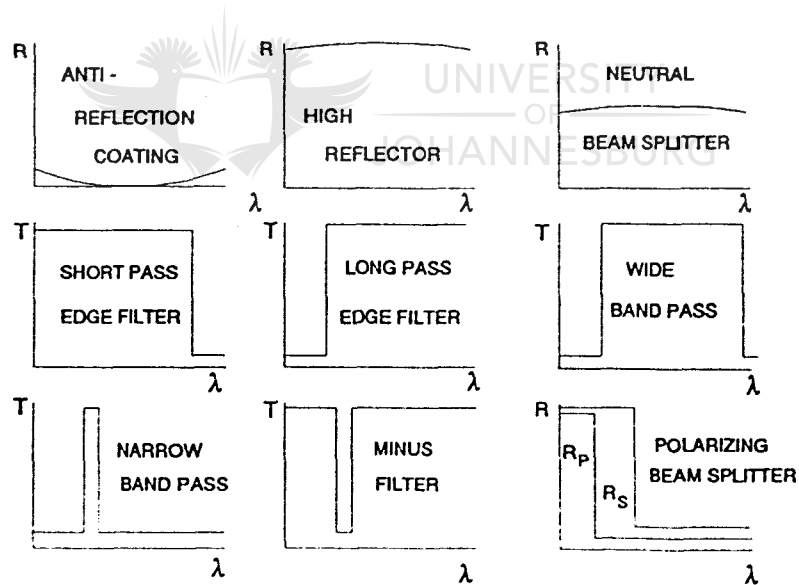


Figure 4.1: The transfer functions of main optical interference coatings¹

types of optical coatings are used in scientific and medical instrumentation, photo and video equipment, electronics and telecommunications. And all that owing to the ability of optical coatings selectively to reflect and transmit specific wavelengths of light. The main types of optical interference coatings are represented in Figure 4.1¹.

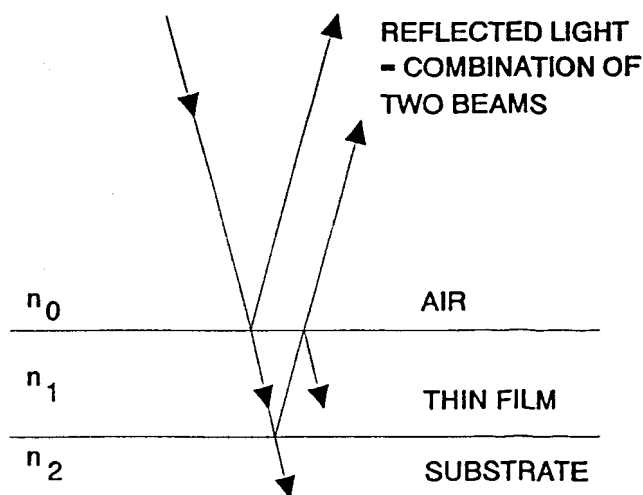


Figure 4.2: The reflection and transmission of light by a single thin film

The design of optical thin films is based on three main principles²:

1. When light is reflected at any boundary between two media, the amplitude of reflectance is given by $(1-\rho)/(1+\rho)$, where ρ is a ratio of refractive indices at the boundary.
2. When light, incoming from a medium with a given refractive index, is reflected at the boundary with a medium of higher refractive index, there is a phase shift of 180° . When reflection takes place at the boundary with a medium possessing lower refractive index than that of an adjoining medium, there is no phase shift.

3. If light is split into two components by reflection at the top and bottom surfaces of a thin film, as illustrated in Figure 4.2, then the beams will interfere. The resultant amplitude, consequently, will either be the difference of the amplitudes of the two components if the relative phase shift is 180° or the sum of the amplitudes if the relative phase shift is either 0° or a multiple of 360° . All other cases where the phase shift is different from either 180° or divisible by 360° will be intermediate between these two.

When reflectance and transmittance of a stack of films with homogeneous refractive indices need to be calculated, it can be done by direct solution of the wave equation with appropriate boundary conditions. Another, more convenient, way of calculating reflectance and transmittance for a stack of films with homogeneous refractive indices is by applying the above-mentioned principles within the bounds of the so-called "matrix method". We will discuss the matrix method later in this chapter.

In the case of inhomogeneous refractive index films, however, the situation is more complex. Theoretical treatment in this case is difficult, because the wave equation can be solved explicitly in terms of known functions in a few special cases only, and even then, the expressions are complicated³. But even in such a situation, the matrix method can be used successfully, provided that the inhomogeneous layer be replaced by a sufficient number of thin homogeneous layers, of which the refractive index pattern contours the index profile $n(x)$, as shown in Figure 4.3.

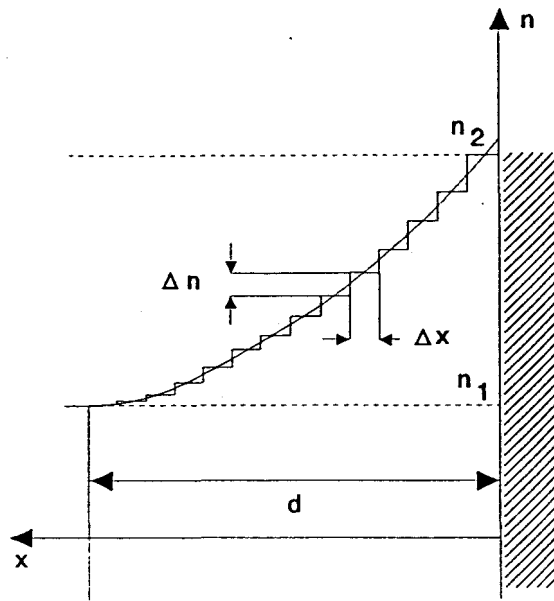


Figure 4.3: The approximation to an inhomogeneous film by a number of homogeneous thin layers³

4.2 The basics of thin film optics. The matrix method

Let us start with a description of the system of notation which is thought to be the most convenient for implementation on computers^{2,4}. We will denote the electric and magnetic vectors of the electromagnetic wave that travels in the positive direction in the m -th layer by E_m^+ and H_m^+ , respectively. Respective vectors for a wave travelling in the negative direction will be represented as E_m^- and H_m^- . Thus, resulting tangential fields E_m and H_m in the m -th layer may be expressed in terms of E_m^+ and E_m^- , as follows:

$$\begin{aligned} E_m &= E_m^+ + E_m^- \\ H_m &= \eta_m (E_m^+ - E_m^-) \end{aligned} \quad (4.1)$$

For normal incidence, η_m will be equal to the refractive index of the m -th layer, n_m . At an arbitrary angle of incidence θ_m , for the p -component of polarisation η_m can be calculated as follows

$$\eta_m = n_m / \cos \theta_m,$$

whereas for the s -component of polarisation:

$$\eta_m = n_m \cos \theta_m,$$

The phase shift of the wave traversing the m -th layer is given by

$$\delta_m = \frac{2\pi n_m d_m \cos \theta_m}{\lambda} \quad (4.2)$$

where λ = the wavelength of the radiation,
 d_m = the physical thickness of the m -th layer, and
 $n_m d_m$ = is a quantity known as the "optical thickness".

δ_m is sometimes called the "phase thickness" of the layer⁴. The system of notation is illustrated in Figure 4.4. The refractive indices of the medium of incidence, the m -th layer and the substrate are denoted by n_0 , n_m and n_{substr} , respectively.

If the m -th medium is absorbing, n_m should be replaced by the complex quantity $N_m =$

$n_m - ik_m$, where i is the square root of -1 and k_m is the extinction coefficient which is a measure of the absorption in the material.

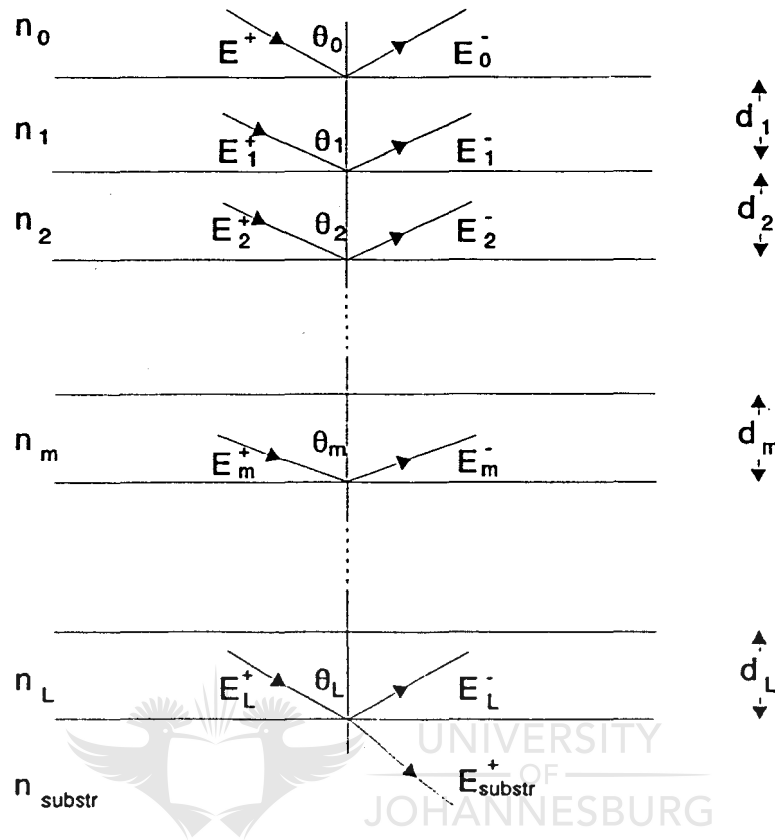


Figure 4.4: System of notation

First we will consider the reflectance and transmittance at a single boundary between two homogeneous media. Because an electromagnetic wave is a form of energy transport, the energy associated with a wave can be observed. The Poynting vector, S , represents the energy flux and is given by

$$\mathbf{S} = \mathbf{E} \times \mathbf{H} . \quad (4.3)$$

A time-averaged quantity $\bar{\mathbf{S}}$ is measured experimentally and for real N we obtain

$$\bar{\mathbf{S}} = \left(\frac{1}{2} \text{Re} (E\mathbf{H}^*) \right) \cdot \mathbf{r} \quad (4.4)$$

where $E, H =$ vector amplitudes,

$\mathbf{r} =$ a unit vector in the direction of propagation of the electromagnetic wave

and $*$ denotes the complex conjugate. Taking into account, that for a medium of index n , $n(\mathbf{r} \times \mathbf{E}) = \mathbf{H}$, Equations (4.3) and (4.4) may be expressed as

$$\mathbf{S} = n |\mathbf{E}|^2 \mathbf{r} \quad (4.5)$$

and

$$\bar{\mathbf{S}} = \frac{n}{2} |\mathbf{E}|^2 \mathbf{r} \quad (4.6)$$

respectively.

The problem of determining the light reflected and transmitted at the boundary separating two media should be dealt with by applying the appropriate boundary

conditions to the solutions of Maxwell's equations. If the wave propagates in an isotropic, non-conducting medium in which there is no space charge, these equations are

$$\begin{aligned}\epsilon\mu \frac{\partial^2 \mathbf{E}}{\partial t^2} &= \nabla^2 \mathbf{E} \\ \epsilon\mu \frac{\partial^2 \mathbf{H}}{\partial t^2} &= \nabla^2 \mathbf{H}\end{aligned}\tag{4.7}$$

These are the simple forms of the wave equation, which states that waves are propagating with velocity $c/(\mu\epsilon)^{1/2}$. However, at optical frequencies the value of μ for all materials of interest can be regarded as unity. Thus, the velocity of propagation is $c/(\epsilon)^{1/2}$, where ϵ is the relative dielectric permittivity of the material, and from the definition of refractive index given in chapter 3 we know that $n=(\epsilon)^{1/2}$.



The boundary conditions require that the tangential components of both the electric and magnetic field vectors should be continuous across the boundary. Let us consider the situation which is illustrated in Figure 4.5: a plane wave is incident on the boundary, defined by $z = 0$, between the medium of incidence (refractive index n_0) and adjoining medium (refractive index n_1). We denote the amplitudes of the electric vectors of the wave approaching the boundary by E^+_{0p} and E^+_{0s} , and those of the transmitted wave are E^+_{1p} and E^+_{1s} , respectively (subscripts p and s denote the p - and s -components of polarisation).

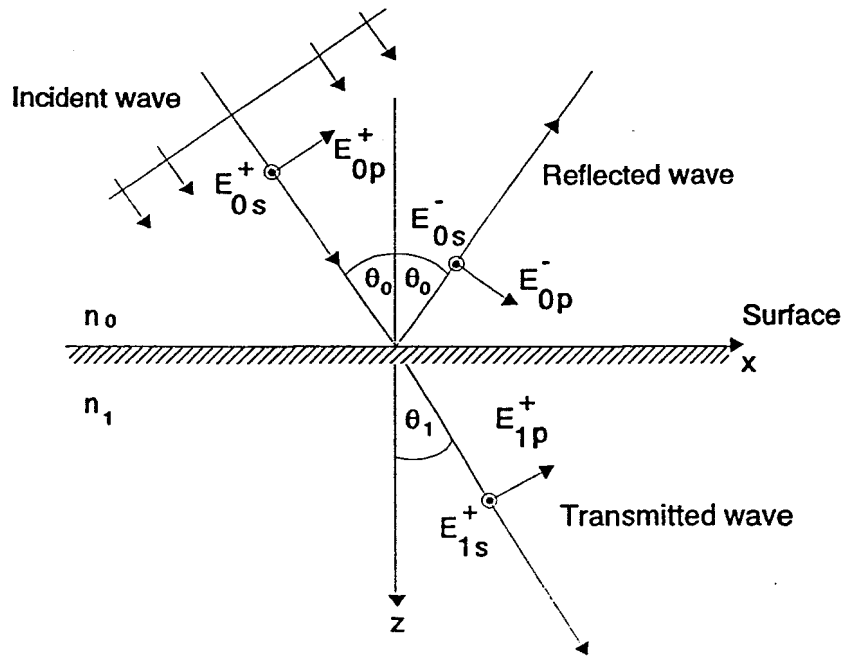


Figure 4.5: Reflection and refraction at the surface of the thin film

The phase factors associated with the incident, transmitted and reflected waves are⁴

$$\left. \begin{array}{l} \exp \left[i \left(\omega t - \frac{2\pi n_0}{\lambda} (x \sin \theta_0 + z \cos \theta_0) \right) \right], \\ \exp \left[i \left(\omega t - \frac{2\pi n_0}{\lambda} (x \sin \theta_0 - z \cos \theta_0) \right) \right], \\ \exp \left[i \left(\omega t - \frac{2\pi n_1}{\lambda} (x \sin \theta_1 + z \cos \theta_1) \right) \right], \end{array} \right\} \begin{array}{l} \textit{incident wave}, \\ \textit{reflected wave}, \\ \textit{transmitted wave}. \end{array}$$

The direction of the incident light in this notation is positive. By applying the boundary

conditions at $z = 0$, we obtain

$$\begin{aligned}
 E_{0x} &= (E_{0p}^+ + E_{0p}^-) \cos\theta_0 = E_{1x} = E_{1p}^+ \cos\theta_1 \\
 E_{0y} &= E_{0s}^+ + E_{0s}^- = E_{1y} = E_{1s}^+ \\
 H_{0x} &= n_0(-E_{0s}^+ + E_{0s}^-) \cos\theta_0 = H_{1x} = -n_1 E_{1s}^+ \cos\theta_1 \\
 H_{0y} &= n_0(E_{0p}^+ - E_{0p}^-) = H_{1y} = n_1 E_{1p}^+
 \end{aligned} \tag{4.8}$$

From Equations (4.8) one can obtain the ratios of the amplitudes of transmitted and reflected waves to the amplitude of incident waves for each component of polarisation.

These ratios are known as the Fresnel coefficients of reflection and Fresnel coefficients of transmission and they are:

$$\begin{aligned}
 r_{1p} &= \frac{E_{0p}^-}{E_{0p}^+} = \frac{n_0 \cos\theta_1 - n_1 \cos\theta_0}{n_0 \cos\theta_1 + n_1 \cos\theta_0} \\
 r_{1s} &= \frac{E_{0s}^-}{E_{0s}^+} = \frac{n_0 \cos\theta_0 - n_1 \cos\theta_1}{n_0 \cos\theta_0 + n_1 \cos\theta_1} \\
 t_{1p} &= \frac{E_{1p}^+}{E_{0p}^+} = \frac{2n_0 \cos\theta_0}{n_0 \cos\theta_1 + n_1 \cos\theta_0} \\
 t_{1s} &= \frac{E_{1s}^+}{E_{0s}^+} = \frac{2n_0 \cos\theta_0}{n_0 \cos\theta_0 + n_1 \cos\theta_1}
 \end{aligned} \tag{4.9}$$

The reflection coefficients or reflectances (defined as the ratios of reflected to transmitted energies) may be obtained using Equation (4.6). They are

$$\mathfrak{R}_p = \frac{(E_{0p}^-)^2}{(E_{0p}^+)^2} = r_{1p}^2$$


$$\mathfrak{R}_s = \frac{(E_{0s}^-)^2}{(E_{0s}^+)^2} = r_{1s}^2$$
(4.10)

and the transmission coefficients or transmittances are

$$\mathfrak{T}_s = \frac{n_1 \cos\theta_1 (E_{1s}^+)^2}{n_0 \cos\theta_0 (E_{0s}^+)^2} = \frac{n_1 \cos\theta_1}{n_0 \cos\theta_0} t_{1s}^2$$

$$\mathfrak{T}_p = \frac{n_1 \cos\theta_1 (E_{1p}^+)^2}{n_0 \cos\theta_0 (E_{0p}^+)^2} = \frac{n_1 \cos\theta_1}{n_0 \cos\theta_0} t_{1p}^2$$
(4.11)

Expressed in terms of refractive indices for *normal incidence* on an isotropic medium the reflection and transmission coefficients can be written as



$$\mathfrak{R}_p = \mathfrak{R}_s = \left| \frac{n_0 - n_1}{n_0 + n_1} \right|^2$$
(4.12)

and

$$\mathfrak{T}_p = \mathfrak{T}_s = \frac{4n_0 n_1}{(n_0 + n_1)^2}$$
(4.13)

provided that n_0 and n_1 are real.

Among the methods developed for calculating the optical properties of multilayers the most powerful is the matrix method⁵. Application of the boundary conditions requiring that the tangential components of **E** and **H** be continuous across any boundary to the equations of wave propagation at the interface between the $(m-1)$ -th and m -th layers, gives

$$\begin{aligned} E_{m-1}^+ &= \frac{1}{t_m} [E_m^+ \exp(i\delta_m) + r_m E_m^- \exp(-i\delta_m)] \\ E_{m-1}^- &= \frac{1}{t_m} [r_m E_m^+ \exp(i\delta_m) + E_m^- \exp(-i\delta_m)] \end{aligned} \quad (4.14)$$

An alternative recurrence relation may be obtained by using Equations (4.1), namely

$$\begin{pmatrix} E_{m-1} \\ H_{m-1} \end{pmatrix} = \begin{bmatrix} \cos\delta_m & \frac{i}{\eta_m \sin\delta_m} \\ i\eta_m \sin\delta_m & \cos\delta_m \end{bmatrix} \begin{pmatrix} E_m \\ H_m \end{pmatrix} \quad (4.15)$$

Thus, for the L -layer sequence of the films

$$\begin{pmatrix} E_0 \\ H_0 \end{pmatrix} = \prod_{m=1}^L M_m \begin{pmatrix} E_L \\ H_L \end{pmatrix} \quad (4.16)$$

where

$$M_m = \begin{bmatrix} \cos\delta_m & \frac{i}{\eta_m} \sin\delta_m \\ i\eta_m \sin\delta_m & \cos\delta_m \end{bmatrix} \quad (4.17)$$

and

$$\begin{pmatrix} E_L \\ H_L \end{pmatrix} = \begin{pmatrix} 1 \\ \eta_{substr} \end{pmatrix} E^+_{substr} \quad (4.18)$$

The matrix in Equation (4.15) is characteristic of one layer only and has unity determinant, thus, providing a check on the calculations. Equations (4.15) to (4.18) form a basis for almost all thin film calculations and will be used throughout all our work for analysis of the reflectance of any refractive index profile by dividing it into many sub-layers.



4.3 Inhomogeneous optical coatings. Design techniques

Optical coatings possessing graded refractive index profiles have many potential applications in optoelectronics, optics, photonics and photovoltaics. Typical applications include broad- and narrow-band filters, rugate filters, suppression of high-order reflection or transmission bands in multilayer structures, beamsplitters, antireflection coatings, etc.⁸. Amongst the above-mentioned applications, rugate filters are especially important

and roused considerable interest as a highly challenging problem, both theoretically and experimentally⁷⁻³¹.

The design of optical coatings with inhomogeneous refractive index profiles can be performed in several ways⁶. The utilization of a numerical approach suggests the division of the entire starting profile into many sub-layers with thicknesses much less than a wavelength in the range of interest and with homogeneous refractive indices. Optimization of the film is performed using the matrix method with a merit function chosen according to desired specifications. This numerical technique, in principle, does not require close correspondence of the starting profile to the target profile. A good choice of the starting design can, however, save time during refinement.

The analytical approach is founded on the correspondence between the refractive index profile and the spectral transmittance T (or reflectance R) curve. It is based on a Fourier transform relationship between the real refractive index n and a function of transmittance Q . The form of this function is, up to now, not known exactly. The Fourier transform relation as introduced by Delano³² was used by Sossi and Kard³³⁻³⁵ to obtain the following approximate expression:

$$\int_{-\infty}^{+\infty} \frac{dn}{dx} \frac{1}{2n} \exp(i 2\pi wx) dx = Q(w) \exp(i\phi(w)) \quad (4.19)$$

where w is the wave number ($w=1/\lambda$). The variable x is double the optical path length and defined as

$$x = 2 \int_0^z n(u) \cdot du \quad (4.20)$$

where z is the coordinate within the layer with the origin placed at the geometrical centre of the inhomogeneous layer. Several types of Q -functions were constructed^{7,19}:

$$Q_1(T) = \sqrt{\frac{1}{2} \left(\frac{1}{T} - T \right)}$$

$$Q_2(T) = \sqrt{1-T} = \sqrt{R}$$

$$Q_3(T) = \sqrt{\frac{1}{T} - 1} = \sqrt{\frac{R}{T}}$$

$$Q_4(T) = \ln \left(\gamma + \sqrt{(\gamma-1)(\gamma+1)} \right), \quad \text{where } \gamma = 1 + \frac{1}{4} \left(\frac{1}{T} - T \right)$$

$$Q_5(T) = \chi Q_2 + (1-\chi) Q_3, \quad \text{where } 0 \leq \chi \leq 1$$

$$Q_6(T) = \sqrt{-\ln(T)}$$

$$Q_7(T) = \frac{1}{2} \ln \left(\frac{1+\sqrt{R}}{1-\sqrt{R}} \right)$$

$$Q_8(T) = \sqrt{\frac{1}{\sqrt{T}} - \sqrt{T}}$$

(4.21)

The choice of Q-function for a specific case depends on the required filter characteristics. Another important parameter in Equation (4.19) is the phase factor $\phi(w)$. Whereas it is possible to set ϕ to zero, it is more practical^{7,36,37} to define empirically a continuously varying phase factor, for instance³⁶

$$\phi(w) = c_1 w \sin(h_1 w) \quad (4.22)$$

where c_1 and h_1 are constants to be chosen for best performance, or¹²

$$\phi(w) = \frac{\pi w}{w_{\min} + w_{\max}} - \frac{\pi}{2} \sin \left(K \pi \frac{w - w_{\min}}{w_{\max} - w_{\min}} \right) \quad (4.23)$$

where K = is a real number (typically $1 \leq K \leq 5$),

w_{\min} and w_{\max} = wave numbers between which integration of Equation (4.24) is performed.

The use of a non-zero phase factor results in a reduction of refractive index modulation and a more effective utilization of the optical thickness.

Fourier transformation of Equation (4.19) and integration with respect to x yield³⁶

$$n(x) = \exp \left(\frac{2}{\pi} \int_0^{\infty} \frac{Q(w)}{w} \sin(\phi(w) - wx) dw \right) \quad (4.24)$$

The integration should be carried out only over the wave number interval in which the desired spectral transmittance values differs from unity. We will illustrate the Fourier transform design technique by synthesizing a beamsplitter by four variations of the basic algorithm.

Analytical Fourier transform technique: In the most simple cases one can use the properties of the Fourier transform relationship between refractive index profile and reflectance and knowledge of analytical Fourier transform pairs³⁸. Tables, containing numerous examples are readily available⁴⁰. One has to choose a Fourier transform pair with a shape closest to the desired Q-function and then find proper constants to fit the analytical solution to the problem. As an example of this analytical procedure we will design an in-line beamsplitter for fibre optic applications. The filter can be deposited onto the end face of the fibre before splicing and, thus, will be surrounded by identical media with refractive indices of 1.5. The most frequently used wavelengths in fibre optic communication are 1300 nm and 1550 nm. So, we can define a rectangular transmission function with the transmittance equal to 50 per cent between wavelengths $\lambda_1 = 900$ and $\lambda_2 = 2100$ nm as shown by the dashed line in Figure 4.7. The Q-function is chosen to be of the type Q_1 and is given by

$$Q(w) = \frac{C_1}{2\Delta w} \left[\Pi \left(\frac{w+w_0}{\Delta w} \right) + \Pi \left(\frac{w-w_0}{\Delta w} \right) \right] \quad (4.25)$$

where w = wave number,
 w_0 = central wave number of a reflection band,
 Δw = width of the reflection band in wave number space, and
 C_1 = constant.

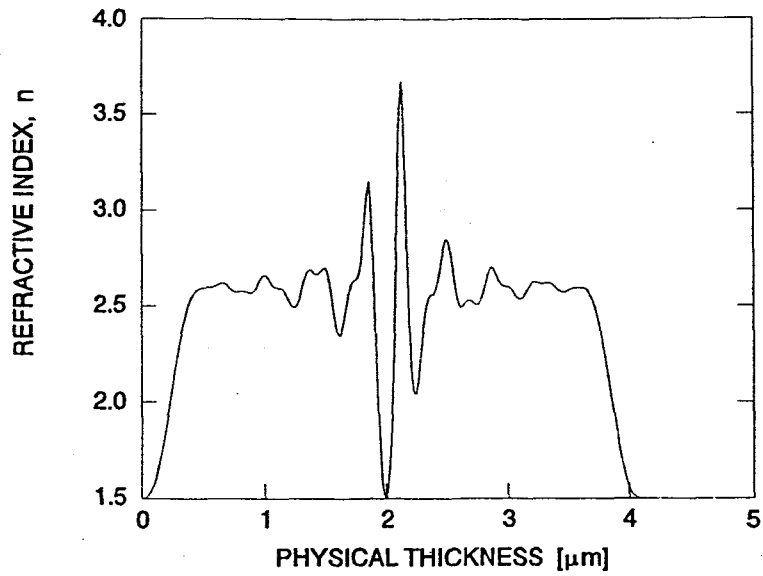


Figure 4.6: Refractive index profile of an inhomogeneous beamsplitter designed by the analytical Fourier transform method

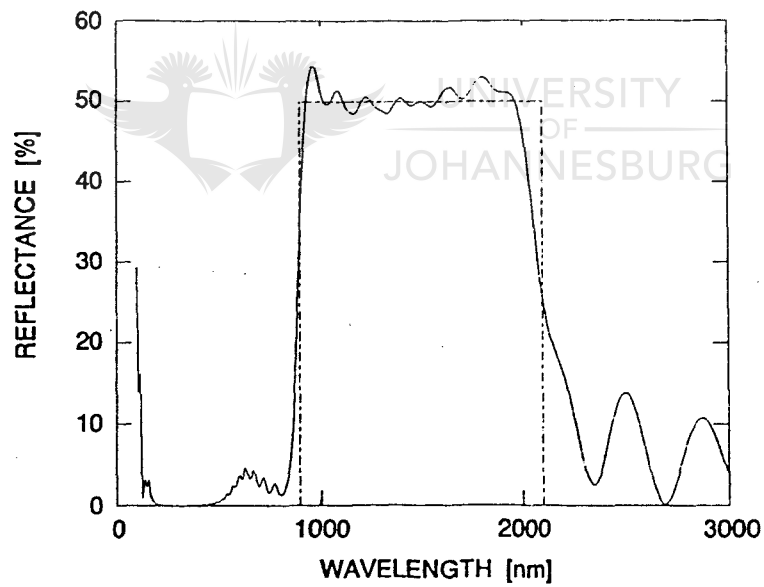


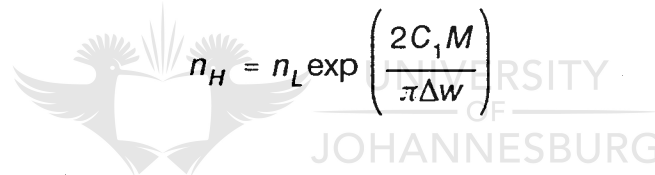
Figure 4.7: Target and computed reflectance of the beamsplitter designed by the analytical Fourier transform method

The function Π is defined by

$$\Pi \left(\frac{w-w_0}{\Delta w} \right) = 1 \quad \text{for} \quad w_0 - \frac{\Delta w}{2} \leq w \leq w_0 + \frac{\Delta w}{2} \quad (4.26)$$

$$= 0 \quad \text{elsewhere}$$

The value of the constant C_1 can be calculated from the required value of peak transmittance³⁸. In our case $C_1 = 5.5 \cdot 10^{-4}$. To construct a refractive index profile for such a filter one needs to specify one of the limiting values of refractive index. It is more convenient to specify the lowest refractive index, n_L . In this example it is the index of the surrounding media and equals 1.5. The highest refractive index n_H can now be calculated from³⁸:



$$n_H = n_L \exp \left(\frac{2C_1 M}{\pi \Delta w} \right) \quad (4.27)$$

where M is the maximum of the quantity $[S_i(y_2) - S_i(y_1)]$, which will be described below.

The refractive index profile for a beamsplitter is then given by³⁸

$$n(x) = \exp \left(\frac{C_1}{\pi \Delta w} (S_i(y_1) - S_i(y_2)) \right) \exp(C_2) \quad (4.28)$$

where constant $C_2 = \ln(n_H \cdot n_L)^{1/2}$. $S_i(y_2)$ and $S_i(y_1)$ are sine integral functions, where

variables y_1 and y_2 are given by

$$y_1 = \frac{2\pi x}{\lambda_1} \quad y_2 = \frac{2\pi x}{\lambda_2} \quad (4.29)$$

The refractive index profile is shown in Figure 4.6. It was calculated according to Equation (4.28), apodized by a Kaiser window with $\theta_k = 3$, and quintic matching layers added for sidelobe and ripple suppression (details will be provided later in this chapter). Reflectance was calculated using the matrix method. The inhomogeneous refractive index profile was divided into 10 nm thick layers of homogeneous refractive index.

Numerical Fourier transform technique: Design of a beamsplitter was repeated using numerical integration of Equation (4.24). The same parameters for bandwidth and height of the reflection band were used, as well as the same quintic matching layers and windowing. Phase factors were set at 0. The calculated refractive index profile is depicted in Figure 4.8. It closely resembles the profile shown in Figure 4.6. However, the length is about 15 per cent larger and the maximum refractive index is slightly (approximately 0.15) lower. The reflectance spectrum of the design is shown by the full curve, whereas the target performance is shown by the dashed line in Figure 4.9. The reflectance spectra for the analytical and numerical designs are very similar in shape as was expected.

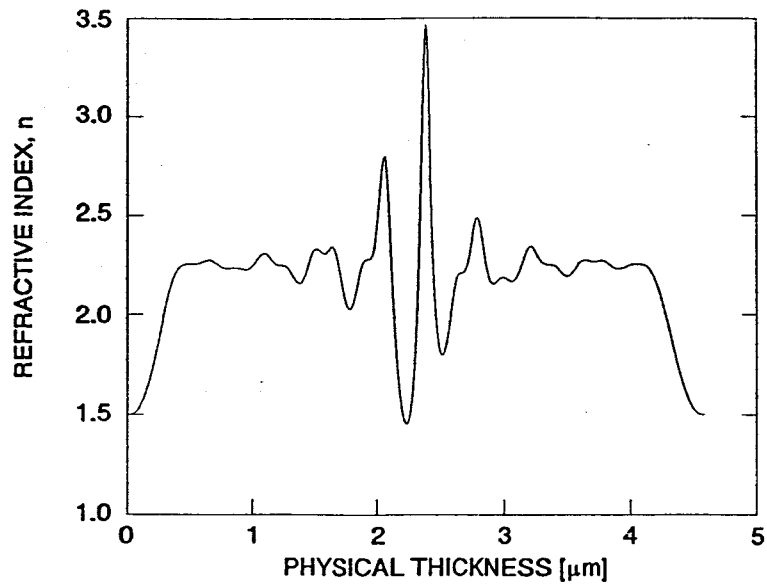


Figure 4.8: Refractive index profile of an inhomogeneous beamsplitter designed by the numerical Fourier transform method

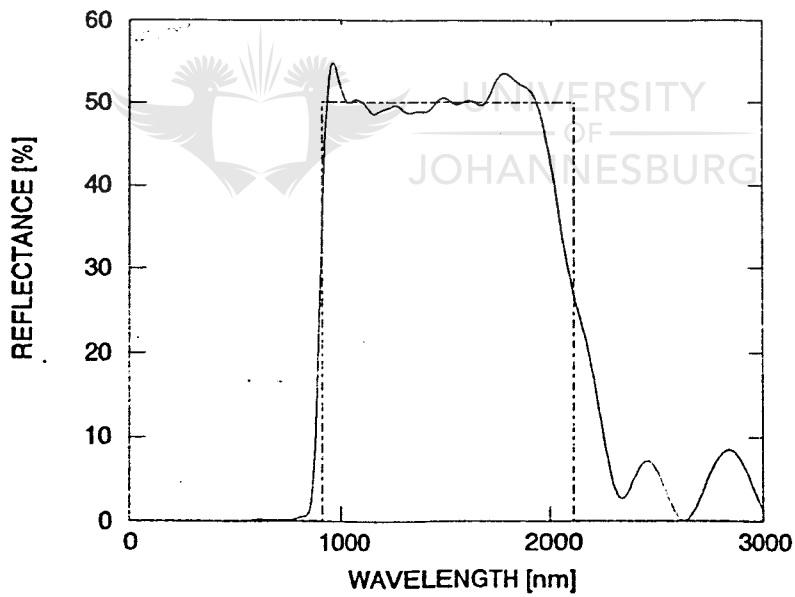


Figure 4.9: Target and computed reflectance of the beamsplitter designed by the numerical Fourier transform method

Numerical Fourier transform technique with successive approximation: One can see that major variations of refractive index are placed in the centre of the refractive index profiles. The maximum values of refractive index, required according to the design, do not exist in SiO_xN_y alloys. To bypass this obstacle of the Fourier transform design technique we will use the continuously varying phase function¹² as suggested by Equation (4.23). Using a non-zero phase factor and successive approximations following re-calculation of the Q-function after determination (by the matrix method) of the reflectance corresponding to the refractive index profile which was obtained after numerical integration of Equation (4.24), we can modify the Q-function according to^{12,36}

$$Q(w)_j = Q(w)_{j-1} + [Q(w)_0 - Q(w)_{j-1}^{\text{new}}] \quad (4.30)$$

where

- $Q(w)_j$ = value of the Q-function on the j -th step of iteration,
- $Q(w)_{j-1}$ = value of the Q-function on the $(j-1)$ -th step of iteration,
- $Q(w)_{j-1}^{\text{new}}$ = new value of the Q-function after calculation of reflection of the structure obtained by integration of Equation (4.24) on the $(j-1)$ -th step, and
- $Q(w)_0$ = value of the target Q-function.

Note that it is necessary to set $Q(w)_j$ equal to zero, if $Q(w)_j$ is negative as calculated by Equation (4.30). That will also allow us not only to bring refractive index inside reasonable range, but also allow better matching of the splitter proper to surrounding media. Using the same parameters as in previous examples and $K = 1.5$ we obtained the refractive index profile and reflectance as shown in Figures 4.10 and 4.11, respectively, after 5 iterations.

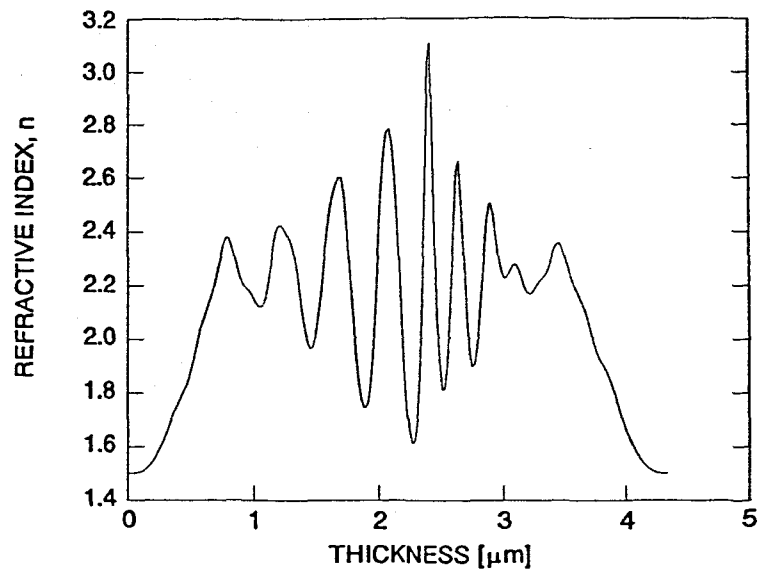


Figure 4.10: Refractive index profile of a beamsplitter designed by the numerical Fourier transform method with non-zero phase factor and successive approximation

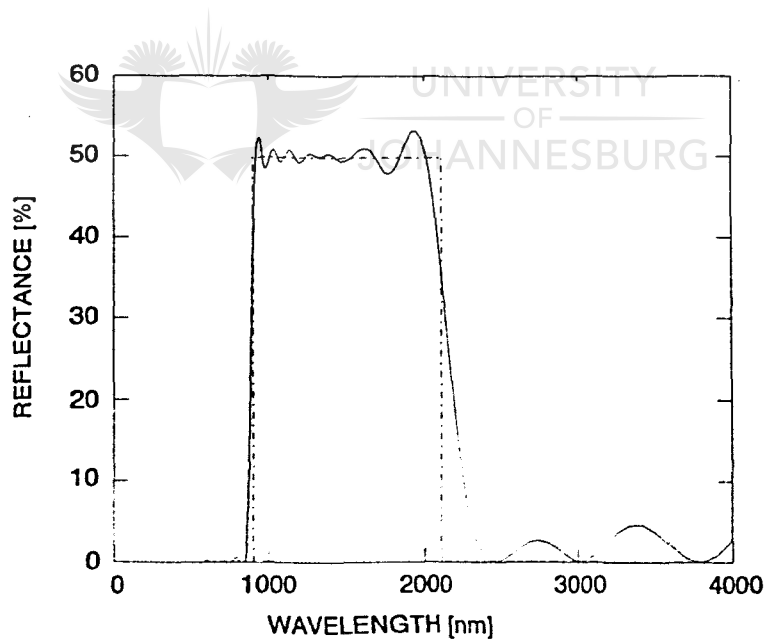


Figure 4.11: Target and computed reflectance of the beamsplitter

One can see that the refractive index range is considerably lowered and it is spread more uniformly throughout the thickness. It is clear that numerical refinement is necessary and, if used with the Fourier transform technique, makes design much more practical.

Numerical Fourier transform technique with corrected target function and successive approximation: Further improvement can be obtained by initial correction of the target performance. It is described in details in the published work¹² and consists of adjustments of the points on the starting transmission curve using representation of every reflectance point by the maximum reflectance value of the elementary rugate filter with a pure sinusoidal refractive index profile. Respective formulae were obtained by Southwell¹¹ on the basis of coupled-wave theory. Successive approximation of the corrected transfer function brings the spectral response closer to the required target performance. The next correction can be performed after the solution of Equation (4.30) becomes stable. In Figures 4.12 and 4.13, respectively, we present results of the implementation of the initial correction technique coupled with successive approximation of the new target performance. It is observed that in the wavelength range of interest the ripple on the reflection curve almost disappeared.

Despite all efforts made in this field, the Fourier transform technique works well only when absorption in the layers and dispersion of the refractive index can be neglected^{12,36}. Another obvious limitation is a difficulty to account for an inevitable refractive index step between air and the filter, and the possible step between the filter and the substrate.

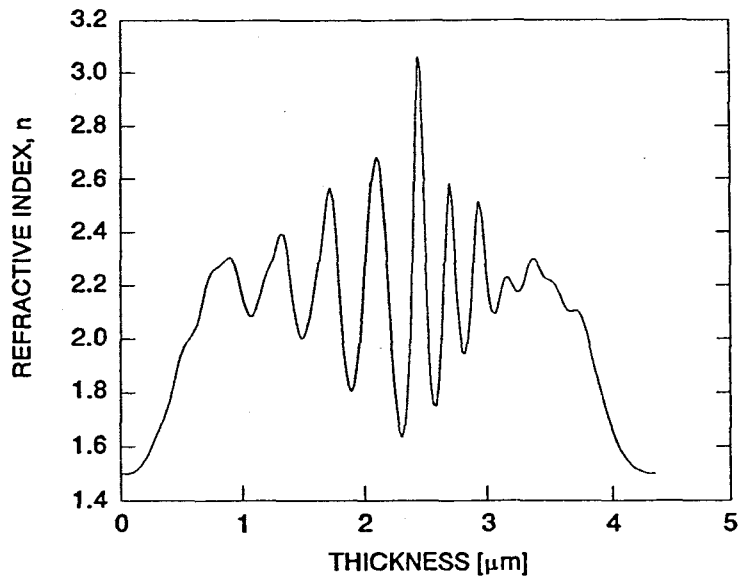


Figure 4.12: Refractive index profile of an inhomogeneous beamsplitter designed by the numerical Fourier transform method with non-zero phase factor, modified target function and successive approximation

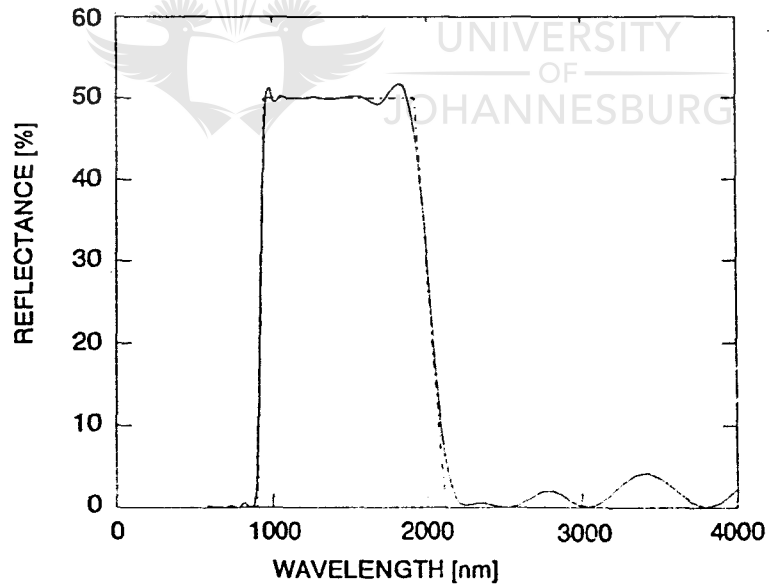


Figure 4.13: Target and computed reflectance of the beamsplitter

Because the main topics of my research are the deposition technique and properties and applications of inhomogeneous SiO_xN_y thin films, we decided to use a simple and effective design procedure developed by Southwell^{13-16,39} for one special case of inhomogeneous refractive index filters, namely sinusoidal or *rugate*. Due to the ability of this design technique to easily take into account dispersion of the refractive index and absorption in the layers, as well as refractive index mismatch between the media, we used it for design of all our rugate structures.

As it was mentioned already, the physical principle of the rugate filter is based on "Bragg-like" interference effects due to periodic variations in the refractive index of the medium and is of particular interest because of its ability to suppress harmonics of the desired stopband. Filters of this type show high reflectivity at a wavelength λ_0 equal to twice the optical period of the refractive index modulation⁸:

$$\lambda_0 = 2n_A P \tag{4.31}$$

where n_A = the average refractive index of one cycle, and

P = the period of modulation.

The refractive index profile for a such filter is given by

$$n(x) = n_A + \frac{1}{2} n_P \sin\left(\frac{2\pi x}{P} + \phi\right) \quad (4.32)$$

where x = the depth coordinate,
 n_P = the peak-to-valley excursion of the sinusoidal refractive index variation, and
 ϕ = phase factor that can be adjusted for optimizing the shape of the filter stopband.

One can have several reflection bands simply by adding more sinusoids of appropriate period to the profile (in this case care should be taken to insure that refractive index values lie in the feasible range):

$$n(x) = n_A + \frac{1}{2} \sum_{j=1}^{N_b} n_{P_j} \sin\left(\frac{2\pi x}{P_j} + \phi_j\right) \quad (4.33)$$

where N_b is the number of reflection bands in the spectrum.

The bandwidth $\Delta\lambda$ is determined by the excursion of the refractive index according to¹⁵:

$$\frac{\Delta\lambda}{\lambda_0} = \frac{n_P}{2n_A} \quad (4.34)$$

The simple rugate filter realized by the refractive index profile given by Equation (4.32) tends to have high sidelobes outside the stopband. This deficiency can, however, be improved significantly by the use of apodization functions or windowing, as shown by

Southwell¹⁵. Further improvement in the filter characteristics is effected by using appropriate matching layers between the substrate and rugate filter, and between the rugate filter and the surrounding media. As, for instance, it was shown by Southwell that quintic matching layers (fifth-order polynomial with coefficients such that first and second derivatives are zero at $x = 0$ and at $x = d_q$) produced excellent results¹³:

$$n_q(x) = n_L + (n_H - n_L) \left[10 \left(\frac{x}{d_q} \right)^3 - 15 \left(\frac{x}{d_q} \right)^4 + 6 \left(\frac{x}{d_q} \right)^5 \right] \quad (4.35)$$

In this instance the profile can be expressed by³¹:

$$n(x) = n_A(x) + \frac{1}{2} \sum_{j=1}^N W_j(x) n_{P_j} \sin \left(\frac{2\pi x}{P_j(x)} + \phi_j \right) \quad (4.36)$$

- where $W_j(x)$ = the window function for the j -th sinusoid,
 $n_A(x)$ = the moving average value of the refractive index profile including the two matching layers, and
 $P_j(x)$ = the period of the j -th sinusoid, taking into account the variation of the average refractive index resulting from the matching layers.

Several kinds of window functions were examined (namely Gaussian, Hamming, Hanning, Blackman and Nuttall)⁴⁰, but the Kaiser window was found to be the best suited to rugate filter design applications. The Kaiser windows are that family of flexible window functions that can be described by the following equation⁴⁰

$$W(x) = \frac{I_0 \left[\theta_k \sqrt{1 - \left(\frac{2x}{d} \right)^2} \right]}{I_0(\theta_k)}, \quad \text{for } |x| \leq \frac{d}{2} \quad (4.37)$$

where I_0 = the modified Bessel function of the first kind and of order zero,
 θ_k = a parameter,
 d = total thickness of the filter subjected to apodization, and
 x = depth coordinate.

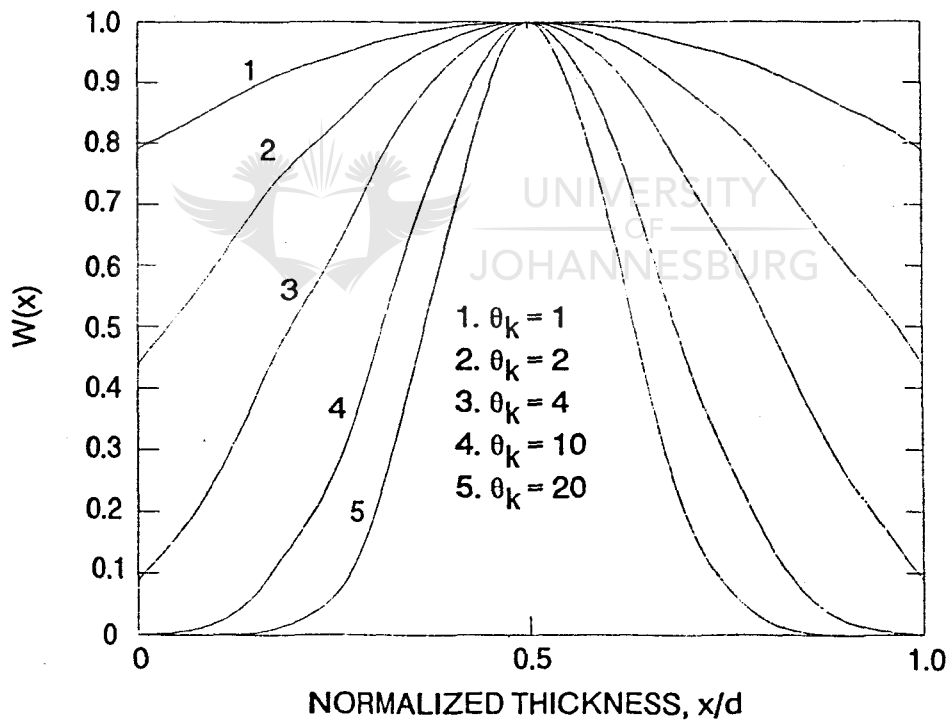


Figure 4.14: A family of Kaiser window functions

By varying the parameter θ_k , the trade-off between the main lobe width and the side lobe level of the Fourier transform of $W(x)$ can be adjusted. Large values of θ_k correspond to wider main lobe width and smaller side lobe levels. Several Kaiser windows with different values of parameter θ_k are shown in Figure 4.14.

Figures 4.15 to 4.17 demonstrate how apodization by a Kaiser window with $\theta_k = 6$ and the introduction of a quintic matching layer transform reflection spectra of a rugate optical filter. All three filters are 30-period rugate filters on glass (with $n_{\text{substr}} = 1.5$) designed for a central wavelength of 1200 nm. These filters have a maximum peak-to-valley excursion of refractive index $n_p = 0.6$ and an average refractive index in the filter proper $n_A = 2$.

Figure 4.15 shows the refractive index profile and corresponding reflectance spectrum for the rugate filter without apodization and matching layers. One can notice large fluctuations in the reflectance on both sides of the stopband.

In the next design apodization by a Kaiser window function with adjustable parameter $\theta_k = 6$ for suppression of sidelobes is imposed on the refractive index profile. The refractive index profile and reflectance spectrum for this filter are shown in Figure 4.16. The height of the sidelobes near the stopband is decreased (in comparison with the previous design) to the same level as that of the ripple far from the stopband. However, the optical density of the filter is also decreased significantly, owing to the decrease in the average refractive index modulation.

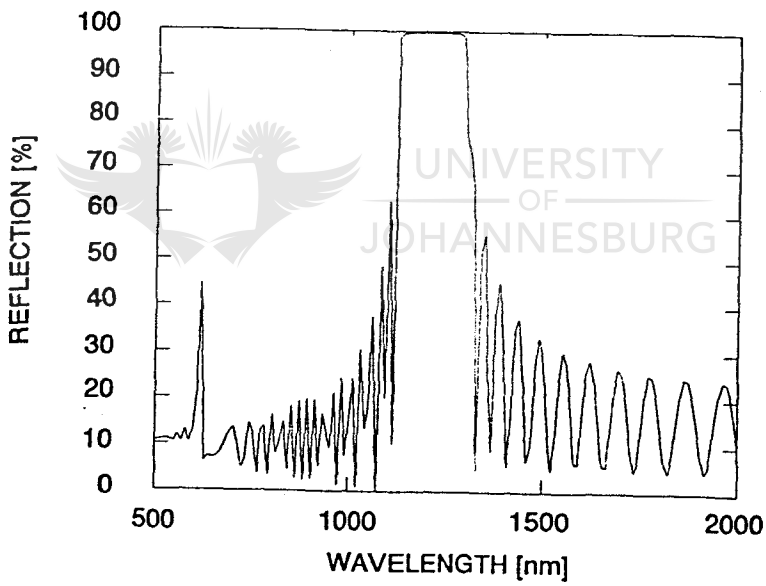
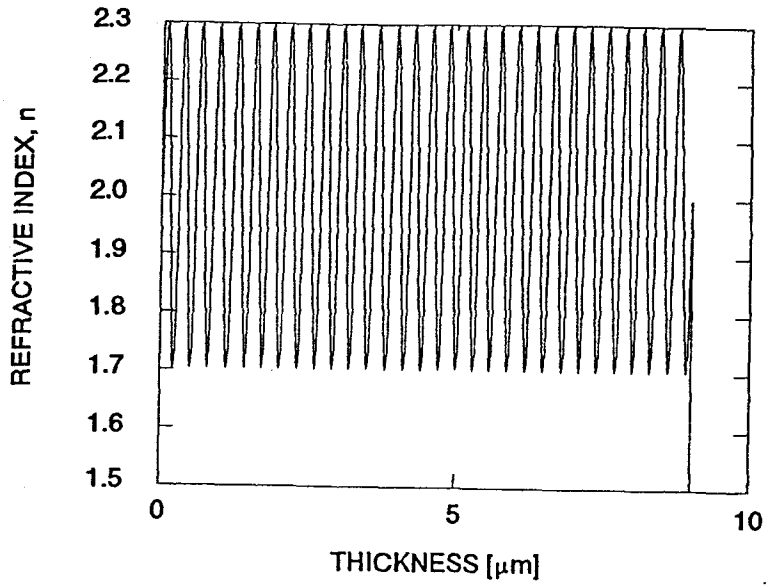


Figure 4.15: The refractive index profile and the corresponding reflectance pattern for a 30-period rugate filter without apodization and matching layers

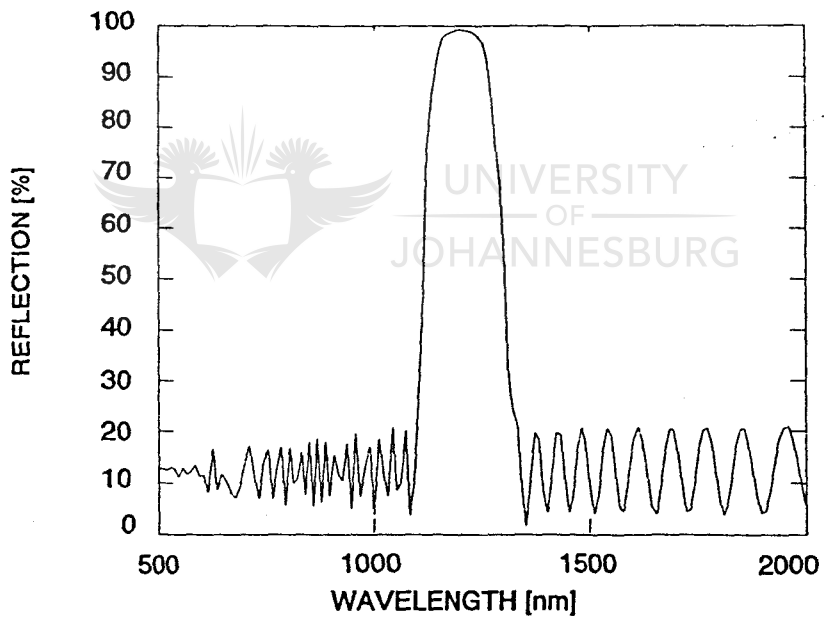
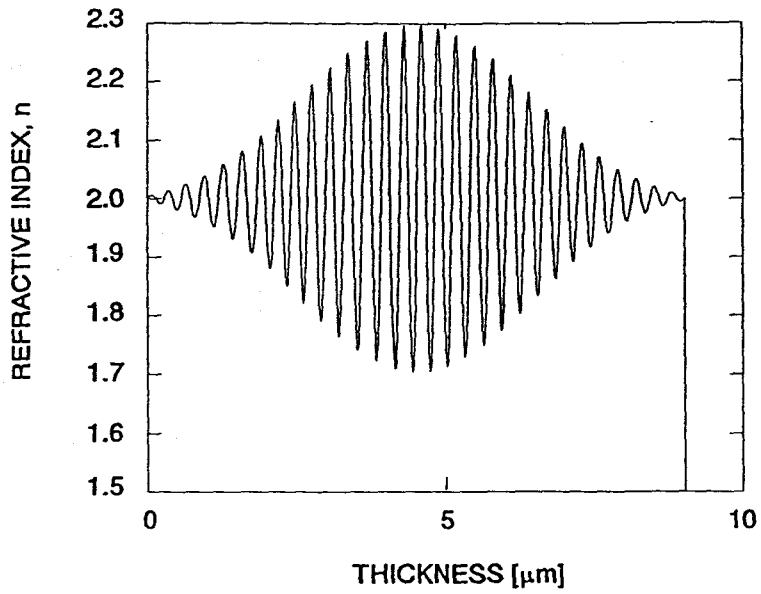


Figure 4.16: The refractive index profile and the corresponding reflectance pattern for a 30-period rugate filter with Kaiser apodization ($\theta_k=6$)

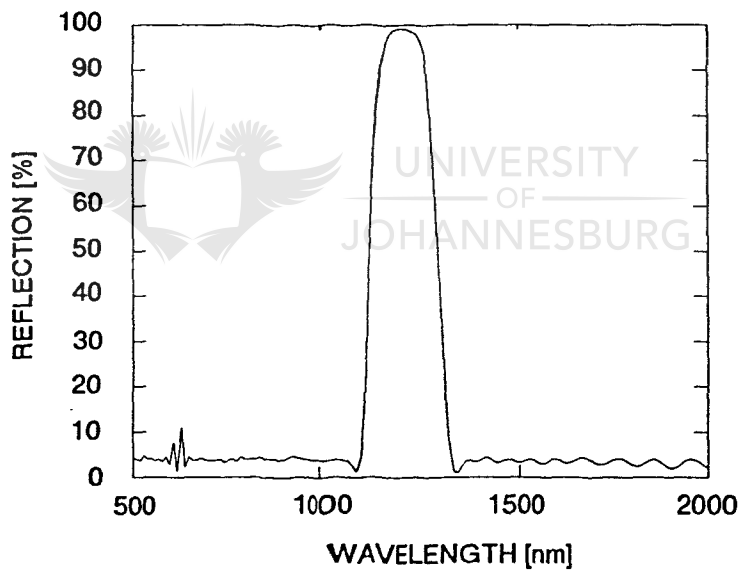
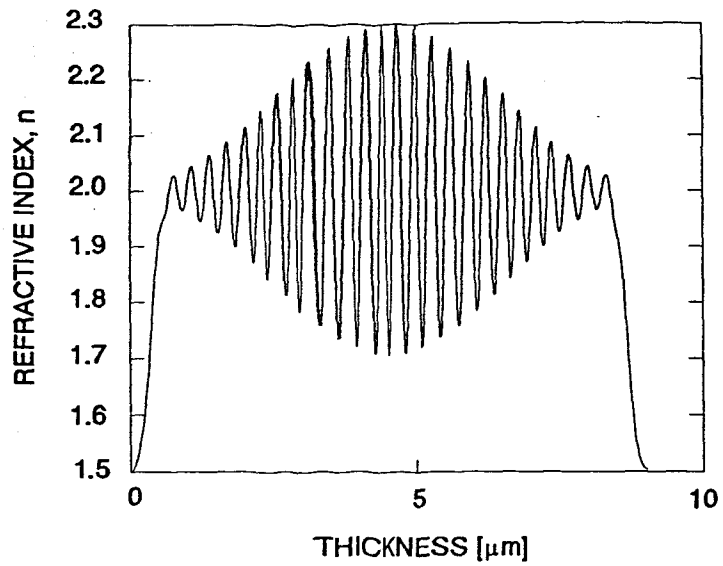


Figure 4.17: The refractive index profile and the corresponding reflectance pattern for a 30-period rugate filter with Kaiser apodization and quintic matching layers

The next step is the introduction of rugated quintic matching layers between the filter and surrounding media at the expense of the first two and a half cycles and the last two and a half cycles of the rugate structure, so the total thickness in terms of number of periods remains the same. The refractive index profile and reflectance of the filter are shown in Figure 4.17. In comparison with the previous design, the ripple is eliminated from the spectrum, while the optical density did not change noticeably. In practice, however, the trade-off is inevitable between thickness, optical density, height of the sidelobes and level of the ripple.



4.4 Conclusions

The Fourier transform technique is a powerful method for the design of optical interference coatings possessing inhomogeneous refractive index profiles. This synthesis technique, based on approximate representation of the exact Fourier transform relationship between refractive index and optical transfer function of the film is fast, reliable and, if dispersion of the refractive index and absorption are negligible, very practical.

In the process of successive approximations of the Q-function, use of a non-zero phase factor and correction of target transfer curve allow for flexible control over refractive index modulations and resulting performance of the synthesized optical coating.

In the case where the role of dispersion in complex refractive index is more significant, a technique based on a simple sinusoidal periodicity is more suitable. For the special case of high-reflectance rugate filters, it permits flexible use of window functions for sidelobe suppression, and matching of filters with the surrounding media employing quintic layers, for instance. Wavelength dependent refractive index steps between surrounding media and optical coatings can easily be taken into account with this procedure.

Design examples presented in this chapter show that the design of inhomogeneous refractive index structures can be performed in several ways, and the most practical one should be determined from the manufacturing technology point of view.

REFERENCES FOR CHAPTER 4

1. A. Thelen, Design of Optical Interference Coatings, McGraw-Hill, Inc., New York, 1989.
2. H.A. Macleod, Thin Film Optical Filters, 2nd ed., Adam Hilger Ltd., Bristol, 1986.
3. R. Jacobson, "Light reflection from films of continuously varying refractive index", in Progress in Optics, Vol. 5 (Editor E. Wolf), North-Holland Publishing, Amsterdam, 1966, pp. 247-286.
4. H.M. Liddel, Computer-Aided Techniques for the Design of Multilayer Filters, Adam Hilger Ltd, Bristol, 1981.
5. O.S. Heavens and R.W. Ditchburn, Insight Into Optics, John Wiley & Sons, Inc., Chichester, 1991.
6. L. Li and J.A. Dobrowolski, "Computation speeds of different optical thin-film synthesis methods", Applied Optics, Vol. 31, No. 19, 1992, pp. 3790-3799.
7. P.G. Verly, J.A. Dobrowolski, W.J. Wild, and R.L. Burton, "Synthesis of high rejection filters with the Fourier transform method", Applied Optics, Vol. 28, No. 14, 1989, pp. 2864-2875.
8. R. Overend, D.R. Gibson, R. Marshall, and K. Lewis, "Rugate filter fabrication using neutral cluster beam deposition", Vacuum, Vol. 43, No. 1&2, 1992, pp. 51-54.
9. P. Baumeister, "Simulation of a rugate filter via a stepped-index dielectric multilayer", Applied Optics, Vol. 25, No. 16, 1986, pp. 2644-2645.
10. W.H. Southwell, "Use of gradient index for spectral filters", Proceedings of SPIE Vol. 464, Solid State Optical Control Devices, 1984, pp. 110-114.

11. W.H. Southwell, "Spectral response calculations of rugate filters using coupled-wave theory", *Journal of the Optical Society of America*, Vol. 5, No. 9, 1988, pp. 1558-1564.
12. H. Fabricius, "Gradient-index filters: designing filters with steep skirts, high reflection, and quintic matching layers", *Applied Optics*, Vol. 31, No. 25, 1992, pp. 5191-5196
13. W.H. Southwell and R.L. Hall, "Rugate filter sidelobe suppression using quintic and rugated quintic matching layers", *Applied Optics*, Vol. 28, No. 14, 1989, pp. 2949-2951.
14. W.J. Gunning, R.L. Hall, F.J. Woodberry, W.H. Southwell, and N.S. Gluck, "Codeposition of continuous composition rugate filters", *Applied Optics*, Vol. 28, No. 14, 1989, pp. 2945-2948.
15. W.H. Southwell, "Using apodization functions to reduce sidelobes in rugate filters", *Applied Optics*, Vol. 28, No. 23, 1989, pp. 5091-5094.
16. H. Sankur, W. Southwell, R. Hall and W.J. Gunning, "Rugate filter deposition by the OMVPE technique", in Optical Interference Coatings Technical Digest, 1992 (Optical Society of America, Washington, D.C., 1992), Vol. 15, pp. 125-127.
17. B.G. Bovard, "Rugate filter design: the modified Fourier transform technique", *Applied Optics*, Vol. 29, No. 1, 1990, pp. 24-30.
18. B.G. Bovard, "Derivation of a matrix describing a rugate dielectric thin film", *Applied Optics*, Vol. 27, No. 10, 1988, pp. 1998-2005.
19. B.G. Bovard, "Rugate filter theory: an overview", *Applied Optics*, Vol. 32, No. 28, 1993, pp. 5427 - 5442.

20. R.J. Becker and M.K. Kullen, "Inversion of rugate spectra", *Thin Solid Films*, Vol. 181, No. 1&2, 1989, pp. 579-588.
21. F. Villa, R. Machorro, J. Siqueiros, and L.E. Regalado, "Admittance of rugate filters derived from 2×2 inhomogeneous matrix", *Applied Optics*, Vol. 33, No. 13, 1994, pp. 2672 - 2677.
22. C.S. Bartholomew, H.T. Betz, J.L. Grieser, R.A. Spence, and N.R. Murarka, "Rugate filters by laser flash evaporation of Si_xN_y on room temperature polycarbonate", *Proceedings of SPIE*, Vol. 821, *Modelling of Optical Thin Films*, 1987, pp. 198-204.
23. J. Allen, B.D. Herrington, S. Jansen and J.C. Blomfield, "Graded rugate filters for head up displays", in Optical Interference Coatings Technical Digest, 1992 (Optical Society of America, Washington, D.C., 1992), Vol. 15, pp. 134-136.
24. E.P. Donovan, D. Van Vechten, A.D.F. Kahn, C.A. Carosella and G.K. Hubler, "Near infrared rugate filter fabrication by ion beam assisted deposition of $\text{Si}_{(1-x)}\text{N}_x$ films", *Applied Optics*, Vol. 28, No. 14, 1989, pp. 2940-2944.
25. S. Lim, J.H. Ryu, J.F. Wager, and T.K. Plant, "Rugate filters grown by plasma-enhanced chemical vapor deposition", *Thin Solid Films*, Vol. 245, No. 1&2, 1994, pp. 141-145.
26. M.L. Elder, K.S. Jancaitis, D. Milam, and J. H. Campbell, "Optical Characterization of damage resistant "kilolayer" rugate filters", in Laser Induced Damage in Optical Materials: 1989, Lawrence Livermore National Laboratory report UCRL-JC-105036.

27. J. Allen, P.G. Girow, B. Herrington, P. Gee, "Rugate filters for image projection in head-mounted displays", SPIE Proceedings, Vol. 2253, Optical Interference Coatings, 1994, pp. 470-475.
28. B.G. Bovard, "Ion-assisted processing of optical coatings", Thin Solid Films, Vol. 206, No. 1&2, 1991, pp. 224-229.
29. P.V. Bulkin, P.L. Swart and B.M. Lacquet, "Properties and applications of electron cyclotron plasma deposited SiO_xN_y films with graded refractive index profiles", accepted for publication in "Journal of Non-Crystalline Solids".
30. A.G. Greenham, B.A. Nichols, R.M. Wood, N. Nourshargh and K.L. Lewis, "Optical interference filters with continuous refractive index modulations by microwave plasma-assisted chemical vapour deposition", Optical Engineering, Vol. 32, No. 5, 1993, pp. 1018-1023.
31. P.V. Bulkin, P.L. Swart and B.M. Lacquet, "ECR plasma CVD for rugate filters manufacturing", SPIE Proceedings, Vol. 2253, Optical Interference Coatings, 1994, pp. 462-469.
32. E. Delano, "Fourier synthesis of multilayer filters", Journal of Optical Society of America, Vol. 57, No. 12, 1967, pp. 1529-1533.
33. L. Sossi and P. Kard, "On the theory of the reflection and transmission of light by a thin inhomogeneous dielectric film", Eesti NSV Tead. Akad. Toim. Fuus. Mat., Vol. 17, 1968, pp. 41-48.
34. L. Sossi, "A method for the synthesis of multilayer dielectric interference coatings", Eesti NSV Tead. Akad. Toim. Fuus. Mat., Vol. 23, 1974, pp. 223-237.

35. L. Sossi, "On the theory of synthesis of multilayer dielectric light filters", Eesti NSV Tead. Akad. Toim. Fuus. Mat., Vol. 25, 1976, pp. 171-176.
36. J.A. Dobrowolski and D. Lowe, "Optical thin film synthesis program based on the use of Fourier transforms", Applied Optics, Vol. 17, No. 19, 1978, pp. 3039-3050.
37. P.G. Verly and J.A. Dobrowolski, "Iterative correction process for optical thin film synthesis with the Fourier transform method", Applied Optics, Vol. 29, No. 25, 1990, pp. 3672-3684.
38. G. Boivin and D. St.-Germain, "Synthesis of gradient-index profiles corresponding to spectral reflectance derived by inverse Fourier transform", Applied Optics, 1987, Vol. 26, No. 19, 1987, pp. 4209-4213.
39. W.H. Southwell, R.L. Hall and W.J. Gunning, "Using wavelets to design gradient-index interference coatings", SPIE Proceedings, Vol. 2046, Inhomogeneous and quasi-inhomogeneous optical coatings, 1993, pp. 46-59.
40. A.V. Oppenheim and R.W. Schaffer, Discrete-Time Signal Processing, Prentice Hall Int., London, 1989.

CHAPTER 5

THE APPLICATION OF GRADED REFRACTIVE INDEX SiO_xN_y LAYERS FOR THE FABRICATION OF OPTICAL COATINGS

5.1 Introduction

The rugate filter, so named after the Latin word *rugosus* (which means "wrinkled"), still poses quite a problem to the modern-day optical coatings manufacturing industry. The fabrication of such complicated structures requires state-of-the-art techniques to gain the necessary process control, thereby preserving the integrity of the refractive index profile. Several techniques for the fabrication of rugate filters were reported in the literature: neutral cluster beam deposition (NCB)¹; microwave plasma assisted deposition (MPACVD)²; ion beam assisted deposition (IBAD)³; organometallic vapour phase epitaxy (OMVPE)⁴; molecular beam deposition⁵; reactive (thermal or electron-beam) evaporation⁶; laser flash evaporation⁷; pulsed plasma deposition⁸; radio frequency (RF) 13.56 MHz plasma enhanced chemical vapour deposition (PECVD)⁹ and microwave 2.45 GHz electron cyclotron resonance plasma enhanced chemical vapour deposition (ECR-PECVD)^{10,11}. Although each of these techniques has its own advantages and disadvantages, the latest technique, in our opinion, probably has the biggest potential.

The sinusoidal modulation can be realized using two approaches, namely a digital and an analogue approach¹. The digital approach achieves the desired refractive index profile by dividing the layer into thin steps of uniform indices (with each index step being divided into a high- and low-index pair with the same equivalent index as the required step). The analogue approach relies upon the continuous grading of the index profile, using materials that form a solid solution, or a stable phase mixture.

Design techniques for these types of filters based either on the simple sinusoidal model^{6,12,13} or on the inverse Fourier transform method¹⁴⁻¹⁷, have already been developed to an advanced stage (it was, however, pointed out already that in the inverse Fourier transform method it is still difficult to accommodate the dispersion of a complex refractive index). Fabrication technology, on the other hand, is still under development. The implementation of sinusoidal modulation of a refractive index, especially with such complications as matching layers and windowing, requires the use of complex materials and deposition techniques with strictly controlled and reproducible parameters.

Neutral cluster beam deposition (NCBD) was used by R Overend et al.¹ to manufacture narrow-band reflection structures for the near infrared at 780 nm. Thin films of BaF₂ and ZnSe were deposited at a rate of 300 to 1200 Å/min under computer control with quartz crystal monitoring. A digitized technique was used in the design procedure. Fabricated rugate filters showed good agreement with the design in the desired stopband and reasonable agreement outside the stopband, but sidelobes reached about 50 per cent. Neutral cluster beam deposition has been shown to provide stable rates of film growth. Compatibility of the technique with a conventional production plant was also shown.

The manufacturing of single- and double-band rugate filters by microwave plasma-assisted chemical vapour deposition (MPACVD) was carried out by AG Greenham et al.². Silicon oxynitride was chosen because of its large refractive index range and continuous series of solid solutions in the $\text{SiO}_2\text{-Si}_3\text{N}_4$ alloy. The precursors used were silicon tetrachloride, oxygen and nitrogen, with argon used as a carrier gas for SiCl_4 . Microwave power of 1 kW at 2.45 GHz was used for sustaining the plasma at 1 mbar of working pressure. Gas supplies to the chamber were controlled by precision mass flow controllers (MFC) operated by computer for creating true sinusoidal modulation of the refractive index. The deposition rate was in the range of 600 to 1200 Å/sec. MPACVD has been successfully applied to the fabrication of continuously modulated refractive index dielectric interference filters of rugate design. Maximum reflectivity obtained was in excess of 99.95 per cent and uniformity of a few per cent has been achieved over 38-mm-diameter substrates.



UNIVERSITY
OF
JOHANNESBURG

Ion beam assisted deposition of $\text{Si}_{(1-y)}\text{N}_y$ films for rugate filter fabrication was studied by EP Donovan et al.³. In this realization, the electron beam gun was used for evaporation of Si and the ion source provided a beam of ionised nitrogen with energy of 500eV and an extracted current varying from 3 to 40 mA. Feedback from the quartz crystal monitor via the computer provided control over the ion source and hence over the refractive index of growing film, which was varying from 2 to 4 (at 1666 nm). A rugate filter with an optical density of 2.6 at a wavelength of 1150 nm was obtained, showing good

agreement with calculated values. A similar technique was used by BG Bovard¹⁸ for manufacturing an AlO_xN_y rugate filter with a variation in the refractive index from 1.65 to 1.85. Aluminium was evaporated with an electron gun and the substrate was bombarded by a beam of N_2^+ ions in an oxygen-rich atmosphere. Maximum reflectance at about 580 nm reached just below the 60 per cent level.

Organometallic vapour phase epitaxial (OMVPE) growth of rugate structures and graded index antireflection coatings was undertaken by H Sankur et al.⁴. Deposition experiments were done in a vertical-flow atmospheric-pressure OMVPE reactor. Trimethylgallium, trimethylaluminium and arsine were used as precursors. (100) oriented GaAs substrates were used and the deposition temperature was in the range of 750 to 800° C. A digitized approach was adopted in the design. The layer composition was automatically controlled by the relative flow rate of the Al and Ga precursors by the computer in closed-loop control, following the acquisition and analysis of the reflectance data. Several single- and multi-line rugate filters were successfully deposited for use in the mid-infrared (3 to 5 μm) and far-infrared (8 to 12 μm) wavelength range. The wavelength placement accuracy was to within 1 to 2 % for all lines.

The molecular beam deposition (MBD) process, which inherited its equipment ideology from the molecular beam epitaxy (MBE) technique, was also studied for optical thin film manufacturing, and for the fabrication of rugate filters in particular, by K Lewis et al.⁵ and

SP Fisher et al.¹⁹. The digitized approach was once again used in the design, and BaF₂ and PbF₂ were used as base materials. The filter grown by thermal evaporation from Knudsen's cells in the ultra-high vacuum environment had 31 sine periods (186 thin layers). The maximum in reflectance at 420 nm was in excess of 80 per cent, but the reflection peak was split in two, owing to small period errors.

Electron gun evaporation, a rather conventional technique, was used by J Allen et al.^{20,21} for the fabrication of digitized rugate filters under computer control. The deposition of TiO₂ and SiO₂ was carried out in a Leybold 700 QEL box coater, while feedback was provided by the use of twin quartz crystals. Great uniformity (± 1.5 nm on the substrate and ± 2.5 nm in run-to-run trial) over a substrate of 320 mm long by 152 mm wide was achieved.

Laser flash evaporation of SiO_xN_y for single- and double-line rugate filters onto polycarbonate substrates was studied by CS Bartholomew et al.⁷. This technique was chosen by the authors because any possible radiative heating of the substrate was small, and because decomposition and reaction of the source material were minimized. The computer-controlled CO₂ laser was evaporating SiO₂ and Si₃N₄ in impulse regime following a digitized rugate design. The interferometer, quartz crystal monitor and laser detector were continuously measuring the index of refraction, thickness and laser power and were sending these values to the computer, where they were compared to

theoretical values. Error and change of algorithms then drove the CO₂ laser and attenuators to give the proper deposition rates of the two target materials. SiO_xN_y rugate filters with optical densities as high as 2.5 and bandwidth as narrow as 6.8 per cent of the rejection wavelength were fabricated. These filters adhered well to polycarbonate and showed good film quality. All the important parameters were within 10 per cent of the design values.

Pulsed radio frequency (RF) plasma deposition of optical filter structures was reported by K Sheach et al.⁸. In contrast with conventional plasma deposition systems, the pulsed plasma deposition process is based on the use of short (100 to 400 μs) discharge pulses of very high RF power (500 W·cm⁻²). These pulses are thought to be sufficiently energetic to achieve complete dissociation of all the active gases introduced to the reaction chamber. No active heating of the substrate is required to produce a film of high quality, and passive heating of the substrate environment is avoided by a low duty cycle (30 Hz) of the discharge pulses which results in a low average power level. Using the pulsed plasma process, it has been possible to carry out this type of deposition solely by pre-programming of the required filter design with no operator intervention being necessary subsequent to the initiation of the deposition. The reproducibility of filters from run to run has been shown to be within 0.5 per cent under optimum conditions. All filters deposited have used the digitized design.

Another type of plasma impulse CVD with 2.45 GHz microwave activation was reported by M Heming et al.²². This plasma process operates at substrate temperatures below 150° C and thus allows a wide range of materials to be coated. The pulsed microwave excitation of the plasma results in effective gas exchange between pulses, high reaction rates and the efficient use of precursor gases for layer formation. Deposition rates of 9000 Å/min for SiO₂ and 2500 Å/min for TiO₂ have been achieved. The technique allows coating of flat- and dome-shaped substrates if used in appropriate arrangements. The uniformity of layer thickness, which is essential for optical filter performance, has been improved to ± 0.3 per cent on 100 mm flat substrates. Uniformity on dome-shaped substrates was not reported.

High-temperature plasma chemical vapour deposition (PCVD) for the fabrication of rugate filters was reported by ML Elder et al.²³. Damage-resistant optical coatings were prepared at substrate temperatures from 850 to 1100° C and consisted of several thousand periods of fused SiO₂ lightly doped with a glass network modifier or network former (e.g. GeO₂, F) to give an interlayer index variation. The nominal refractive index difference Δn can range from as low as 0.001 to as high as 0.05, depending on the dopant and the dopant concentration. Control of the layer thickness (coatings period) to within a few angstroms is possible at deposition rates of a few micrometers per minute. Peak reflectance for filters manufactured according to this technique was observed to be within 0.5 per cent of the designed wavelength.

PECVD with RF 13.56 MHz plasma also was used for fabrication of graded refractive index layers of silicon oxynitride, and of rugate filters in particular, by S. Lim et al^{9,24}. The process was carried out in a capacitively coupled parallel-plate reactor configuration with the top electrode powered and the bottom electrode grounded and heated. The power density used was approximately $0.165 \text{ W}\cdot\text{cm}^{-2}$, while the chamber pressure and substrate temperature were 0.5 Torr and 300°C , respectively. As precursors, 2.01% SiH_4 in He, nitrogen and 5% N_2O in He were used. Flows of SiH_4 and N_2 were kept constant at 20 and 12 sccm, respectively, while the flow of N_2O was varied from 0 to about 300 sccm. Homogeneous layers of different composition were grown in advance to create a calibration chart. The refractive index range obtained was from 1.46 to 2.05. Rugate filters with 10 and 20 sinusoidal periods were grown on a glass substrate and shown to be in good agreement with simulations, except for some difference in sidelobes.



Remote plasma enhanced chemical vapour deposition (RPECVD) can also be considered as an optical coatings deposition technique. Results by DJ Stephens et al²⁵. on the deposition of Bragg reflectors consisting of $\text{SiO}_2/\text{Si}_3\text{N}_4$ multilayers show promising agreement between the designed and the actual spectra. In spite of the fact that the fabrication of classical multilayer stacks was only performed, the technology seems to be capable of producing inhomogeneous refractive index layers as well.

5.2 ECR-PECVD for the fabrication of inhomogeneous optical coatings

As was illustrated in chapter 3, ECR-PECVD is an effective means for low-temperature deposition of thin films with strict control being exerted over the refractive index and the growth rate. The quality of ECR-PECVD-deposited films is superior, in terms of hydrogen concentration, thermal and chemical stability and packing density, to that of similar composition films obtained according to conventional techniques²⁶⁻²⁸. These are basic requirements for the successful implementation of the technology for the fabrication of inhomogeneous optical coatings.

The first utilization of ECR-PECVD for optical coatings manufacturing dates back to an unpublished corporate report by S Dzioba of Bell-Northern Research Ltd., Canada, in 1989²⁹. ECR-PECVD was used to deposit a Si/SiO_x multilayer dielectric stack on InP for an optical dichroic filter and the possibility to control the refractive index reproducibly and accurately was illustrated. In 1994, S Dzioba and R Rousina reported on ECR-PECVD for the fabrication of quarterwave single-layer antireflection coating made of SiO_xN_y and multilayer stacks of a:Si/SiO_xN_y with abrupt interfaces for dichroic mirrors³⁰.

The first application of ECR-PECVD for the deposition of layers with inhomogeneous refractive index profiles was reported by P Bulkin, P Swart and B Lacquet in 1993³¹. A

rugate filter with reflection of about 80 per cent was fabricated using SiN_x (x varied from 0 to $4/3$). Later, we reported on the fabrication of SiN_x high-reflectance single- and double-band rugate structures by ECR-PECVD with RF substrate biasing and extended the materials range to SiO_xN_y ^{10,11}.

We have used ECR-PECVD for the manufacturing of rugate filters because of the number of distinct features offered by this technology³². It is a low-temperature process, thus allowing deposition of the filters onto temperature-sensitive $\text{A}^{\text{III}}\text{B}^{\text{V}}$ and polymer substrates. As deposition occurs from the gas phase in ECR-PECVD, the continuous changing of the refractive index can readily be achieved by the computer control exerted over the gas flows, and the duration of the process is not limited by the volume of a crucible load. Sharp interfaces can, if required, also be easily obtained with this technology³³, thus allowing us to support both the analogue- and digital-design techniques, as well as classical multilayer stack fabrication³³. The plasma allows for effective pre-deposition cleaning of the substrates, and the low-pressure results in complete suppression of volume reaction, eliminating potential particle inclusions into the growing film. The strong dependence of the refractive index on the gas ratio, the small consumption of reagents and the possibility to grow many different materials coupled with inexpensive microwave hardware, make ECR technology especially suited to the research laboratory environment.

5.3 Rugate filters

Despite the fact that several of the above-mentioned techniques have shown to be able to manufacture such complicated structures as rugate filters, we believe that ECR-PECVD is a versatile and powerful alternative method. We have demonstrated it by several practical examples of filters realized with either continuously graded refractive index profiles, or conventional step-index structures. Rugate filters for one and two reflecting bands were designed, manufactured on silicon and glass substrates, and characterized. An experimental inhomogeneous gaussian antireflection coating on silicon is compared with a three-layer coating. Further evidence of the applicability of ECR-PECVD to the manufacture of step-index structures is provided by the fabrication of an 18-layer quarterwave stack.



On the basis of experimental optical data for SiN_x and SiO_xN_y described in chapter 3, several rugate structures featuring rugated quintic matching layers and Kaiser apodization were designed. The availability of complete data of the optical properties of the SiN_x and SiO_xN_y thin films makes possible the design of optical coatings which takes into account absorption in the layers and dispersion of the refractive index¹¹. Dispersion and absorption in the layers start to play a substantial role only at wavelengths shorter than 700 nm. These effects are not always deleterious but can, for instance, suppress the harmonic reflection peaks¹¹.

5.3.1 Single-band SiN_x rugate filter on silicon

A single-band rugate filter designed for maximum reflectance at a wavelength of 1000 nm, and having a total thickness of 2.1 micron, had a theoretical reflectance of 97.8 per cent in the band. The refractive index profile comprised a Kaiser window for the entire length of the coating, which was superimposed on a rugated quintic transitional matching layer from air to filter and from filter to substrate is shown in Figure 5.1. The average refractive index in the filter proper was chosen to be 2.5, and the maximum peak-to-valley excursion of refractive index $n_p = 1.2$, while the adjustable parameter of the Kaiser window (θ_k) was set at 4.25. Figure 5.2 depicts the required and the actual gas flows recorded during the growth of the single-band filter.

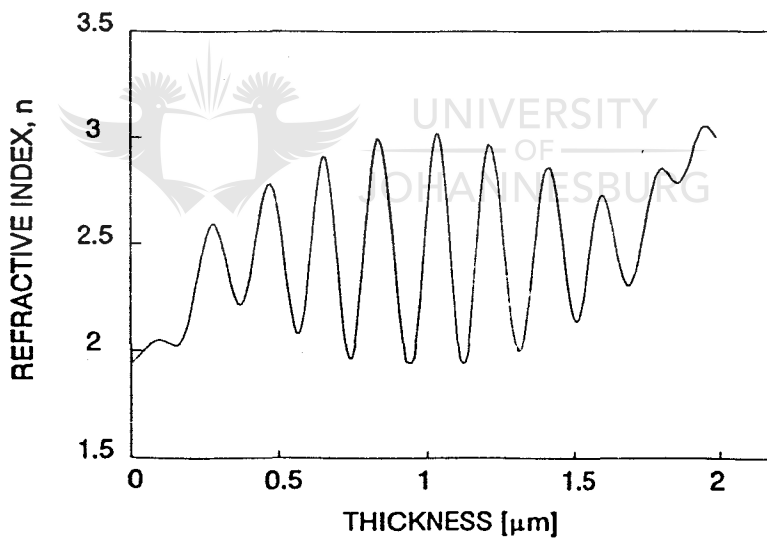


Figure 5.1: Refractive index profile (at wavelength 1000 nm) of a single-band SiN_x rugate filter on silicon.

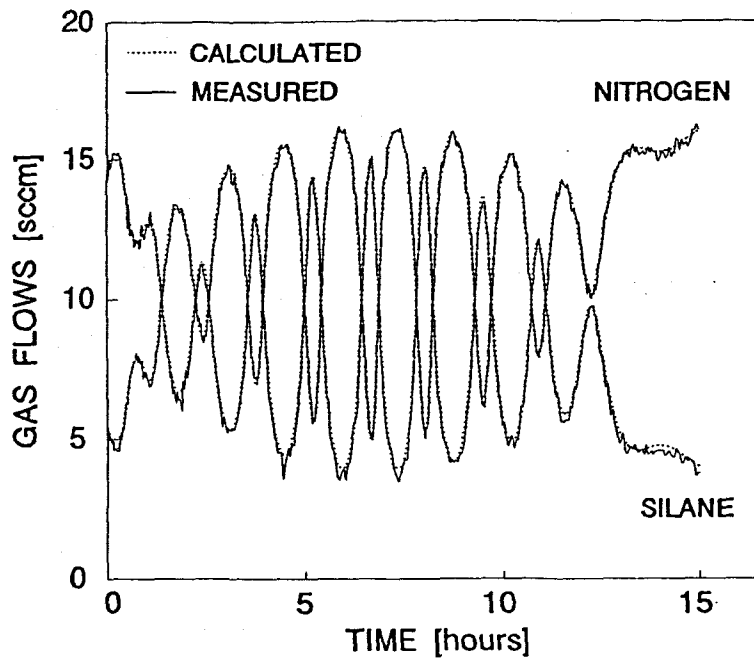


Figure 5.2: Calculated and recorded gas flows during the deposition of a single-band rugate filter.

Figure 5.3 shows the reflectance spectrum of the as-grown single-band rugate filter. The corresponding simulated spectrum is shown by dashed line in the above-mentioned figure. The experimental spectrum had been corrected for non-idealities of the aluminium reference mirror employed in the spectrophotometer (Hitachi U-3400 with a 5° specular reflectance attachment). Agreement between simulated and experimental peak reflectance is within the experimental error of the spectrophotometer, whereas its position is not exactly at the designed value. It appears at 960 nm instead of at 1000 nm. Although the design incorporates apodization and rugated quintic matching layers, the sidelobes of approximately 15 per cent evident in Figure 5.3 could not be fully

suppressed. They are attributed to the wavelength dependent refractive index step between the filter and the media on both sides.

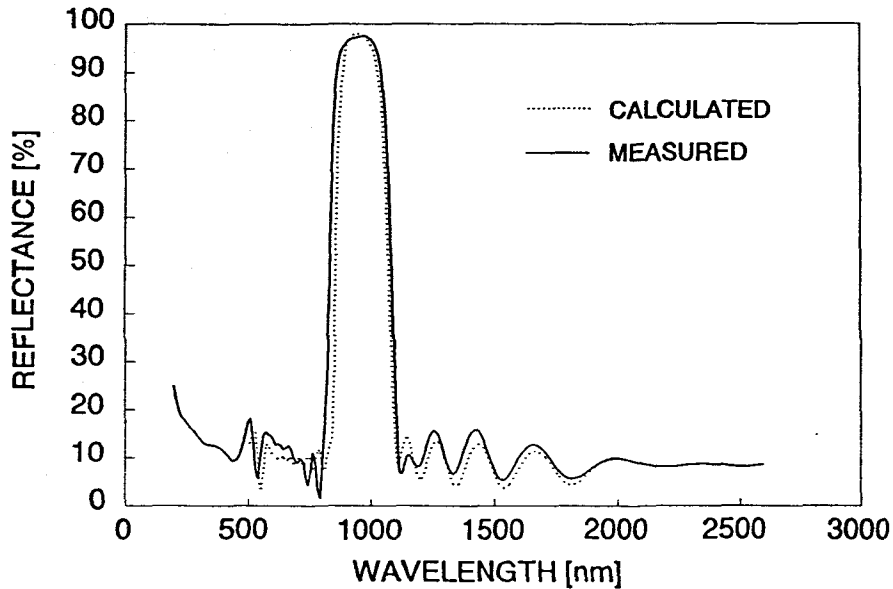


Figure 5.3: Reflectance spectra of a single-band rugate filter on silicon.



The good agreement of the spectra shown in Figure 5.3 has confirmed the high degree of accuracy in the determination of optical constants of the material. The discrepancy between the designed and actual spectra is attributed mainly to fluctuations in self-bias of the substrate, which was not under closed-loop control. The experimental value for full-width-at-half-maximum (FWHM) is approximately 15 per cent larger than expected. It is 240 nm (design value: 215 nm). We ascribe this increase to the slight undershoot of the MFC for silane, as can be seen in Figure 5.2. This will lead to a deeper valley of the refractive index profile, increasing the total excursion of the refractive index.

5.3.2 Double-band SiN_x rugate filter on silicon

A double-band rugate filter with a total thickness of 3.33 micron was designed to have maximum reflectance of 98% in the main band at 1000 nm and a second reflection band at the wavelength given by the ratio 1.3:1. It has a total excursion of refractive index $n_p=1.2$, and also features rugated quintic layers and apodization using a Kaiser window with $\theta_k=3.0$. The refractive index profile of this filter is shown in Figure 5.4. The temporal changes of the gas flows needed during the growth of the double-band filter are shown in Figure. 5.5.

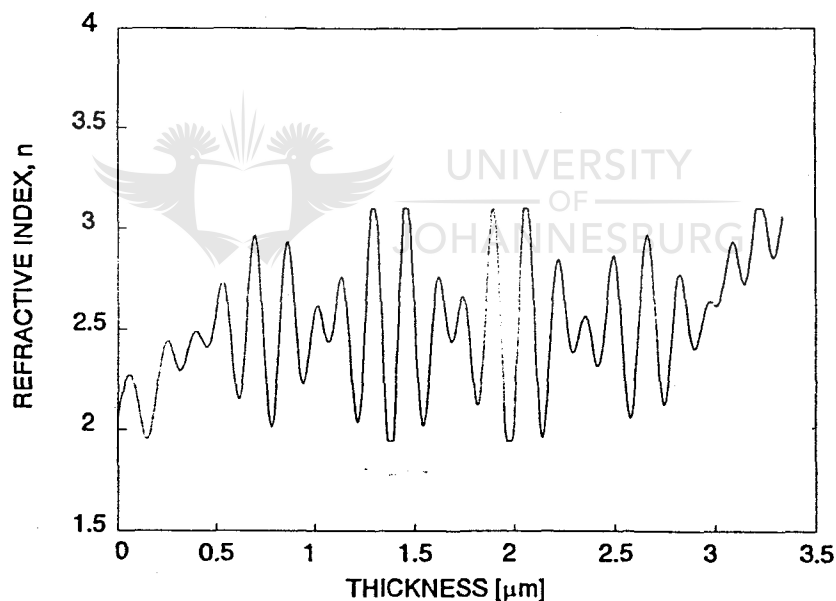


Figure 5.4: Refractive index profile (at wavelength 1000 nm) of a double-band SiN_x rugate filter on silicon.

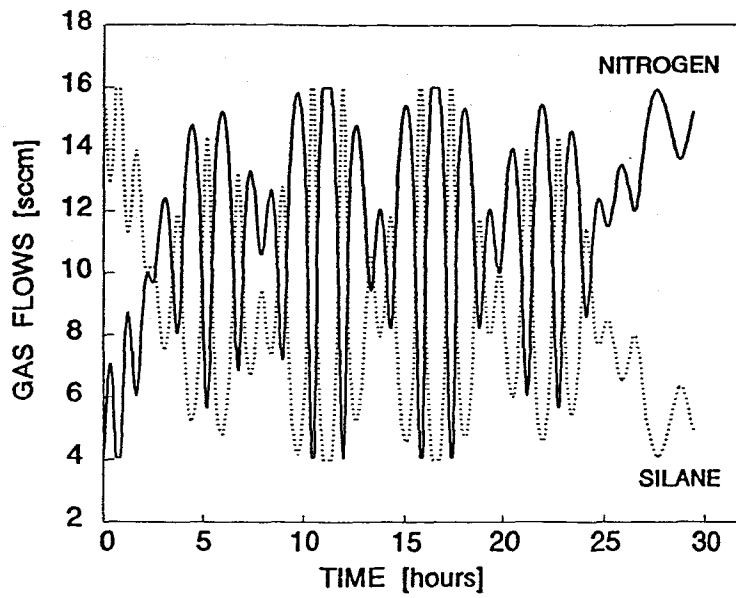


Figure 5.5: Required gas flows for the deposition of a double-band SiN_x rugate filter.

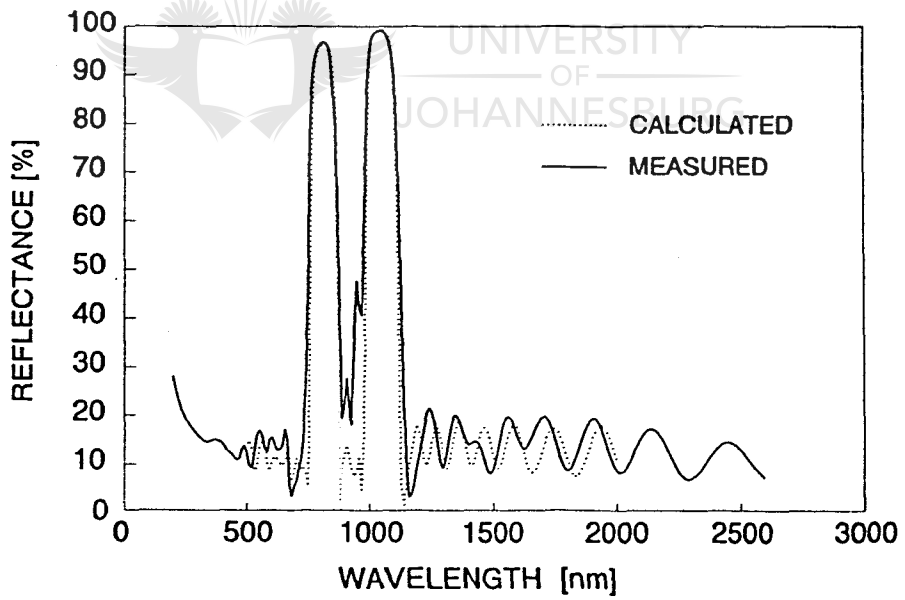


Figure 5.6: Reflectance spectra of a double-band SiN_x rugate filter on silicon.

Figure 5.6 shows the reflectance spectrum corrected for the aluminium reference mirror, of an as-grown double-band rugate filter. The corresponding simulated spectrum is shown by a dashed line in the above-mentioned figure. The maxima of the reflectance bands of the grown filter are not exactly at the designed values. The centre of the main band of the double band rugate filter is positioned at 1035 nm instead of at 1000 nm. The ratio 1.3:1 between positions of the main and second bands, however, has been preserved. The results are within 3.5 per cent of the design values. The discrepancy between the designed and actual spectra is attributed mainly to fluctuations in self-bias of the substrate, which was not under closed-loop control.

The experimental values for FWHM are approximately 15 per cent larger than expected. The upper band of the double-band filter has a bandwidth of 150 nm at 1035 nm (design value: 135 nm), whereas the FWHM bandwidth at 800 nm is 120 nm, compared to the expected value of 105 nm. We ascribe these increases to the slight undershoot of the mass-flow controller for silane, as was explained already in paragraph 5.3.1.

5.3.3 Single-band SiO_xN_y rugate filter on glass

Filters based on the Si-Si₃N₄ system have reflectance in the transparent region of not less than 15%. SiO_xN_y , on the other hand, could have a refractive index as low as that of SiO₂, yielding a much larger range of refractive indices and a reduced reflection of 5

to 8 per cent outside the stopband. Simultaneously, lower refractive index will allow for the more effective matching of the rugate filter with the substrate and incident medium (air).

Figure 5.7 presents three-dimensional graphs of n and k as functions of depth and wavelength of a rugate optical filter. This single-band rugate filter was designed for maximum reflectance at a wavelength of 680 nm. For a total layer thickness of 2.11 μm , the theoretical reflectance in the band was 97.6 per cent. The refractive index profile comprised a Kaiser window for the entire length of the coating, which was superimposed on a rugated quintic transitional matching layer from air to filter and from filter to substrate. The average refractive index in the filter proper was chosen to be 2.0, and the maximum peak-to-valley excursion of the refractive index equalled 1.0, while the adjustable parameter of the Kaiser window was set at $\theta_k = 4.25$.



This SiO_xN_y rugate structure was grown on Corning 7059 glass substrates. Temporal changes of the gas flows needed during the growth of the filter described above are shown in Figure 5.8. Figure 5.9 shows the reflectance spectrum of an as-grown single-band filter with correction for the reference aluminium mirror. The corresponding simulated spectrum is shown by a dashed line. The maximum in the reflectance band of the grown filter occurs at 700 nm and its height almost equals the design value. Shift of the central wavelength is approximately 3 per cent from the designed value of 680 nm. This discrepancy is also attributed to fluctuations in the self-bias of the substrate.

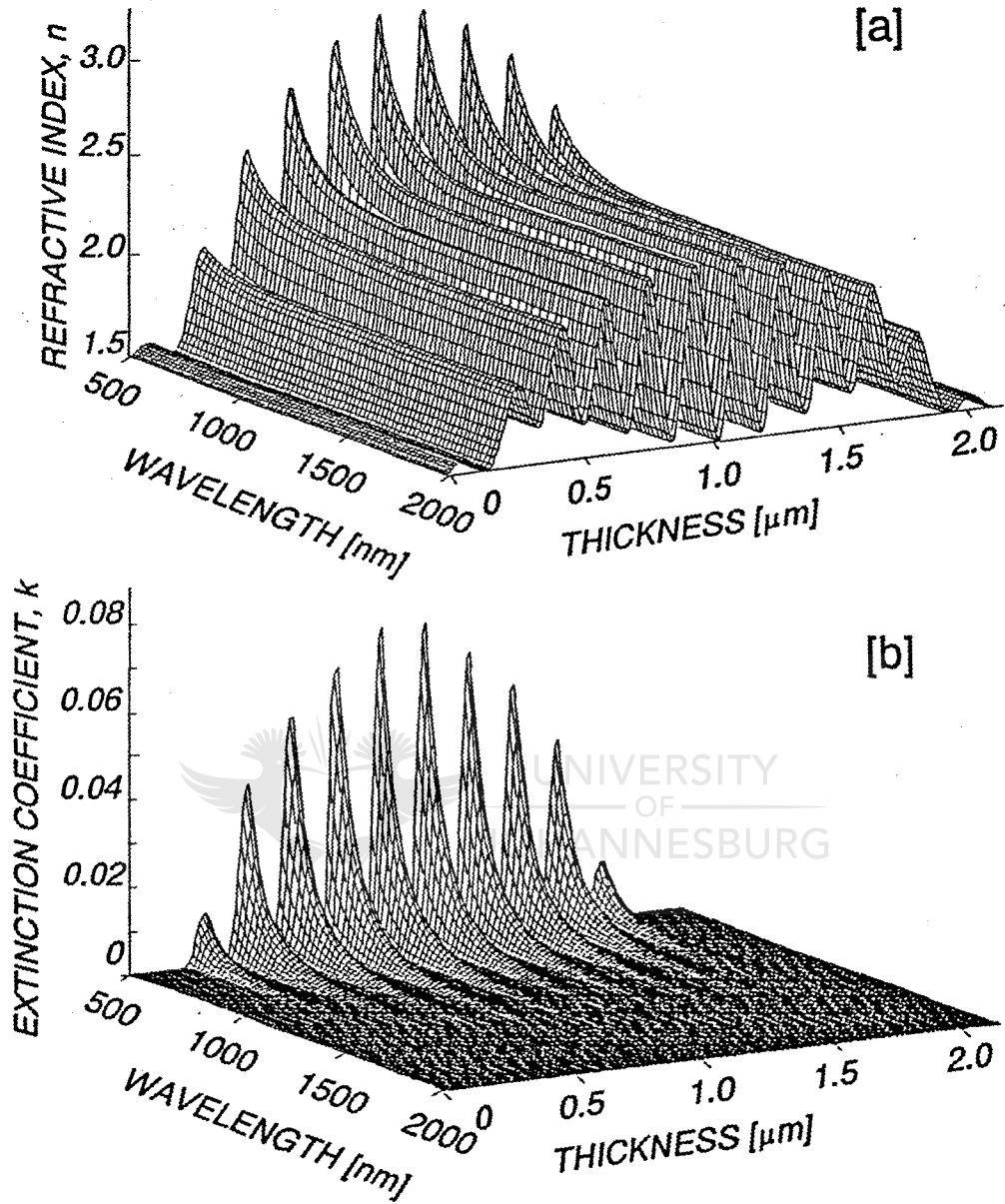


Figure 5.7: 3-dimensional representation of the refractive index (a), and extinction coefficient (b) of rugate filter on glass.

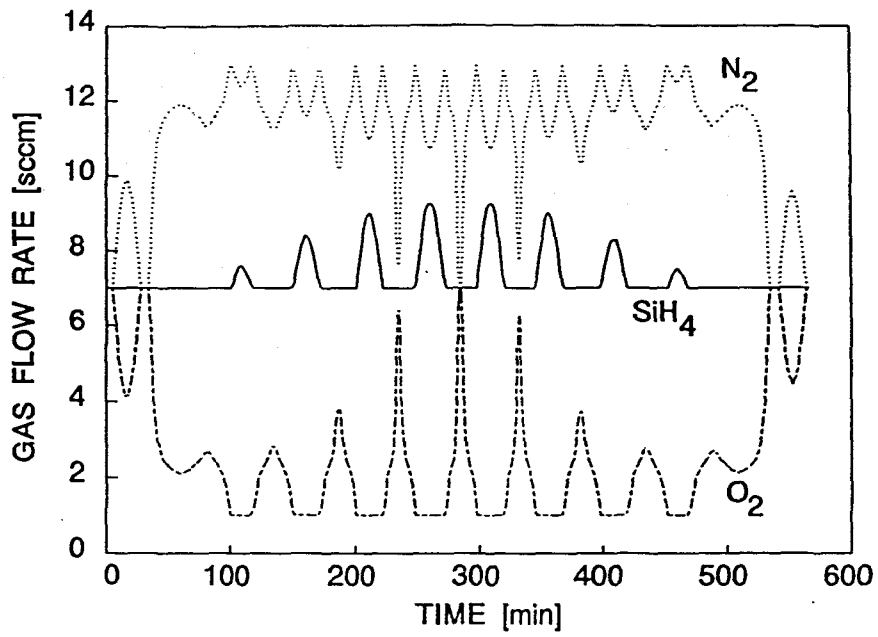


Figure 5.8: Temporal gas flows maintained during deposition of rugate filter on glass

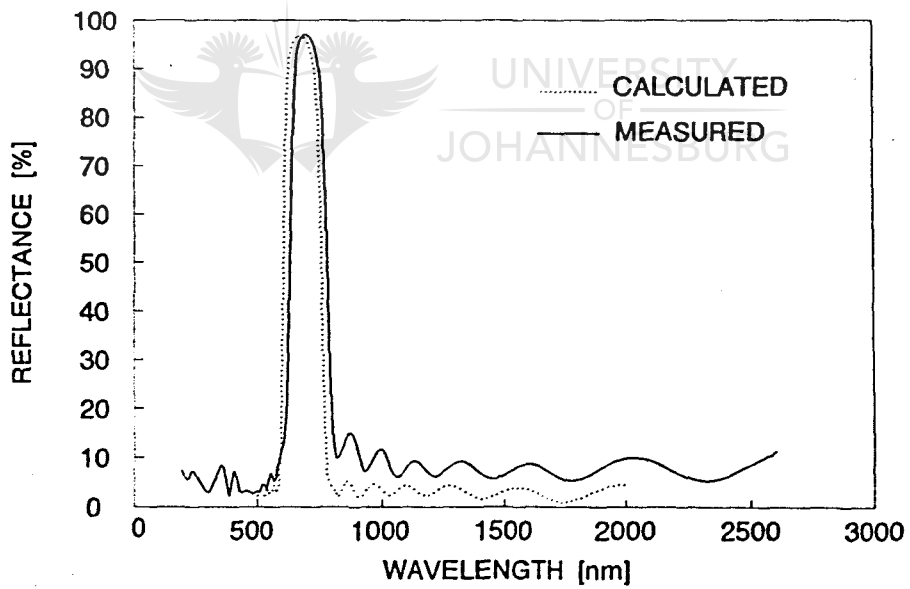


Figure 5.9: Simulated and measured reflectance of rugate filter

Owing to the fact that the Tylan 2600 MFC employed for control of oxygen flow did not exhibit undershoot, the experimental value obtained for bandwidth (FWHM) agrees with the expected value of 150 nm. Sidelobes outside the stopband are 5-8 per cent peak-to-peak. There is also a constant offset of approximately 4 per cent in the level of sidelobes as a result of incoherent reflections from the back surface of the glass substrate. These reflections were not accounted for in the simulations.

5.3.4 Gaussian antireflection coating on silicon

Mono-, polycrystalline and amorphous silicon solar cells together constitute a major source of alternative energy these days. It is known that there are two optimum energy band gaps for photovoltaic conversion³⁴. One is 1.15 eV (1.08 μm), which allows the use of all sunlight above the energy of strong atmospheric absorption (approximately 1.1 eV). The second optimum lies at 1.36 eV (0.911 μm). The silicon band gap equals 1.12 eV, therefore it lies just below the first optimum. However, all types of silicon are high-refractive index materials and reflectance of its bare surface is more than 30%. In order to make the most of the radiation of the sun an antireflection coating is required. We present here two types of antireflection coatings on silicon for application in photovoltaics, one inhomogeneous and the other a three-layer coating. The reference wavelength was chosen to be 800 nm, where the refractive index of monocrystalline silicon is 3.69³⁵.

The first coating is a Gaussian coating, with a refractive index profile shown in Figure 5.10. The profile is described by the formula

$$n(x) = n_{\min} + (n_{\max} - n_{\min}) \exp\left(-\frac{(x-4\sigma)^2}{2\sigma^2}\right) \quad (5.1)$$

where $\sigma = 0.048$ (one quarter of the total thickness of the coating). The total thickness of the coating is $0.19 \mu\text{m}$ and the refractive index gradually changes from $n_{\min} = 1.5$ to $n_{\max} = 2.9$ (at wavelength 800 nm). It would be better to have n_{\max} a closer match to the refractive index of the substrate. However, in the SiO_xN_y -system the maximum refractive index is limited by the chosen process trajectory (see chapter 2 and 3).

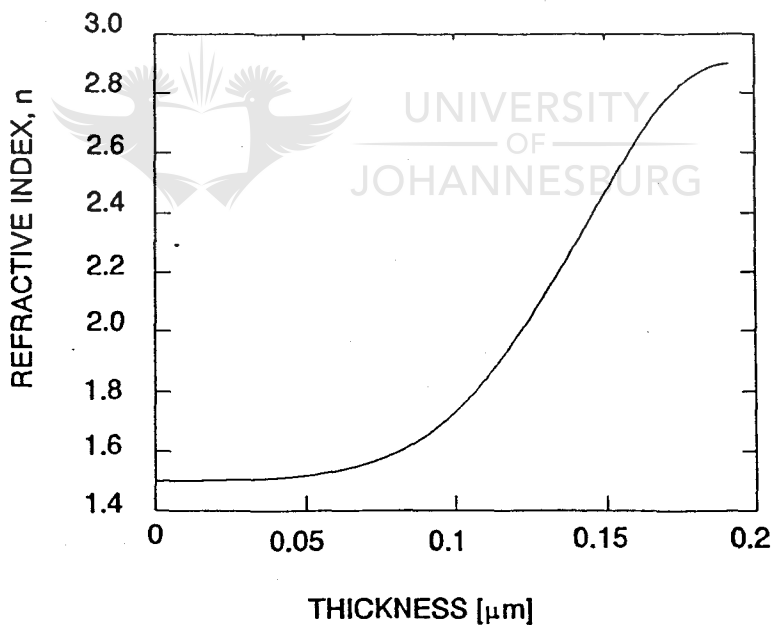


Figure 5.10: A refractive index profile of a $0.19 \mu\text{m}$ thick Gaussian antireflection coating

The required gas flows for fabrication of this coating are illustrated in Figure 5.11. Figure 5.12 illustrates the reflectance of an uncoated silicon wafer (1), in comparison with the design (2) and the actual performance (3) of the inhomogeneous refractive index coating. One can see that the reflectance was reduced drastically, from approximately 30% in the spectral range of interest to less than 5%. The actual performance is following the design prediction fairly closely, except for wavelengths shorter than 600 nm.

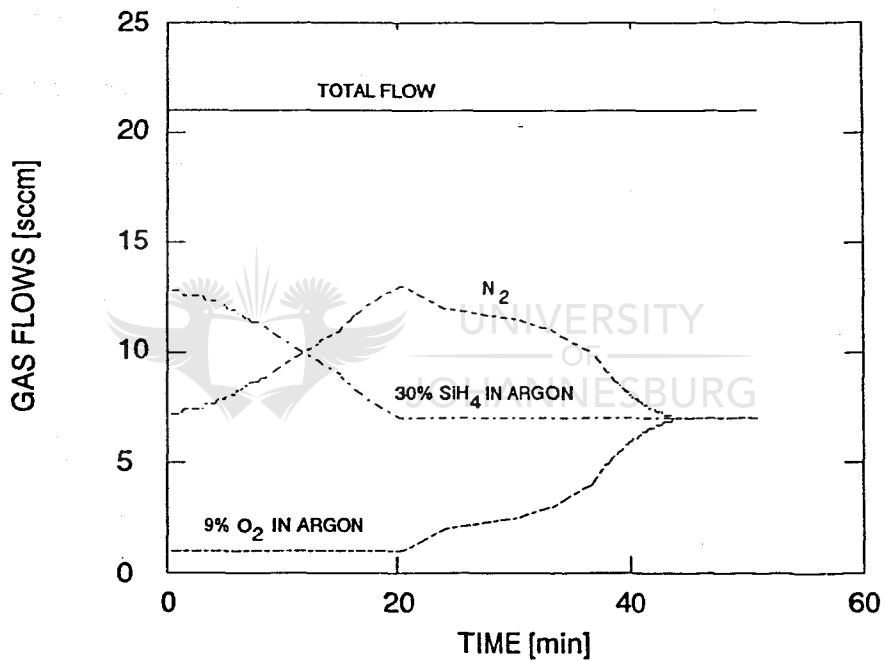


Figure 5.11: Temporal gas flows set during the growth of a Gaussian antireflection coating

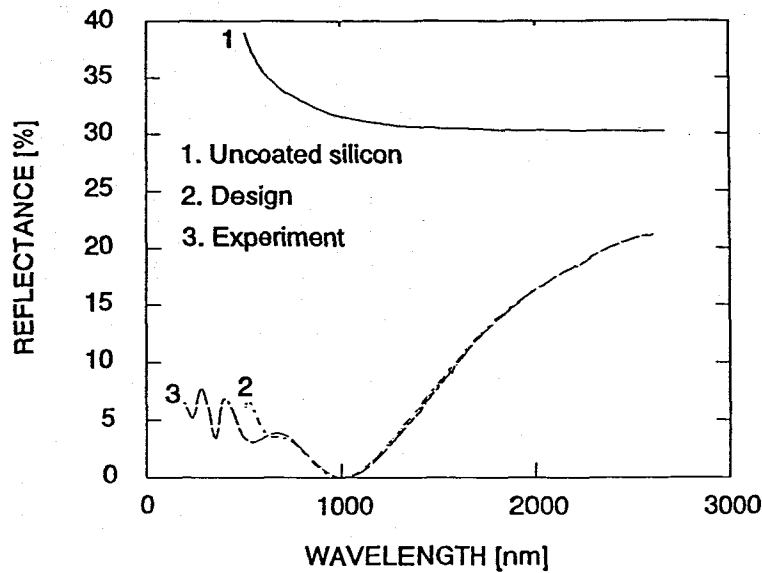


Figure 5.12: Reflectance spectra of a Gaussian antireflection coating on silicon

5.4 Multilayer filters

5.4.1 Three-layer antireflection coating on silicon

The 3-layer antireflection coating, with a total thickness of $0.23 \mu\text{m}$, consists of three homogeneous layers of materials with refractive indices and thicknesses chosen in such a way that they meet the requirements of matching neighbouring layers with constraint on the lowest refractive index possible³⁶, which is 1.5 for the SiO_xN_y system. Figure 5.13 illustrates the refractive index profile of the 3-layer antireflection coating. Figure 5.14 illustrates the reflectance of a bare silicon wafer (1) in comparison with the design (2) and the actual performance (3) of the three-layer antireflection coating. Again, the reflectance was reduced drastically, from approximately 30% in the spectral range

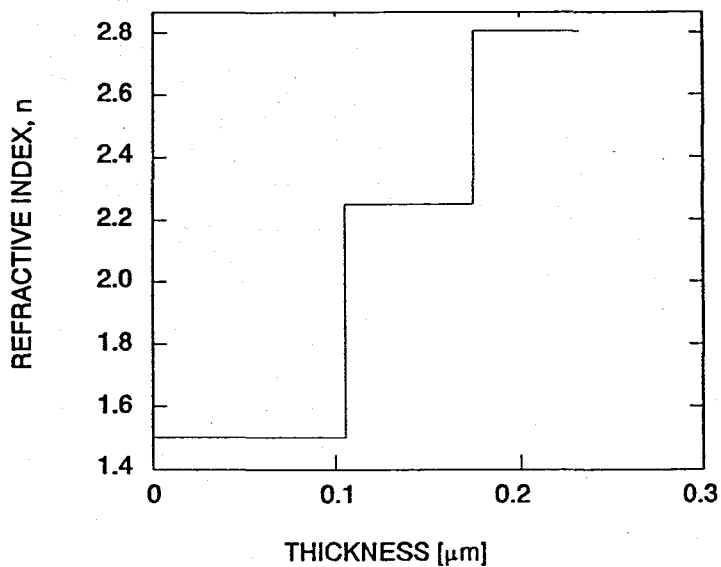


Figure 5.13: Refractive index profile of a 0.23 μm thick three-layer antireflection coating on silicon

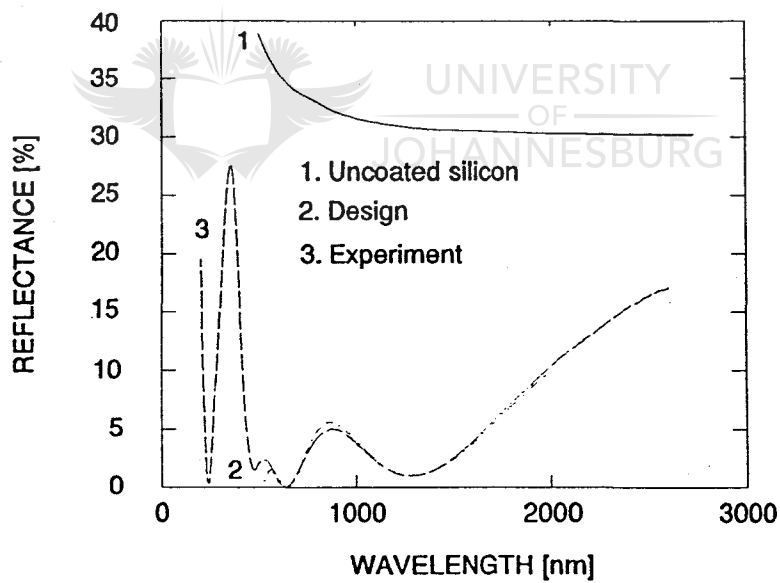


Figure 5.14: Reflectance of bare (1) and coated (3) silicon surface, (2) - design

of interest to no more than 5%. The actual performance is also following the design prediction sufficiently close, except for wavelengths shorter than 550 nm. However, in comparison with the inhomogeneous design, there are oscillations as high as 27 per cent in reflectance on the short wavelength side.

5.4.2 Beamsplitter on glass

Neutral beamsplitters have found many applications in modern optics, which requires the splitting or combining of light. A good example is a two-beam Michelson or Mach-Zehnder interferometer³⁷. It is possible to design an almost exactly 50/50 all-dielectric beamsplitter based on variations of high and low refractive index layers. We have adapted the design by HA Macleod³⁶, consisting of a combination LHLHLL (H=2.6, L=1.5) on glass for the 1300 to 1600 nm wavelength range. This range covers the wavelengths most frequently used in fibre-optic light sources, and such a beamsplitter can be incorporated into fibre-optic sensors based on interference effects.

The refractive index, and the design and performance of the beamsplitter are illustrated in Figures 5.15 and 5.16, respectively. Transmission (3) and reflection (2) curves, both are within 2 % of the required 50 % in the spectral range concerned. The splitter shows very good agreement with the design performance.

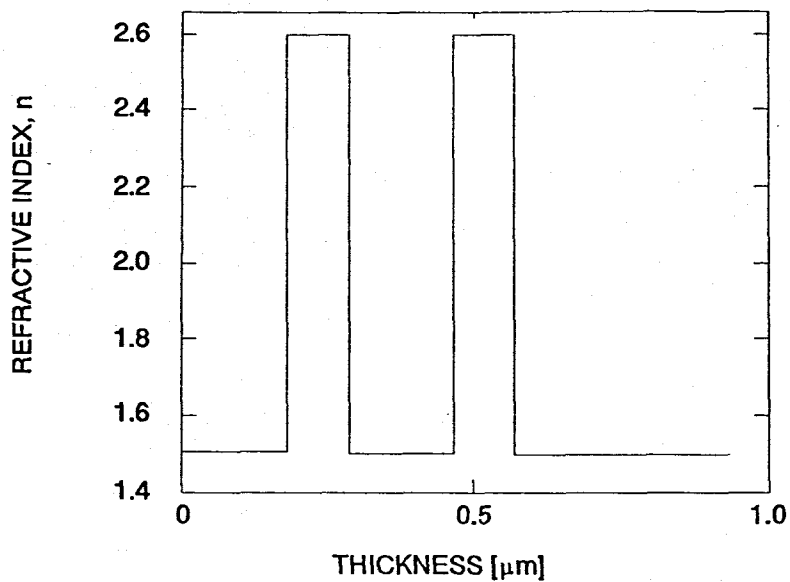


Figure 5.15: Refractive index profile of a 0.95 μm thick 50/50 beamsplitter

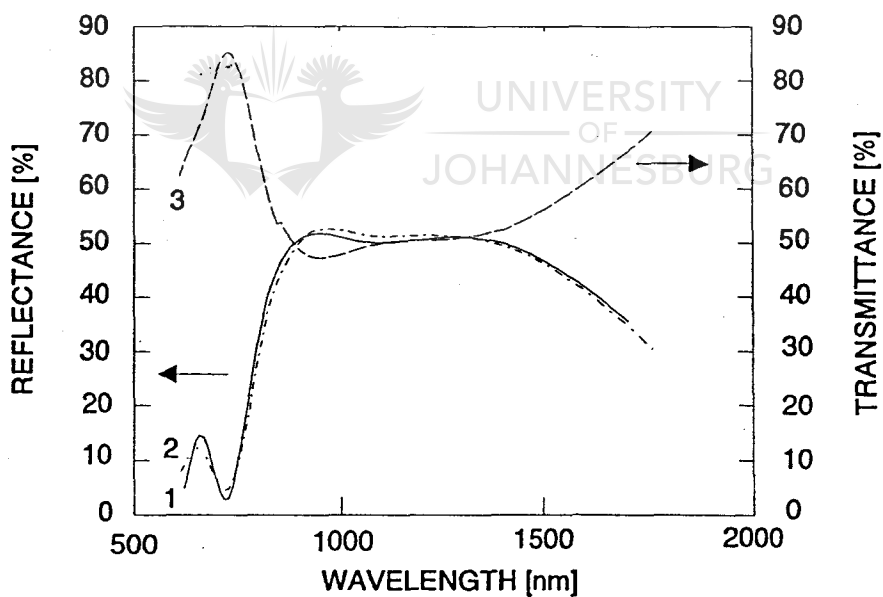


Figure 5.16: Design (1) and actual performance (2 and 3) of a LHLHLL beamsplitter

5.4.3 The multilayer high-reflection filter on glass

The fabrication of a multilayer high-reflection optical filter on a glass substrate was also undertaken. A SiO_xN_y Bragg reflector $[(\text{HL})^9]$ ($H=2.6$, $L=1.5$) was designed for the central wavelength of 1060 nm and grown on a Corning 7059 glass substrate. The refractive index profile of the filter is shown in Figure 5.17. Temporal changes of the gas flows needed during the growth of this filter are illustrated in Figure 5.18. The silane flow is denoted as 1, the nitrogen flow as 2 and the oxygen flow as 3, respectively.

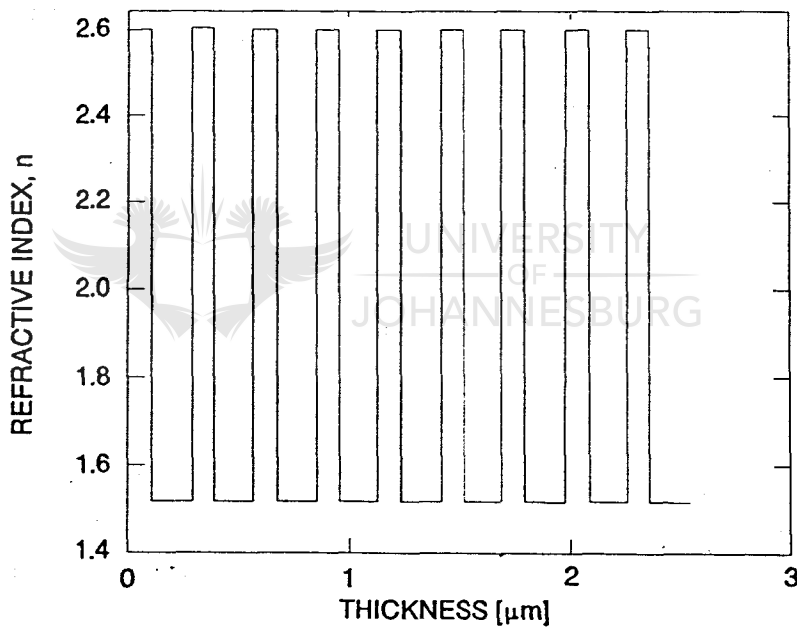


Figure 5.17: Refractive index profile of the high-reflection multilayer filter with structure air- $[(\text{HL})^9]$ -glass

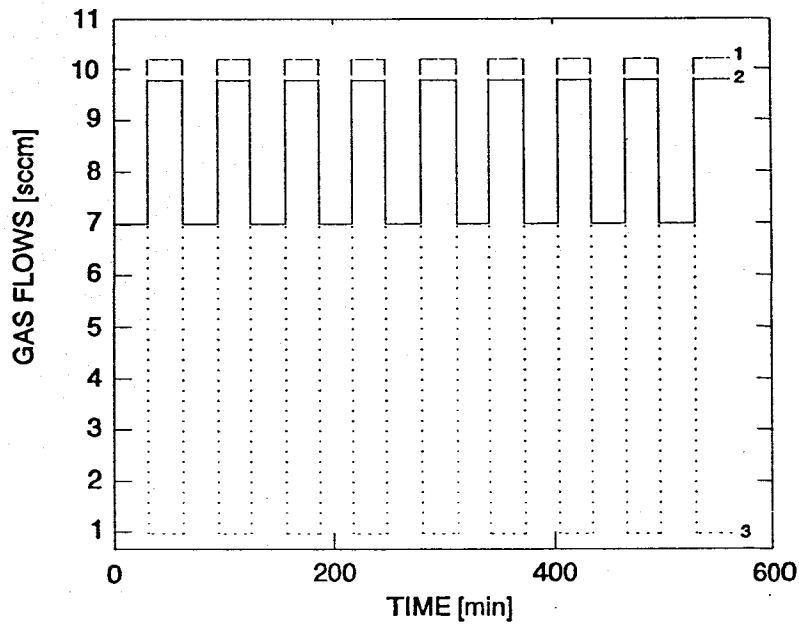


Figure 5.18: Temporal gas flows maintained during the deposition of the multilayer filter

Figure 5.19 shows the reflectance spectra of an as-grown filter corrected for the reference aluminium mirror. The maximum in the reflectance band of the grown filter occurs at 1050 nm and its height approximately equals the design value of slightly less than 100 per cent. The corresponding simulated spectrum is shown by a dashed line. The simulation was performed on the basis of the refractive index of the initial design by compressing its thickness by the value of corresponding to the shift of the centre wavelength. The shift of the central wavelength from the designed value of 1060 nm is approximately 1 per cent. Figure 5.20 shows the experimental reflectance and the transmittance spectra of this filter.

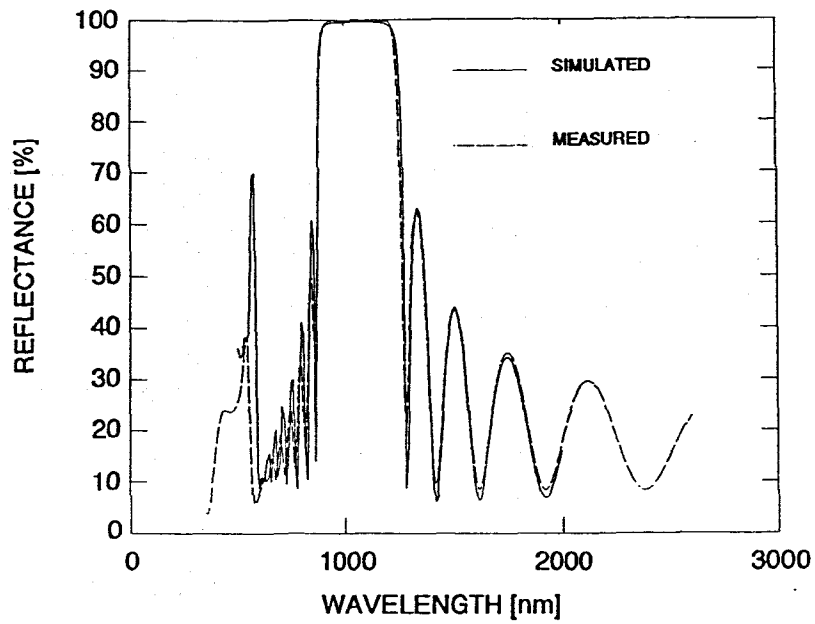


Figure 5.19: Simulated and measured reflectance of the multilayer filter

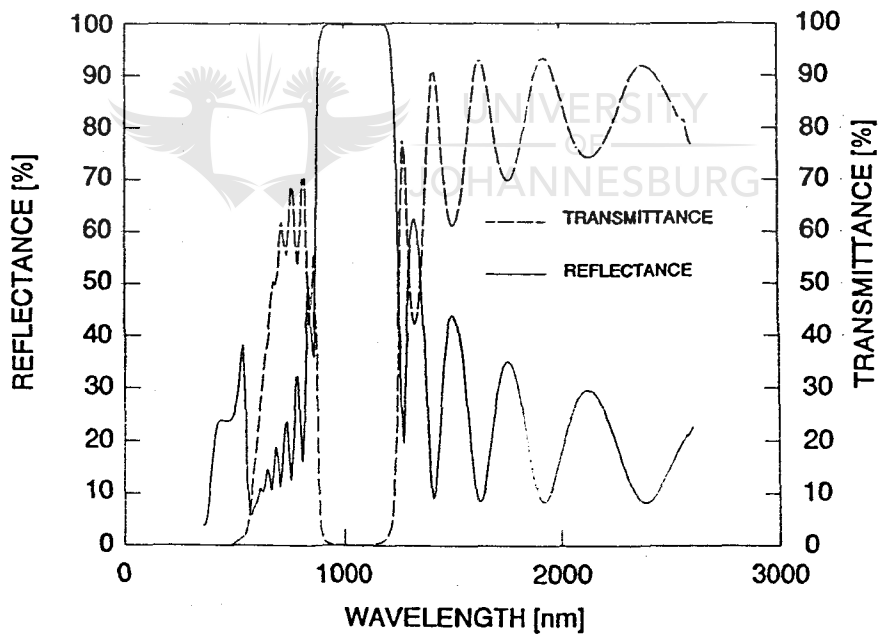


Figure 5.20: Measured reflectance and transmittance of the multilayer filter

5.5 Conclusions

As was shown, computer-controlled ECR plasma deposition is a convenient method of producing films with continuously varying refractive index. The advantages of easily achievable computerized mass-flow control and the strong dependence of refractive index on gas composition, together with the stable nature of ECR discharge at low pressures and the high quality of layers, could lead to the inclusion of ECR-PECVD in optical coatings technology.

The good agreement between the designs and the actual measured optical properties of the rugate structures confirms the attractiveness of ECR plasma deposition for the fabrication of layers with complicated refractive index profiles. Parameters of deposited filters made of SiN_x and SiO_xN_y agreed well with the designed values.

Single- and double-line rugate filters, an inhomogeneous antireflection coating, a three-layer antireflection coating, a beamsplitter and a multilayer high-reflection filter were grown by ECR-PECVD. Results show compatibility of ECR-PECVD with classical optical coatings design, while allowing the fabrication of very complex inhomogeneous structures.

The results made known here can be improved by incorporating new parameters, such as control of microwave power. Also, a divergent magnetic field ECR source is needed to increase the deposition rate and the deposition area. The introduction of these improvements will be the next step in our research.

REFERENCES FOR CHAPTER 5

1. R. Overend, D.R. Gibson, R. Marshall, and K. Lewis, "Rugate filter fabrication using neutral cluster beam deposition", *Vacuum*, Vol. 43, No. 1&2, 1992, pp. 51-54.
2. A.G. Greenham, B.A. Nichols, R.M. Wood, N. Nourshargh and K.L. Lewis, "Optical interference filters with continuous refractive index modulations by microwave plasma-assisted chemical vapour deposition", *Optical Engineering*, Vol. 32, No. 5, 1993, pp. 1018-1023.
3. E.P. Donovan, D. Van Vechten, A.D.F. Kahn, C.A. Carosella and G.K. Hubler, "Near infrared rugate filter fabrication by ion beam assisted deposition of $\text{Si}_{(1-x)}\text{N}_x$ films", *Applied Optics*, Vol. 28, No. 14, 1989, pp. 2940-2944.
4. H. Sankur, W. Southwell, R. Hall and W.J. Gunning, "Rugate filter deposition by the OMVPE technique", in Optical Interference Coatings Technical Digest, 1992 (Optical Society of America, Washington, D.C., 1992), Vol. 15, pp. 125-127.
5. K.L. Lewis, I.T. Muirhead, A.M. Pitt, A.G. Cullis, N.G. Chew, A. Miller, and T.J. Wyatt-Davies, "Molecular beam deposition of optical coatings and their characterization", *Applied Optics*, Vol. 28, No. 14, 1989, pp. 2785-2791.
6. W.J. Gunning, R.L. Hall, F.J. Woodberry, W.H. Southwell, and N.S. Gluck, "Codeposition of continuous composition rugate filters", *Applied Optics*, Vol. 28, No. 14, 1989, pp. 2945-2948.
7. C.S. Bartholomew, H.T. Betz, J.L. Grieser, R.A. Spence, and N.R. Murarka, "Rugate filters by laser flash evaporation of Si_xN_y on room temperature polycarbonate", *Proceedings of SPIE*, Vol. 821, Modelling of Optical Thin Films, 1987, pp. 198-204.

8. K. Sheach, and R. Heinecke, "Pulsed plasma deposition of optical filter structures", in Optical Interference Coatings Technical Digest, 1992 (Optical Society of America, Washington, D.C., 1992), Vol. 15, pp. 128-130.
9. S. Lim, J.H. Ryu, J.F. Wager, and T.K. Plant, "Rugate filters grown by plasma-enhanced chemical vapor deposition", *Thin Solid Films*, Vol. 245, No. 1&2, 1994, pp. 141-145.
10. P.V. Bulkin, P.L. Swart and B.M. Lacquet, "Properties and applications of electron cyclotron plasma deposited SiO_xN_y films with graded refractive index profiles", accepted for publication in "Journal of Non-Crystalline Solids".
11. P.V. Bulkin, P.L. Swart and B.M. Lacquet, "ECR plasma CVD for rugate filters manufacturing", *SPIE Proceedings*, Vol. 2253, Optical Interference Coatings, 1994, pp. 462-469.
12. W.H. Southwell and R.L. Hall, "Rugate filter sidelobe suppression using quintic and rugated quintic matching layers", *Applied Optics*, Vol. 28, No. 14, 1989, pp. 2949-2951.
13. W.H. Southwell, "Using apodization functions to reduce sidelobes in rugate filters", *Applied Optics*, Vol. 28, No. 23, 1989, pp. 5091-5094.
14. P.G. Verly, J.A. Dobrowolski, W.J. Wild, and R.L. Burton, "Synthesis of high rejection filters with the Fourier transform method", *Applied Optics*, Vol. 28, No. 14, 1989, pp. 2864-2875.
15. H. Fabricius, "Gradient-index filters: designing filters with steep skirts, high reflection, and quintic matching layers", *Applied Optics*, Vol. 31, No. 25, 1992, pp. 5191-5196.

16. B.G. Bovard, "Rugate filter design: the modified Fourier transform technique", *Applied Optics*, Vol. 29, No. 1, 1990, pp. 24-30.
17. B.G. Bovard, "Rugate filter theory: an overview", *Applied Optics*, Vol. 32, No. 28, 1993, pp. 5427 - 5442.
18. B.G. Bovard, "Ion-assisted processing of optical coatings", *Thin Solid Films*, Vol. 206, No. , 1991, pp. 224-229.
19. S.P. Fisher, J.F. Leonard, I.T. Muirhead, G. Buller and P. Meredith, "The fabrication of optical devices by molecular beam deposition technology", in Optical Interference Coatings Technical Digest, 1992 (Optical Society of America, Washington, D.C., 1992), Vol. 15, pp. 131-133.
20. J. Allen, B.D. Herrington, S. Jansen and J.C. Blomfield, "Graded rugate filters for head up displays", in Optical Interference Coatings Technical Digest, 1992 (Optical Society of America, Washington, D.C., 1992), Vol. 15, pp. 134-136.
21. J. Allen, P.G. Girow, B. Herrington, P. Gee, "Rugate filters for image projection in head-mounted displays", *SPIE Proceedings*, Vol. 2253, *Optical Interference Coatings*, 1994, pp. 470-475.
22. M. Heming, J. Hochauss, J. Otto and J. Segner, "Plasma impulse chemical vapour deposition - a novel technique for optical coatings", in Optical Interference Coatings Technical Digest, 1992 (Optical Society of America, Washington, D.C., 1992), Vol. 15, pp.296-298.
23. M.L. Elder, K.S. Jancaitis, D. Milam, and J. H. Campbell, "Optical Characterization of damage resistant "kilolayer" rugate filters", in Laser Induced Damage in Optical Materials: 1989, Lawrence Livermore National Laboratory report UCRL-JC-105036.

24. S. Lim, J.H. Ryu, and J.F. Wager, "Inhomogeneous dielectrics grown by plasma-enhanced chemical vapor deposition", *Thin Solid Films*, Vol. 236, No. 1&2, 1993, pp. 64 - 66.
25. D.J. Stephens, S.S. He, G. Lucovsky, H. Mikkelsen, K. Leo, and H. Kurz, "Effects of thin film deposition rates, and process-induced interfacial layers on the optical properties of plasma-deposited $\text{SiO}_2/\text{Si}_3\text{N}_4$ Bragg reflectors", *Journal of Vacuum Science and Technology A*, Vol. 11, No. 4, 1993, pp. 893 - 899.
26. J. Ahn and K. Suzuki, "Stress-controlled silicon nitride film with high optical transmittance prepared by an ultrahigh-vacuum electron cyclotron resonance plasma chemical-vapor deposition system", *Applied Physics Letters*, Vol. 64, No. 24, 1994, pp. 3249-3251.
27. Y. Manabe and T. Mitsuyu, "Silicon nitride thin films prepared by the electron cyclotron resonance plasma chemical vapor deposition", *Journal of Applied Physics*, Vol. 66, No.6, 1989, pp. 2475-2480.
28. S.V. Nguyen and K. Albaugh, "The characterization of electron cyclotron resonance plasma deposited silicon nitride and silicon oxide films", *Journal of Electrochemical Society*, Vol. 136, No. 10, 1989, pp. 2835-2840.
29. S. Dzioba, "ECR plasma deposition of dielectrics for optoelectronic applications", Research report, Bell-Northern Research Ltd., Ottawa, 1989.
30. S. Dzioba and R. Rousina, "Dielectric thin film deposition by electron cyclotron resonance plasma chemical vapor deposition for optoelectronics", *Journal of Vacuum Science and Technology B*, Vol. 12, No. 1, 1994, pp. 433-440.

31. P.V. Bulkin, P.L. Swart and B.M. Lacquet, "Electron cyclotron resonance plasma deposition of SiN_x for optical applications", Symposium C, E-MRS Spring Meeting, Strasbourg, France, 4-7 May 1993. (published in Thin Solid Films, Vol. 241, No. 1&2, 1994, pp. 247-250).
32. J. Asmussen, "Electron cyclotron resonance plasma microwave discharges for etching and thin-film deposition", Journal of Vacuum Science and Technology A, Vol. 7, No. 3, 1989, pp. 883-893.
33. P.V. Bulkin, P.L. Swart, B.M. Lacquet and F.J. Burger, "Electron cyclotron resonance plasma deposition for multilayer structures of silicon nitride on silicon", South African Journal of Physics, Vol. 16, No. 1&2, 1993, pp. 33-36.
34. M.A. Green, "Single-crystal silicon: photovoltaic applications", MRS Bulletin, Vol. 18, No. 10, pp. 26-28.
35. E.D. Palik (Editor), Handbook of Optical Constants of Solids, Academic Press, Orlando, Florida, 1985.
36. H.A. Macleod, Thin Film Optical Filters, 2nd ed., Adam Higler Ltd., Bristol, 1986.
37. O.S. Heavens and R.W. Ditchburn, Insight into optics, John Wiley & Sons, Inc., Chichester, 1991.

CHAPTER 6

CONCLUSIONS

6.1 Discussion

New deposition technologies are emerging with three major objectives, namely increased deposition rate, improved uniformity and improved level of control¹. As coating designs become thicker freedom from the current limitations on source capacity is required. Work towards the achievement of these objectives places ever-greater emphasis on the use of gas sources for which, in principle, the processing time is only limited by factors such as deposition rate and control reliability. Many of the precursors used in chemical vapour deposition (CVD) are based on corrosive, pyrophoric and poisonous substances (e.g. silane, metalorganics, etc.), which in themselves create additional needs for system integrity and safety¹.

Another important issue to be addressed by any development of a new deposition technique is that of a low substrate temperature operation which would allow the fabrication of advanced-type coatings on temperature-sensitive $A^{III}B^V$ and $A^{II}B^{VI}$, as well

as on organic materials. Direct chemical reaction, however, is not successful at low temperatures, and some form of plasma or ion assistance is required. Recent developments in plasma sources based on ECR technology have particular relevance here²⁻⁶. The exceptional stability of the ECR discharge and the proven controllability of the chemical vapour deposition technology ensure that coating performance can be guaranteed by feed-forward control alone, even in the most complex inhomogeneous designs, thus eliminating costly real-time broad-band optical monitoring. In addition, a choice of ECR-PECVD process can help coating manufacturers overcome two more problems, namely difficulties to perform the final stages of substrate preparation and the multiple deposition processes within a single vacuum system.

The work presented here applies ECR-PECVD for the first time to the fabrication of inhomogeneous optical interference coatings⁷⁻⁹. Electron cyclotron resonance plasma enhanced chemical vapour deposition was used for the deposition of amorphous SiO_x , SiN_x and SiO_xN_y films from O_2/Ar , N_2 and SiH_4/Ar mixtures. The properties of these thin films were determined by optical transmission spectroscopy and Fourier transform infrared spectroscopy (FTIR).

A comparison of the deposition of Si-SiO_2 and $\text{Si-Si}_3\text{N}_4$ alloys revealed marked differences in the growth rate behaviour and common trends in refractive index changes. For SiN_x deposition the growth rate decreased monotonically with an increase in the nitrogen flow (at constant total flow) from 43 to 17 Å/min, whereas the SiO_x growth rate

dependence has a maximum of around 75 Å/min at a gas flow ratio $\text{SiH}_4/(\text{SiH}_4+\text{O}_2)$ of approximately 0.7. Refractive indices for both processes decreased strongly with a decrease in the silane content of the gas phase: from amorphous silicon's 3.8 measured at 632.8 nm to 1.48 and 1.98 for silicon dioxide and silicon nitride, respectively.

ECR-PECVD of silicon oxynitride layers was also investigated for different gas flow ratios and substrate bias. The growth rate was in the 20 to 100 Å/min range, whereas the refractive index changed from 2.60 to 1.48, with a corresponding change in the $\text{O}_2/(\text{N}_2+\text{O}_2)$ ratio from 0.01 to 0.32 at constant total flow and constant silane flow. It was also found that increased self-bias resulted in a substantial increase in the growth rate, whereas the refractive index shared a marginal change only. Working pressure and magnetic field exerted a slight influence on the refractive index of a material, but had a marked effect on the growth rate. The gas flow ratio determined the refractive index over a wide range as a result of changes in the chemical composition. FTIR measurements showed a smooth transition between silicon dioxide and silicon nitride. Raman spectroscopy showed that the films deposited from silane diluted with argon, possess amorphous structure.

The investigation produced new information on the optical properties of SiO_x , SiN_x and SiO_xN_y thin films deposited by ECR-PECVD from mixture of silane, oxygen, nitrogen and argon. The results show a strong dependence of n , k and α on the composition of the gas mixture during deposition. The curves of refractive indices for SiO_x and SiN_x

materials grown at a gas composition with the lowest silane content are almost identical to those for stoichiometric SiO_2 and Si_3N_4 films. These values are close to the corresponding values for films grown by thermal oxidation, high-temperature CVD and reactive ion plating, suggesting a small amount of hydrogen in the compounds. With decreasing silicon content in the films, k , α and E_g exhibit a strong blue shift. The explanation for this fact can be found in the two models currently being used to describe the bonding structure of non-stoichiometric SiN_x and SiO_x . This blue shift can be linked to the substitution of Si-Si bonds with Si-O and Si-N bonds (in the case of the random network bond model) or to the decrease of the α -Si-phase in comparison with the SiO_2 and Si_3N_4 phases (in the case of the two separate phases model). The estimated values of the optical band gap lie between 1.7 and 4.2 eV for SiN_x and between 1.7 and more than 6 eV for SiO_x . The transmission curves calculated, using the measured optical constants, show a great measure of agreement with the experimental spectra.



The data on the properties of ECR-PECVD-deposited thin film is in good agreement with that reported for high-quality, low-absorption SiO_x , SiN_x and SiO_xN_y layers. The results demonstrate that ECR-PECVD can be used successfully for the manufacturing of optical filters with pre-programmed graded refractive index profiles by controlling the gas flows of silane, nitrogen and oxygen, respectively. Computer-controlled microwave ECR plasma enhanced chemical vapour deposition was shown to be a convenient method of producing films with constant or continuously varying refractive indices. The advantages of easily implemented computerized mass-flow control and the strong

dependence of the refractive index on gas composition, together with the stable nature of ECR discharge at low pressures and the high quality of layers, could lead to the inclusion of ECR-PECVD in optical coatings technology. The results obtained, however, not only can be used for optical applications, but contained general valuable information regarding structure and properties of materials available in the SiO_xN_y system.

Computer software was developed for the extraction of important optical parameters of thin films, namely complex refractive index, absorption coefficient and band gap from the transmission spectra. We also implemented software for the Fourier transform synthesis technique, and applied it in the design of a broad-band beamsplitter. In addition, detailed information gained on the optical properties of SiO_xN_y was incorporated into design software for single- and dual-band rugate optical filters. The program suite includes a choice of average value and excursion of refractive index, types of matching layers and apodization functions. Filter reflectance response curves are computed taking into account dispersion of complex refractive index and absorption in the film.

The agreement between designs and actually measured optical properties of the rugate structures confirms the attractiveness of ECR plasma deposition for the fabrication of layers with complicated refractive index profiles. Parameters of deposited filters made of SiN_x and SiO_xN_y agreed well with designed values. Overall errors in the positions of the peaks and peak reflectance did not exceed 4 per cent. Truly inhomogeneous rugate filters, a Gaussian antireflection coating, a three-layer antireflection coating, a

beamsplitter and a multilayer Bragg reflector were grown by this technique. Results show compatibility of ECR-PECVD with classical optical coatings design and fabrication, while allowing the fabrication of even the most complex inhomogeneous structures.

6.2 Recommendation for further research

The deposition technique for optical interference coatings fabrication developed in the work has proven very promising and has enabled us to realise any custom-designed refractive index profile. However, in order fully to evaluate the advantages and disadvantages of this technique, further development seems necessary.

It is necessary, for instance, to extend the wavelength range over which materials are characterized, which was in this work limited to the 200 to 2600 nm working range of the Hitachi U-3400 spectrophotometer. Such extension will allow the design and simulation of optical coatings to be carried out for short wavelength ultraviolet, as well as for the mid- and far-infrared ranges. Also, only optical characterization is not sufficient for adequate analysis of optical thin films. Direct investigation of the chemical composition of SiO_x , SiN_x and SiO_xN_y by X-ray photoelectron spectroscopy (XPS) or quantitative Auger electron spectroscopy (AES) should be accomplished, as well as a study of the physical properties, such as packing density and stress in the films. An evaluation of environmental stability will also be useful.

The results made known in this research project can be improved by incorporating new parameters, such as closed-loop control of the microwave generator. No expensive hardware alterations are needed and it should be performed in the near future. However, the main obstacles in the current realization of ECR-PECVD are the low growth rate and the lack of uniformity, both of which can be traced to the utilization of a compact ECR source, initially developed for molecular beam epitaxy, chemical beam epitaxy and surface analysis applications. The low growth rate is due to the fact that microwave power of only up to 100 W can safely be allowed in order to preserve vacuum integrity of the compact ECR source. Reasonable uniformity can only be obtained over an area of approximately 20 mm by 20 mm, owing to the magnetic field distribution of the ring-shaped SmCo_5 magnets employed in the source. These problems can, however, be rectified by replacing the compact ECR source with a divergent magnetic field ECR source based on a cylindrical waveguide applicator which is reported to allow uniform deposition on an area of up to 500 mm in diameter⁴ and which is reported to increase the growth rate up to 3000 Å/min (for SiO_2 deposition)¹⁰. For this, alterations of the main vacuum chamber will be required, and considerable expenses will have to be incurred.

REFERENCES FOR CHAPTER 6

1. K.L. Lewis, "Crystal gazing - a look towards optical coatings in the future", in Optical Interference Coatings Technical Digest, 1992 (Optical Society of America, Washington, D.C., 1992), Vol. 15, pp. 401-403.
2. A. Ghanbari, M.S. Ameen, and R.S. Heinrich, "Characterization of a large volume electron cyclotron resonance plasma for etching and deposition of materials", *Journal of Vacuum Science and Technology A*, Vol. 10, No. 4, 1992, pp. 1276-1280.
3. J. Pelletier and T. Lagarde, "Chemical vapor deposition in high-density low-pressure plasmas: reactor scale-up and performance", *Thin Solid Films*, Vol. 241, No. 1&2, 1994, pp. 240-246.
4. L. Bourget, B. Lane and J. Ding, "Large area ECR processing", presented at the E-MRS Spring Meeting 1994, Symposium A "Amorphous insulating thin films II", paper A-VII-XII/P51, Strasbourg, May 24-27, 1994.
5. G.D. Alton and D.N. Smithe, "Design studies for an advanced ECR ion source", *Review of Scientific Instruments*, Vol. 65, No. 4, 1994, pp. 775-787.
6. W.D. Getty and J.B. Geddes, "Size-scalable, 2.45-GHz electron cyclotron resonance plasma source using permanent magnets and waveguide coupling", *Journal of Vacuum Science and Technology B*, Vol. 12, No. 1, 1994, pp. 408-415.
7. P.V. Bulkin, P.L. Swart and B.M. Lacquet, "Electron cyclotron resonance plasma deposition of SiN_x for optical applications", *Thin Solid Films*, Vol. 241 No. 1&2, 1994, pp. 247-250.

8. P.V. Bulkin, P.L. Swart and B.M. Lacquet, "ECR plasma CVD for rugate filters manufacturing", SPIE Proceedings, Vol. 2253, Optical Interference Coatings, 1994, pp. 462-469.
9. P.V. Bulkin, P.L. Swart and B.M. Lacquet, "Properties and applications of electron cyclotron plasma deposited SiO_xN_y films with graded refractive index profiles", accepted for publication in "Journal of Non-Crystalline Solids".
10. B. Gorowitz, R.H. Wilson and T.B. Gorczyca, "Recent trends in LPCVD and PECVD", Solid State Technology, No. 10, 1987, pp. 97-103.



UNIVERSITY
OF
JOHANNESBURG